

---

# $^1\text{H}$ MR Spectroscopy and Chemical Shift Imaging of the *In Vivo* Brain at 7 Tesla

DISSERTATION

zur Erlangung des Grades eines Doktors  
der Naturwissenschaften  
der Fakultät für Mathematik und Physik  
der Eberhard-Karls-Universität zu Tübingen

vorgelegt von

Christoph Juchem  
aus Koblenz

2006

---

Tag der mündlichen Prüfung: 22. November 2006

Dekan: Prof. Dr. N. Schopohl

1. Berichterstatter: Prof. Dr. Dr. F. Schick

2. Berichterstatter: Prof. Dr. K. Albert

# Abstract

Neurotransmitters and compounds of the brain's energy metabolism are directly linked to brain function. *In vivo* magnetic resonance (MR) spectroscopy is a useful method to quantify the neurochemical profiles of localized brain regions non-invasively and to provide valuable information for medical treatment or for the study of underlying mechanisms. The concentrations of substances in the brain detectable by MR, however, are at best in the range of millimols and the sensitivity of MR methods that are based on the Boltzmann spin polarization is inherently low. Most anatomical or functional structures in the brain of humans and monkeys are in the millimeter range or below. The spatial resolution that would be necessary to account for the small target dimensions could not be realized so far in humans and with current MR systems. Reasonable signal strength could only be achieved at the cost of limited spatial specificity.

The spectral quality of *in vivo* MR spectroscopy and the amount of information available from it strongly depend on the existence and strength of potential experimental artifacts like frequency drifts, localization errors or spectral contaminations. In addition, the homogeneity of the magnetic field within the sensitive probe volume is a critical issue.

The goal of the thesis was to establish different methods for MR spectroscopy and chemical shift imaging at maximum spatial specificity and spectral quality. The methods were to be adopted for investigations of the non-human primate visual cortex, an area of intense study of the brain's physiology and function.

To maximize the sensitivity and the quality of the MR spectra, a number of methods have been implemented and optimized. Artifact sources were analyzed and methodological corrections were proposed to overcome them. For instance, strong limitations of the MR scanner's built-in capacity to compensate actively for inhomogeneities of the magnetic field by electrical coils were overcome by newly designed

ferromagnetic permalloy assemblies. A combined modular passive (ferromagnetic) and active (electrical) shimming method was developed that provides very strong and highly accurate correction fields for the homogenization of magnetic field distributions in the *in vivo* brain with reasonably low experimental effort.

MR spectroscopy of the macaque primary visual cortex (V1) is challenging, because of its position adjacent to the skull bone and the cortical thickness of only 1.7–2.0 mm. A dedicated 7 Tesla high field MR setup, an anesthetized monkey preparation and optimized MR methods enabled single voxel MR spectroscopy from 40  $\mu\text{L}$  volumes of V1. Due to the varying magnetic susceptibility conditions around macaque V1 this region is prone for susceptibility induced field distortions. To achieve optimal field homogeneity, field distributions were analyzed, and an appropriate shimming strategy was developed. With the established methods the successful sampling from brain regions entirely confined within V1 gray matter is now possible.

Chemical shift imaging methods were implemented and optimized to permit high resolution spatial mapping of metabolite distributions from the macaque visual cortex. The feasibility of chemical shift imaging along planar slices through the brain with a spatial resolution of 1–2 mm has been shown using conventional phase encoding. In addition, Hamming acquisition weighting was provided to improve the reliability of the metabolic mapping based on its favorable imaging properties.

Applying the techniques developed in this thesis the achieved resolution limits for  $^1\text{H}$  MR spectroscopy and chemical shift imaging in monkeys were 2–3 orders of magnitude better compared to previous studies in humans. The spatial specificity now reaches the level of *cortical* dimensions which is the basis for the investigation of physiology and function in the primate visual system.

# Zusammenfassung

Neurotransmitter und Metabolite des zerebralen Energiestoffwechsels sind unmittelbar mit Hirnaktivität korreliert. *In vivo* Magnetresonanzspektroskopie ermöglicht eine direkte, nicht-invasive Messung einer Vielzahl dieser chemischen Komponenten von lokalisierten Bereichen des Gehirns. Die so erzielbaren Erkenntnisse sind von hohem Wert für die medizinische Diagnostik auf der einen Seite sowie für die Erforschung der zugrunde liegenden Mechanismen auf der anderen. Die Konzentrationen der auf diese Weise detektierbaren Substanzen im Gehirn sind jedoch sehr gering und bestenfalls im Bereich weniger Millimol. Zusätzlich ist die Sensitivität von Magnetresonanzenexperimenten an sich sehr begrenzt für Techniken, die auf der Boltzmann'schen Spinpolarisation beruhen. Die Dimensionen anatomischer und funktioneller Strukturen im Gehirn von Menschen und Affen liegen im Bereich von Millimetern oder darunter. Räumliche Auflösungen, die in der Lage wären solch kleine Meßobjekte zu erfassen sind bisher und mit heutigen MR Systemen am Menschen nicht realisierbar. Ausreichende Signalstärken konnten nur auf Kosten einer limitierten räumlichen Auflösung erreicht werden.

Die spektrale Qualität von *in vivo* MR Spektren und der daraus zu erzielende Informationsgehalt hängen maßgeblich von der Existenz und Größenordnung potentieller Meßartefakte wie Frequenzverschiebungen, Lokalisierungsfehlern und spektralen Verunreinigungen ab. Inhomogenitäten des Magnetfeldes innerhalb des betrachteten Raumbereiches stellen ein weiteres, grundlegendes Problem dar.

Das Ziel dieser Arbeit war die Etablierung von Methoden für MR Spektroskopie und spektroskopische Bildgebung mit maximaler räumlicher Spezifität und bestmöglicher spektraler Qualität. Diese waren so anzupassen, daß Untersuchungen der Sehrinde des nicht-menschlichen Primaten und die Erforschung von Hirnphysiologie und -funktion in diesem Bereich des Gehirns ermöglicht werden.

Im Rahmen dieser Arbeit wurden verschiedene MR spektroskopische Methoden implementiert und bzgl. der speziellen Erfordernisse optimiert. Artefaktquellen wurden analysiert und methodische Korrekturen wurden vorgeschlagen, diese zu minimieren oder zu beheben. So wurden etwa starke Limitierungen zur aktiven Homogenisierung von Magnetfeldverteilungen mittels elektrischer Spulen des MR Tomographen durch eine neue Entwicklung von modularen, ferromagnetischen  $\mu$ -Metall-Anordnungen gelöst. Durch die Kombination von Methoden zur (ferromagnetischen) passiven und (elektronischen) aktiven Magnetfeldmodulierung ist es nun möglich, mit vertretbarem Aufwand sehr starke und trotzdem sehr präzise Magnetfeldverteilungen zur Korrektur von Feldinhomogenitäten im *in vivo* Gehirn zu generieren.

MR Spektroskopie in der primären Sehrinde (V1) im Makaken ist eine besondere Herausforderung wegen der unmittelbaren Nähe von V1 zum Schädelknochen und weil die kortikale Dicke in diesem Bereich lediglich 1.7–2.0 mm beträgt. Die Verwendung eines spezialisierten 7 Tesla Hochfeld MR Tomographen, eine Anästhesiepräparation der Versuchstiere und optimierte MR Methoden waren nötig, um volumenselektive MR Spektroskopie aus 40  $\mu$ l kleinen Volumina von V1 zu ermöglichen. Aufgrund der Regionen unterschiedlicher magnetischer Suszeptibilitäten im Bereich von Kortex, Schädelknochen und der den Kopf umgebenden Luft werden insbesondere dort Feldverzerrungen beobachtet. Die auftretenden Magnetfeldinhomogenitäten im Bereich der primären Sehrinde wurden daher vermessen, analysiert und es konnte eine Strategie vorgeschlagen werden, diese effizient zu minimieren. Mit den hier etablierten Methoden sind nun MR spektroskopische Untersuchungen von kleinsten Volumina möglich, die sich komplett innerhalb der primären Sehrinde befinden.

Desweiteren wurden Methoden zur spektroskopischen Bildgebung implementiert und optimiert, um eine hochaufgelöste Kartierung der Metabolitenverteilung des visuellen Kortex zu ermöglichen. Mittels konventioneller Phasenkodierung wurde die Machbarkeit von spektroskopischen Karten der Sehrinde mit einer Ortsauflösung von 1–2 mm gezeigt. Zusätzlich wurden Methoden zur Hamming Akquisitionswichtung bereitgestellt, durch deren verbesserte Lokalisierungseigenschaften eine weitere Erhöhung der Verlässlichkeit erzielter metabolischer Karten zu erwarten ist.

Die vorgelegte Dissertation beschreibt die Verbesserung der räumlichen Auflösung von MR Spektroskopie und spektroskopischer Bildgebung im Primaten von 2–3 Größenordnungen verglichen mit ähnlichen Studien am Menschen. Die räumliche Spezifität hat somit ein *kortikales* Niveau erreicht, das die Grundlage darstellt für Studien von Physiologie und Funktion des visuellen Systems.

# Contents

<b>1</b>	<b>Physical Basics of Magnetic Resonance</b>	<b>12</b>
1.1	Spin Magnetization . . . . .	12
1.2	Bloch Equations and Relaxation . . . . .	14
1.3	Radio-Frequency Excitation . . . . .	16
1.4	Chemical Shift . . . . .	17
1.5	Dipolar Coupling . . . . .	18
1.6	J-Coupling . . . . .	19
1.7	Magnetic Field Gradients . . . . .	20
1.8	k-Space . . . . .	21
1.9	Chemical Shift Displacement . . . . .	22
1.10	Field Homogeneity . . . . .	23
<b>2</b>	<b>Techniques for <math>^1\text{H}</math> MR Spectroscopy</b>	<b>28</b>
2.1	Single Voxel Spectroscopy . . . . .	28
2.2	Conventional Chemical Shift Imaging . . . . .	30
2.3	Acquisition Weighted Chemical Shift Imaging . . . . .	31
2.4	Water Suppression . . . . .	31
2.5	Outer Volume Suppression . . . . .	32
2.6	Spectrum Quantification . . . . .	33
2.7	Field Homogenization . . . . .	35
<b>3</b>	<b>MR Spectroscopy of the Brain</b>	<b>37</b>
3.1	MR Spectroscopy in Neuroscience . . . . .	37
3.2	The Visual Cortex: Function and Significance . . . . .	38
3.3	Compounds in $^1\text{H}$ MR Spectroscopy of the Brain . . . . .	39
3.4	Spectral Separation of $^1\text{H}$ Brain Metabolites . . . . .	54
<b>4</b>	<b>Experimental Setup</b>	<b>58</b>
4.1	7 Tesla Magnet . . . . .	58
4.2	Magnetic Field Gradients . . . . .	59

4.3	Radio-Frequency System . . . . .	59
4.4	Anesthetized Monkey Setup . . . . .	60
<b>5</b>	<b>Implementation and Quality Management</b>	<b>62</b>
5.1	Implementation of MR Spectroscopy and CSI . . . . .	62
5.2	Performance and Quality Measures . . . . .	71
5.3	Frequency Lock Algorithm . . . . .	72
5.4	MR Frequency Stability . . . . .	73
5.5	First Order Localized Shim Algorithm . . . . .	76
5.6	Experiment Adjustment and Execution . . . . .	76
5.7	Simulation of $^1\text{H}$ MR Metabolite Spectra . . . . .	80
<b>6</b>	<b>Combined Passive and Active Shimming</b>	<b>82</b>
6.1	Theoretical Design and Optimization . . . . .	84
6.2	Experimental Validation . . . . .	93
6.3	Combined Shimming in the Monkey . . . . .	94
6.4	Significance and Discussion . . . . .	98
<b>7</b>	<b>Chemical Shift Imaging of the Visual Cortex</b>	<b>101</b>
7.1	High Resolution CSI of the Visual Cortex . . . . .	101
7.2	Significance and Discussion . . . . .	106
<b>8</b>	<b>Acquisition Weighted Chemical Shift Imaging</b>	<b>108</b>
8.1	Theoretical Comparison of Weighting Schemes . . . . .	108
8.2	Implementation of Hamming Weighted CSI . . . . .	112
8.3	Experimental Validation . . . . .	113
8.4	Significance and Discussion . . . . .	115
<b>9</b>	<b>MR Spectroscopy of V1</b>	<b>116</b>
9.1	<i>In vivo</i> MR Spectroscopy in V1 . . . . .	116
9.2	Shimming at the Brain Surface . . . . .	118
9.3	Localized $^1\text{H}$ MR Spectroscopy in Macaque V1 . . . . .	124
9.4	Significance and Discussion . . . . .	127
<b>10</b>	<b>Summary</b>	<b>129</b>
	<b>Bibliography</b>	<b>148</b>



# Glossary

Abbreviation	Description
ATP	adenosine triphosphate
BW	spectral bandwidth
CRLB	Cramér-Rao lower bounds
CSF	cerebro-spinal fluid
CSI	chemical shift imaging
FLASH	fast low angle shot
FOV	field-of-view
FWHM	full width at half maximum
LB	line broadening
LCModel	linear combination of model spectra
MR	magnetic resonance
NA	number of averages
OVS	outer volume suppression
RF	radio-frequency
ROI	region-of-interest
SRF	spatial response function
STEAM	stimulated echo acquisition mode
T1	spin-lattice-relaxation time
T2	spin-spin-relaxation time
TCA	tricarbalic acid
TE	echo time
TM	mixing time
TMS	tetra-methyl silane
TR	repetition time
VAPOR	variable pulse power and optimized relaxation delays
V1	primary visual cortex

# Introduction

The first magnetic resonance absorption experiment was done in 1939 and proved the existence of a nuclear magnetic momentum [1]. The finding of the effect of nuclear magnetic resonance (MR) in condensed matter at the end of 1945 opened a completely new field of physical research [2, 3]. The basis of MR spectroscopy was laid 4 years later, when the dependence of the resonance frequency of a nucleus on its chemical environment was discovered [4, 5]. The initial MR applications were limited to physics and chemistry. In 1973, however, a method to spatially encode the nuclear spin density was presented such that the first MR imaging method was provided [6]. Since then an enormous effort was made to improve the hardware and the techniques for MR imaging and spectroscopy. Today's MR methods are able to measure biophysical parameters as different as metabolite concentrations, functional activity or microscopic diffusion. MR spectroscopy is not only used in analytical chemistry to retrieve information about chemicals, but also *in vivo* to obtain quantitative information about biologically active compounds from living subjects. The techniques are of great importance particularly in medicine and neuroscience, because they allow the non-invasive assessment of neurochemical profiles of localized brain regions [7, 8].

Neurotransmitters and substances of the brain's energy metabolism are directly linked to functional activity in the brain [9]. The brain metabolism consists of complex mechanisms not only at the gross anatomical scale, but also with an extensive cellular heterogeneity [10]. The spatial resolution of spectroscopic investigations in the human, however, is strongly limited due to the small metabolite concentrations in the brain and the inherently low sensitivity of MR spectroscopy when based on the Boltzmann spin polarization. Therefore, up to now, these techniques are not appropriate to study localized effects in the brain.

The aim of the thesis was to push ahead the spatial resolution limit for single volume MR spectroscopy and chemical shift imaging of the visual cortex to *cortical* dimensions. Resolution improvements by 2–3 orders of magnitude were required compared to similar studies in the human. At the same time the signal strength and the spectral quality should enable the separation and quantification of a maximum number of brain metabolites with focus on those involved in the brain's energy metabolism or neurotransmission.

To this end, high quality MR spectroscopy methods needed to be established and optimized. Potential artifacts that could reduce the sensitivity of  $^1\text{H}$  MR spectroscopy or the amount of information available from the spectra were to be analyzed and correction methods were to be developed.

# Chapter 1

## Physical Basics of Magnetic Resonance

In this chapter the relevant physical concepts related to the phenomenon of nuclear magnetic resonance are summarized. The origin of MR spectra is introduced and the effects of nuclear coupling, relaxation or time dependent magnetic fields are discussed. Magnetic field gradients, imaging and related artifacts are presented. The importance of the homogeneity of the magnetic field for the spectral data quality is rationalized. Finally, the k-space concept is introduced which is essential for the understanding of chemical shift imaging (CSI) techniques.

Standard text book knowledge has been taken mainly from the references [11–15]. For the sake of clarity, literature citations are used in this chapter only when particular studies or work is referred to.

### 1.1 Spin Magnetization

For a nuclear spin with the angular momentum  $\hat{I}$  in a static magnetic field  $B_0$ <sup>1</sup> the Zeeman Hamiltonian is given by

$$\hat{H}_z = -\gamma\hbar B_0 \hat{I}_z \quad (1.1)$$

with  $B_0$ , by convention, aligned with the z-axis and  $\hbar I_z$  being the z-component of the angular momentum operator  $\hat{I}$ . The nuclear spin  $\vec{I}$  is proportional to the magnetic

---

<sup>1</sup>Here and in the following the letter  $B$  is used to describe the magnetic field. A distinction between magnetic field and magnetic induction is only made when it is explicitly required.

moment  $\vec{\mu}$  of the nucleus according to  $\vec{\mu} = \gamma\hbar\vec{I}$  with  $\gamma$  being the nucleus specific gyromagnetic ratio. For the hydrogen nucleus which consists of a single proton and is the only nucleus considered here, the gyromagnetic ratio is  $\gamma/2\pi = 42.577\text{MHz/T}$ . Without an external magnetic field ( $B_0 = 0$ ), the two energy eigenvalues of the

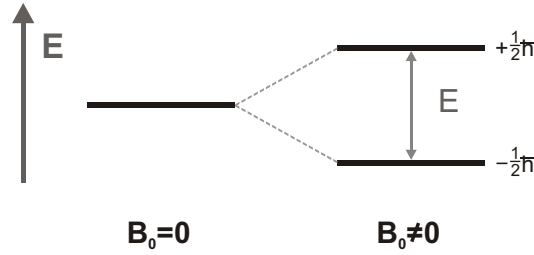


**Figure 1.1:** Zeeman splitting of nuclear spin states. Without an external magnetic field ( $B_0 = 0$ ), the energy eigenstates  $\alpha$  and  $\beta$  of the spin  $1/2$  particle are degenerated. For  $B_0 \neq 0$ , Zeeman splitting is observed.

spin  $1/2$  particle are degenerated and no Zeeman splitting is observed. For  $B_0 \neq 0$ , however, two different energy eigenstates  $\mp 1/2\gamma\hbar B_0$  exist for  $I_z = \pm 1/2$  with an energy difference  $\Delta E = \gamma\hbar B_0$ .

For an ensemble of non-interacting particles at thermodynamic equilibrium the population probabilities of the two possible spin states  $P_\alpha$  and  $P_\beta$  (with  $P_\alpha + P_\beta = 1$ ) follow the Boltzmann law

$$\frac{P_\alpha}{P_\beta} = \exp\left(\frac{\gamma\hbar B_0}{k_B T}\right) \quad (1.2)$$

with  $k_B$  being the Boltzmann constant ( $k_B = 1.38 \cdot 10^{-23} \text{JK}^{-1}$ ). For room temperature (300 K) and  $B_0$  fields of a few Tesla, a spin polarization of  $\sim 10^{-5}$  is induced for  $^1\text{H}$  nuclei that is aligned with  $\vec{B}_0$ . Notably, the small Boltzmann spin polarization results in an inherently low sensitivity of magnetic resonance techniques and is the major limitation for conducting MR experiments.

The first order expansion of the equilibrium polarization for temperatures  $T \gg 0$  (*high temperature approximation*) together with  $\vec{M}_0 = N(P_\alpha - P_\beta)\vec{\mu}$  for  $N$  being the total number of spins then leads to the observable macroscopic magnetic moment of an ensemble of spins

$$\vec{M}_0 = \frac{N\gamma^2\hbar^2}{4k_B T}\vec{B}_0 \quad . \quad (1.3)$$

Based on the stationary spin ensemble, the time development of a spin system now can be described by the *Liouville equation* (or *density operator equation*).

$$\frac{d}{dt}\hat{\rho} = 2i\pi [\hat{\rho}, \hat{H}(t)] \quad (1.4)$$

## 1.2 Bloch Equations and Relaxation

Based on equation (1.4) the time evolution of the magnetization can be calculated to

$$\frac{d}{dt}\vec{M} = -\gamma\vec{M} \times \vec{B}_0 \quad . \quad (1.5)$$

When the spin system encounters in a non-equilibrium state, e.g. after RF excitation (see section 1.3), it will return to the equilibrium state. This process called *relaxation*, however, is not included in equation (1.5). In general, relaxation of the magnetization vector can be described by two characteristic parameters based on the behavior of different vector components:

The magnetization component parallel to the main magnetic field  $\vec{B}_0$  is called *longitudinal* magnetization and the corresponding relaxation process, therefore, is called *longitudinal* or *spin-lattice-relaxation*. It is described by the time constant  $T1$ . The projection of the magnetization vector to the plane perpendicular to the main magnetic field  $\vec{B}_0$  is called *transverse* magnetization and the corresponding relaxation process is called *transverse* or *spin-spin-relaxation*. It is described by the time constant  $T2$ . The total time-development of the magnetization vector is then achieved by the combination of precession and relaxation processes, described by the *Bloch equations*

$$\frac{d}{dt}M_z = -\gamma(\vec{M} \times \vec{B}_0)_z + \frac{M_0 - M_z}{T1} \quad (1.6)$$

$$\frac{d}{dt}M_{x,y} = -\gamma(\vec{M} \times \vec{B}_0)_{x,y} - \frac{M_{x,y}}{T2} \quad . \quad (1.7)$$

These equations have the solutions

$$M_x = M_0 \exp(-t/T2) \cos(\omega_0 t) \quad (1.8)$$

$$M_y = M_0 \exp(-t/T2) \sin(\omega_0 t) \quad (1.9)$$

$$M_z = M_0 [1 - \exp(-t/T1)] \quad . \quad (1.10)$$

The transverse component of the magnetization  $\vec{M}_{xy}$  rotates around the axis of the static magnetic field  $\vec{B}_0$  with the characteristic Larmor frequency  $\omega_0$

$$\omega_0 = 2\pi\nu_0 = \gamma B_0 \quad . \quad (1.11)$$

This process is called *Larmor precession* and can be measured as an induction signal with an RF antenna since the transverse components  $M_{x,y}$  are physical observables. Because of the decay of the transverse magnetization due to relaxation, however, a *FID* (Free Induction Decay) signal is observed, i.e. a sinusoidal function with an exponential damping (Fig. 1.2)<sup>2</sup>.

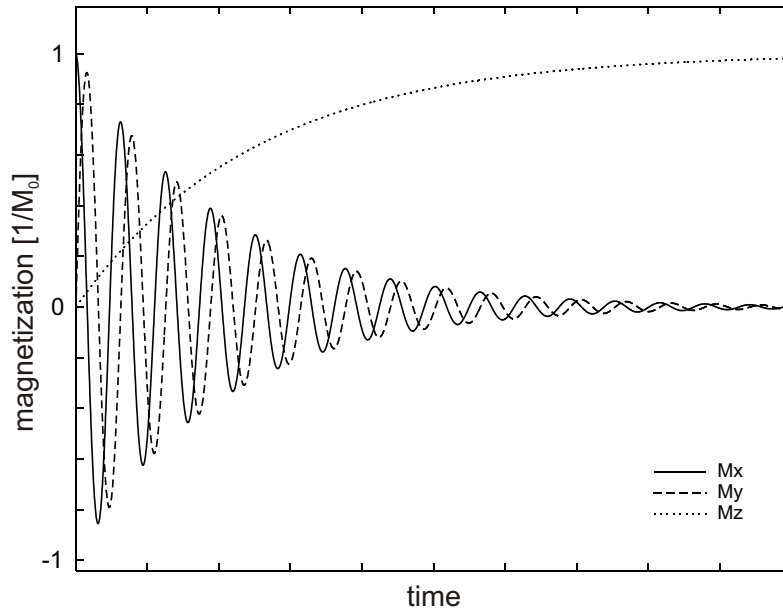


**Figure 1.2:** Free induction decay (FID) of the transverse magnetization components  $M_{x,y} \neq 0$ . The sinusoidal functions are exponentially damped with time constant  $T_2$  (or  $T_2^*$ ). The longitudinal magnetization  $M_z$  returns to its thermodynamical equilibrium value  $M_0$  with the time constant  $T_1$ .

If the magnetic field distribution within the sensitive region-of-interest is not homogeneous, the spin-spin-relaxation time  $T_2$  is further reduced. In case of a field profile with a Lorentzian frequency distribution a parameter  $T_2^*$  can be defined by

$$\frac{1}{T_2^*} = \frac{1}{T_2} + \gamma \Delta B_0 \quad (1.12)$$

<sup>2</sup>For presentation purposes  $T_1 \sim T_2$  was chosen in figure 1.2

with  $\Delta B_0$  being the inhomogeneity of the  $B_0$  field. The total signal  $s(t)$  of a spin density distribution  $\rho(\vec{r}, \nu)$  of nuclei at positions  $\vec{r}$  and with frequencies  $\nu$  is then given by

$$s(t) = \iint \rho(\vec{r}, \nu) e^{-t/T_2^*} e^{2\pi i \nu t} d\vec{r} d\nu \quad . \quad (1.13)$$

The signal constituents can be calculated by Fourier transform of the measured FID signal. The spectral lines, however, are convoluted with a Lorentzian line shape based on the factor  $e^{-t/T_2^*}$ .

### 1.3 Radio-Frequency Excitation

The equilibrium magnetization  $\vec{M}_0$  is purely longitudinal, i.e. it is aligned with the static magnetic field  $\vec{B}_0$ . An observable transverse component  $\vec{M}_{xy}$  of the magnetization perpendicular to  $\vec{B}_0$  is only observed when the equilibrium state is distorted. This is achieved by radio-frequency (RF) irradiation of the spin system that causes transitions between the spin states. To incorporate this effect in the Hamiltonian, the static main magnetic field  $\vec{B}_0$  of the stationary Hamiltonian in equation (1.1) has to be extended by a circularly polarized magnetic field  $B_1$  (with  $\omega_1 = \gamma B_1$ ) perpendicular to  $\vec{B}_0$

$$\hat{H}_{RF}(t) = -\omega_0 \hat{I}_z - \omega_1 \left( \hat{I}_x \cos(\omega t) - \hat{I}_y \sin(\omega t) \right) \quad . \quad (1.14)$$

If the coordinate system is rotated around  $\vec{B}_0$  with the angular frequency  $\omega$  (*rotating frame*), an effective Hamiltonian  $\hat{H}_{eff}$  can be defined

$$\hat{H}_{RF_{eff}} = -(\omega_0 - \omega) \hat{I}_z - \omega_1 \hat{I}_x \quad . \quad (1.15)$$

For an irradiation frequency fulfilling the Larmor condition ( $\omega = \omega_0$ ), the effective Hamiltonian reduces to  $-\omega_1 \hat{I}_x$ , i.e. a magnetization vector that rotates with the frequency  $\omega_1$  around the x-axis. The rotation angle due to the RF irradiation is determined by the  $B_1$  RF field and the duration of the irradiation  $\tau$  according to

$$\alpha = \gamma \int_{t=0}^{\tau} B_1(t) dt \quad . \quad (1.16)$$



## 1.4 Chemical Shift

Based on the Larmor condition (equ. (1.11)), the resonance frequency of a nucleus is given by its gyromagnetic ratio and the magnetic field. If the nucleus is not free but part of a chemical compound, (in most cases) a shielding  $\sigma$  of the external field  $B_0$  by the surrounding electrons is observed (*screening*) [4,5]. The Zeeman Hamiltonian  $H_z$  therefore becomes

$$\hat{H}_z = -\gamma\hbar(1 - \sigma)B_0\hat{I}_z \quad \text{with} \quad 0 < \sigma < 1. \quad (1.17)$$

The related shift of a nucleus' MR frequency is called *chemical shift* and its measurement provides a main concept of MR spectroscopy. To this end, a chemical shift value  $\delta$  is determined which is usually in the order of *ppm* (parts per million)

$$\delta[ppm] = \frac{\omega - \omega_{ref}}{\omega_{ref}} \cdot 10^6 \quad . \quad (1.18)$$

The shifted Larmor frequencies  $\omega$  are assigned relative to a frequency reference  $\omega_{ref}$  that must be stable for experimental variations of relevant parameters like the pH value<sup>3</sup> or the sample temperature. Since the electronic shielding is field dependent, the frequency shifts are further normalized by the same reference. The chemical shift value  $\delta$  then provides a frequency measure of the electronic shielding that is independent of the applied external magnetic field strength.

Substances providing frequency standards like tetra-methyl silane (TMS) are added for *in vitro* experiments in solutions. This is not possible *in vivo* in the brain and internal standards like the 2.02 ppm methyl singlet of NAA are used (see section 3.3).

---

<sup>3</sup>The pH value is defined as the negative decadic logarithm of the H<sup>+</sup> ion concentration

## 1.5 Dipolar Coupling

Hydrogen nuclei may directly couple one another based on their nuclear spin and the related magnetic moment  $\vec{\mu}$ . The total Hamiltonian therefore has to be extended by a term  $H_D$  for the *dipolar coupling* of two nuclei  $N$  and  $M$ .  $H_D$  is proportional to the *direct coupling*  $D_{NM}$  [13]

$$\hat{H}_D \propto D_{NM} \equiv -\frac{\mu_0}{4\pi} \frac{\gamma_N \gamma_M h}{8\pi^2} \frac{(3 \cos^2 \theta_{NM} - 1)}{r_{NM}^3} \quad (1.19)$$

with  $\theta_{NM}$  being the angle between the distance vector  $\vec{r}_{NM}$  of the nuclei and the z-axis, i.e. the direction of the magnetic field  $\vec{B}_0$ . Due to the cubic distance dependence of the dipolar coupling, it is quite small and can be observed only for very close nuclei. In solids with static geometrical conditions the consequences of the dipole-dipole interaction are apparent. In solutions of low viscosity the molecular tumbling due to the Brownian motion reduces the correlation times between nuclei and the dipolar coupling may be averaged out. This is the regular case for *in vivo* MR spectroscopy of freely moving brain metabolites of low molecular weight [7]. The dipolar coupling, however, leads to broadened resonances for macromolecules [16–20].

## 1.6 J-Coupling

Nuclei in a molecule may not only couple in a direct way, but also indirectly via their chemical bindings. Since the nuclei do not interact directly themselves, but their spin states are correlated by the binding electrons, this type of interaction is called J-coupling. For two nuclear spins  $\hat{N}$  and  $\hat{M}$  the Hamiltonian of the J-coupling  $\hat{H}_J$  is given by

$$\hat{H}_J = J_{NM} \hat{N} \cdot \hat{M} \quad . \quad (1.20)$$

This weak scalar coupling has to be included into the total Hamiltonian and leads to a shift of the Zeeman niveaus based on the nuclear spin states. Corresponding shifts are proportional to the magnetic moment of the coupled nucleus that caused the multiplet splitting and therefore determined by the magnetic spin quantum number and the multiplicity of the coupled nucleus. The peak intensities are given by the probabilities of the particular spin states. J-couplings are assigned in Hertz and values for  $^1\text{H}$ - $^1\text{H}$  couplings are in the range of 1–15 Hz, whereas values of 100–200 Hz are observed for  $^1\text{H}$ - $^{13}\text{C}$  couplings [21].

The absolute values of the chemical shift depend on the strength of the external magnetic field, however the J-values do not. Therefore, the global appearance of the MR spectrum becomes strongly field dependent. If the chemical shift differences of a compound are big compared to its J-coupling constants ( $|\Delta\nu| \gg J$  with  $\omega = 2\pi\nu$ ), the spectrum is considered to be of *first order*. Magnetically equivalent nuclei, i.e. nuclei that have the same coupling constant J with respect to another nucleus, do not show J-coupling between themselves due to quantum-mechanical selection rules (e.g.  $\text{CH}_3$  of NAA at 2.02 ppm). If more than 2 first order nuclei are coupled, the complete spectrum can be deduced by a stepwise consideration of the particular couplings. *Second order* spectra for which the J-values and the chemical shift differences are in the same range, however, can only be derived from the full quantum-mechanical description [22].

## 1.7 Magnetic Field Gradients

Magnetic field gradients are used to achieve a spatial dependence of the Larmor resonance condition (equ. (1.11)) and are the basis for all types of localization and imaging techniques in MR experiments

$$G_x = \frac{\partial B_z}{\partial x}, \quad G_y = \frac{\partial B_z}{\partial y}, \quad G_z = \frac{\partial B_z}{\partial z} \quad . \quad (1.21)$$

The gradient fields are superimposed to the MR scanners' static  $B_0$  field

$$B(x, y, z) = B_0 + xG_x + yG_y + zG_z \quad (1.22)$$

and make the Larmor resonance frequency with  $\omega(x, y, z) = \gamma B(x, y, z)$  become dependent on position. In general, the gradient fields are at least one order of magnitude smaller than the  $B_0$  field.

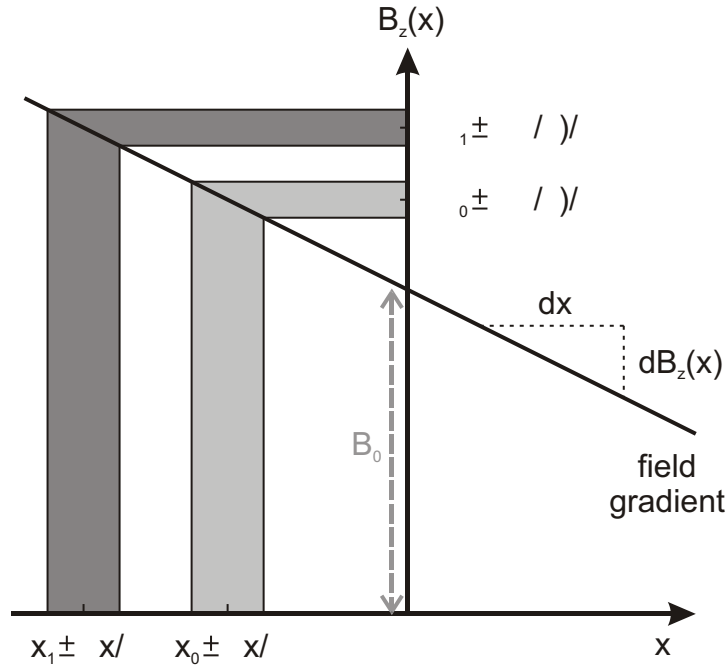


**Figure 1.3:** *Magnetic field gradients and chemical shift displacement. When a field gradient  $G_x = \partial B_z / \partial x$  is superimposed to the main  $B_0$  field, the Larmor frequency  $\omega$  becomes dependent on position. For a RF pulse with a center frequency  $\omega_0$  and a bandwidth  $\Delta\omega$  the Larmor condition is fulfilled only in a particular spatial region  $x_0 \pm \Delta x / 2$  and only those spins are affected by the RF pulse (bright gray). A different chemical shift  $\omega_1$  then leads to a different spatial encoding (dark gray), i.e. the chemical shift displacement (CSD).*

## 1.8 k-Space

For a point-like sample the magnetization performs a precession at a constant angular frequency. If relaxation effects are neglected the measured signal  $s(t)$  in the rotating frame (see section 1.3) therefore is given by

$$s(t) = s_0 e^{2\pi i \nu t} \quad . \quad (1.23)$$

If a magnetic field gradient  $\vec{G}(t)$  is applied, the Larmor frequency becomes time dependent and the angular frequency is no longer constant

$$\omega(t) = \gamma \vec{G}(t) \vec{r}, \quad s(t) = s_0 e^{i\gamma \int_0^t \vec{G}(t) \vec{r} dt} \quad . \quad (1.24)$$

Using the definition

$$\vec{k} = \frac{\gamma}{2\pi} \int_0^t \vec{G}(t') dt' \quad (1.25)$$

and based on the superposition principle the total signal from a spin density distribution  $\rho(\vec{r})$  can then be calculated by spatial integration of all signal contributions

$$s(\vec{k}) = \int \rho(\vec{r}) e^{i\gamma \int_0^t \vec{G}(t) \vec{r} dt} d\vec{r} = \int \rho(\vec{r}) e^{2\pi i \vec{k} \vec{r}} d\vec{r} \quad . \quad (1.26)$$

The signal representation in k-space and the spin density distribution in image space build a Fourier pair and, therefore, can be directly transformed one to the other and vice versa

$$\rho(\vec{r}) = \int s(\vec{k}) e^{-2\pi i \vec{k} \vec{r}} d\vec{k} \quad . \quad (1.27)$$

In MR imaging experiments, the k-space vector  $\vec{k}$  which corresponds to a particular spatial frequency component, is encoded by a combination of appropriate magnetic field gradients before the magnetization signal is measured. Since experimentally no continuous k-space coverage can be achieved a reasonable sampling grid is to be measured. The discrete Fourier pair corresponding to equations (1.26) and (1.27) in two dimensions is then given by [23]

$$s(k_{lx}, k_{my}) = \frac{1}{N_x N_y} \sum_{l=1}^{N_x} \sum_{m=1}^{N_y} \rho(x_l, y_m) e^{-i \frac{2\pi}{N_x} k_{lx} x_l} e^{-i \frac{2\pi}{N_y} k_{my} y_m} \quad (1.28)$$

$$\rho(x_l, y_m) = \frac{1}{N_x N_y} \sum_{l=1}^{N_x} \sum_{m=1}^{N_y} s(k_{lx}, k_{my}) e^{i \frac{2\pi}{N_x} k_{lx} x_l} e^{i \frac{2\pi}{N_y} k_{my} y_m} \quad (1.29)$$

Sampling information from a grid of k-space points provides the data matrix necessary to reconstruct morphological/anatomical images with

$$\Delta k = \frac{1}{FOV} \quad (1.30)$$

The spacing of the sampling points in k-space  $\Delta k$  is determined by the targeted FOV. If signal contributions from outside the FOV exist, they are folded back into the FOV and lead to an artifactual localization (*aliasing*). The (nominal) spatial resolution  $\Delta x$  in image space is then determined by the FOV size and the dimension of the k-space sampling matrix  $N$

$$\Delta x = \frac{FOV}{N} \quad (1.31)$$

The k-space concept was mainly introduced to provide a better understanding of MR sequences [24, 25] and proved its usefulness particularly for the development of fast imaging techniques [26].

## 1.9 Chemical Shift Displacement

As described in the sections 1.4 and 1.6 the dependence of the Larmor frequency on chemical shift and J-coupling is the basis of MR spectroscopy and is used to identify metabolites based on their spectral pattern. Magnetic field gradients, however, use the same frequency dependence to encode spatial position. This ambiguity is the origin of an artifact called *chemical shift displacement* (CSD), i.e. a differing spatial encoding based on the particular metabolic chemical shifts<sup>4</sup> (Fig. 1.3). For

---

<sup>4</sup>The term *chemical shift* is often used to summarize both the actual chemical shift as well as J-coupling effects

single voxel spectroscopy the artifact leads to shifts of the voxel position, in MR imaging the consequence is an CSD artifact along the frequency encoding direction. A strategy to minimize the CSD is to increase the strength of the encoding magnetic field gradients. Thereby, the frequency bandwidth per spatial length is increased and the chemical shift differences become less relevant.

## 1.10 Field Homogeneity

All MR methods are based on the same Larmor condition (equ. (1.11)) which relates the resonance frequency to the static  $B_0$  field of the MR scanner. If the magnetic field within the region-of-interest is varying, i.e. it is inhomogeneous, the consequence are position dependent shifts of the Larmor frequency<sup>5</sup>. A non-homogeneous distribution of the magnetic field within the sensitive probe volume therefore leads to a broadening of spectral peaks and a reduction of the signal-to-noise ratio (SNR). Furthermore, the distribution of the magnetic field has a direct impact on the line shape of spectral peaks, which may lead to quantification errors, if inappropriate model functions are used [27–29].

### 1.10.1 Magnetic Susceptibility

If a material is exposed to a magnetic field  $\vec{H}$ , the magnetic moments of the material interact with the external field and an overall magnetic induction  $\vec{B}$  is observed<sup>6</sup>

$$\vec{B} = \mu_0(\vec{H} + \vec{M}) \quad . \quad (1.32)$$

$\mu_0 = 4\pi \cdot 10^{-7} \text{VsA}^{-1}\text{m}^{-1}$  is the vacuum permeability and  $\vec{M} = \vec{m}/V$  is the magnetization of the object, i.e. the induced magnetic moment  $\vec{m}$  per volume  $V$ . The magnetization  $\vec{M}$  describes the degree to which a sample is magnetized in an external magnetic field and is commonly expressed by the volumetric magnetic susceptibility  $\chi_m$

$$\vec{M} = \chi_m \vec{H} \quad . \quad (1.33)$$

The magnetic susceptibility  $\chi_m$  is a dimensionless factor and substances with a magnetic susceptibility  $\chi_m < 0$  are classified as diamagnetic. Materials with  $\chi_m > 0$  are called paramagnetic while ferromagnetic substances have  $\chi_m \gg 1$ .

<sup>5</sup>The magnetic field variations  $\Delta B$  within the ROI are assumed to be small compared to the scanner  $B_0$  field, i.e. the spectral pattern remains unchanged

<sup>6</sup>Here an explicit distinction is made between the magnetic field  $H$  and the magnetic induction  $B$

When ferromagnetic objects are magnetized by an external magnetic field, the magnetization curve is a non-linear function of the magnetization field strength and hysteresis is observed [30]. In the literature, often the polarization  $J = \mu_0 M$  is used instead of the magnetic susceptibility  $\chi_m$ .

### 1.10.2 Biological Samples in a Magnetic Field

MR scanners are designed to provide static homogeneous fields in nearly spherical target volumes around the iso-center. This center region of the magnet is used for MR experiments and must have the appropriate size for the sample to be measured. This is achieved by appropriate design of the superconducting  $B_0$  coil and additional field profiling with tons of iron. Residual inhomogeneities are minimized by a one-time passive shimming during scanner installation [31–33]. Due to the thereby achieved good field homogeneity of a modern MR scanner, experimental field distortions are clearly dominated by those induced by the magnetically susceptible probe placed inside the scanner. At the boundary of two media having different magnetic susceptibilities, the component of the magnetic induction  $\vec{B}$  perpendicular to the interface must be continuous since no sources exist ( $\vec{\nabla} \cdot \vec{B} = 0$ ). Brain tissue, bone, cerebro-spinal fluid (CSF), i.e. mainly water, and skin are diamagnetic [34–36]. But the magnetic susceptibility of air is  $\sim 1$ , so that strong field distortions are observed around transitions from tissue and bone to air like at the inferior prefrontal cortex, the inferior temporal lobe or adjacent to the skull surface [37–39].

### 1.10.3 Mapping and Analysis of Magnetic Fields

Magnetic field distributions in the brain can be directly measured with MR methods based on the considerable water content in brain tissue. According to the Larmor equation (equ. (1.11)) the magnetization accumulates a phase  $\phi$  between spin excitation and the formation of a gradient echo, i.e. during the echo time  $TE$ . A difference in echo time  $\Delta TE$  of two similar scans thereby leads to a difference in the magnetization phase  $\Delta\phi$  and relative field distributions can be calculated. The magnetic field strength and the frequency  $\nu$  provide the identical information based on the Larmor equation

$$\nu = \frac{1}{2\pi} \frac{\Delta\phi}{\Delta TE} \quad . \quad (1.34)$$



### 1.10.4 Spherical Harmonics Decomposition

The Laplace equation  $\Delta\Psi = 0$ , with  $\Psi$  being the magnetic scalar potential, holds in a volume that is free of sources of magnetic flux [40, 41]. Every solution of the Laplace equation can be represented in the infinite basis of the spherical harmonic functions [41]:

$$\Psi(r, \phi, \theta) = \sum_{m=0}^{\infty} \sum_{n=m}^{\infty} (A_n^m \cos(m\phi) + B_n^m \sin(m\phi)) r^n P_n^m(u) \quad (1.35)$$

with  $u = \cos\theta$  and  $P_n^m$  being the associated Legendre functions. The parameters  $r$ ,  $\theta$  and  $\phi$  assign the position in polar coordinates. In this expression, the field term  $r^n P_n^m(u)$  contains the spatial dependence of the spherical harmonic functions [42].

The z-axis of modern MR scanners, by convention, is chosen to be aligned with the  $\vec{B}_0$  field. From equation (1.35) the z-component of the magnetic field can be calculated by differentiation of the magnetic scalar potential  $\Psi$  with respect to z [40, 41]

$$B_z = \frac{\partial\Psi}{\partial z} = - \sum_{m=0}^{\infty} \sum_{n=m+1}^{\infty} (A_n^m \cos(m\phi) + B_n^m \sin(m\phi)) r^{n-1} (n+m) P_{n-1}^m(u). \quad (1.36)$$

In table 1.1 the first-to-fourth order spherical harmonic terms  $\psi_n^m(r, \theta) = r^n P_n^m(\cos\theta)$  are summarized ( $n = 1, \dots, 4$ ;  $m = -n, \dots, +n$ ) in cartesian coordinates. Furthermore, the first and second order spherical harmonics are visualized in figure 1.4 for a unity sphere ( $r = 1$ ).

Since every static magnetic field can be decomposed into spherical harmonic functions (or Legendre polynomials), the deviations of a magnetic field distribution from homogeneity can be also expressed in that basis [43]. If modular and calibrated magnetic fields corresponding to the spherical harmonic functions are available, inhomogeneities of an arbitrary field distribution can be minimized (see section 2.7).

**Table 1.1:** First-to-fourth order spherical harmonic functions. For  $n = 1, \dots, 4$  and  $m = -n, \dots, +n$  the term  $\psi_n^m(r, \theta) = r^n P_n^m(\cos\theta)$  is expressed in cartesian coordinates. The abbreviated names are assigned according to the dominating field term.

abbreviation	order (n)	degree (m)	function
X	1	1	$x$
Z	1	0	$z$
Y	1	-1	$y$
X2-Y2	2	2	$3(x^2 - y^2)$
ZX	2	1	$3zx$
Z2	2	0	$z^2 - 1/2(x^2 + y^2)/2$
ZY	2	-1	$3zy$
XY	2	-2	$6xy$
X3	3	3	$15x(x^2 - 3y^2)$
Z(X2-Y2)	3	2	$15z(x^2 - y^2)$
Z2X	3	1	$3/2x[4z^2 - (x^2 + y^2)]$
Z3	3	0	$z[z^2 - 3/2(x^2 + y^2)]$
Z2Y	3	-1	$3/2y[4z^2 - (x^2 + y^2)]$
XYZ	3	-2	$30xyz$
Y3	3	-3	$-15y(y^2 - 3x^2)$
X4+Y4	4	4	$105(x^4 - 6x^2y^2 + y^4)$
X3Z	4	3	$105xz(x^2 - 3y^2)$
Z2(X2-Y2)	4	2	$15/2(x^2 - y^2)[(6z^2 - (x^2 + y^2))]$
XZ3	4	1	$5/2xz[4z^2 - 3(x^2 + y^2)]$
Z4	4	0	$z^4 - 3z^2(x^2 + y^2) + 3/8(x^2 + y^2)^2$
YZ3	4	-1	$5/2yz[4z^2 - 3(x^2 + y^2)]$
XYZ2	4	-2	$15/2xy[(6z^2 - (x^2 + y^2))]$
Y3Z	4	-3	$105yz(3x^2 - y^2)$
X3Y	4	-4	$420xy(x^2 - y^2)$

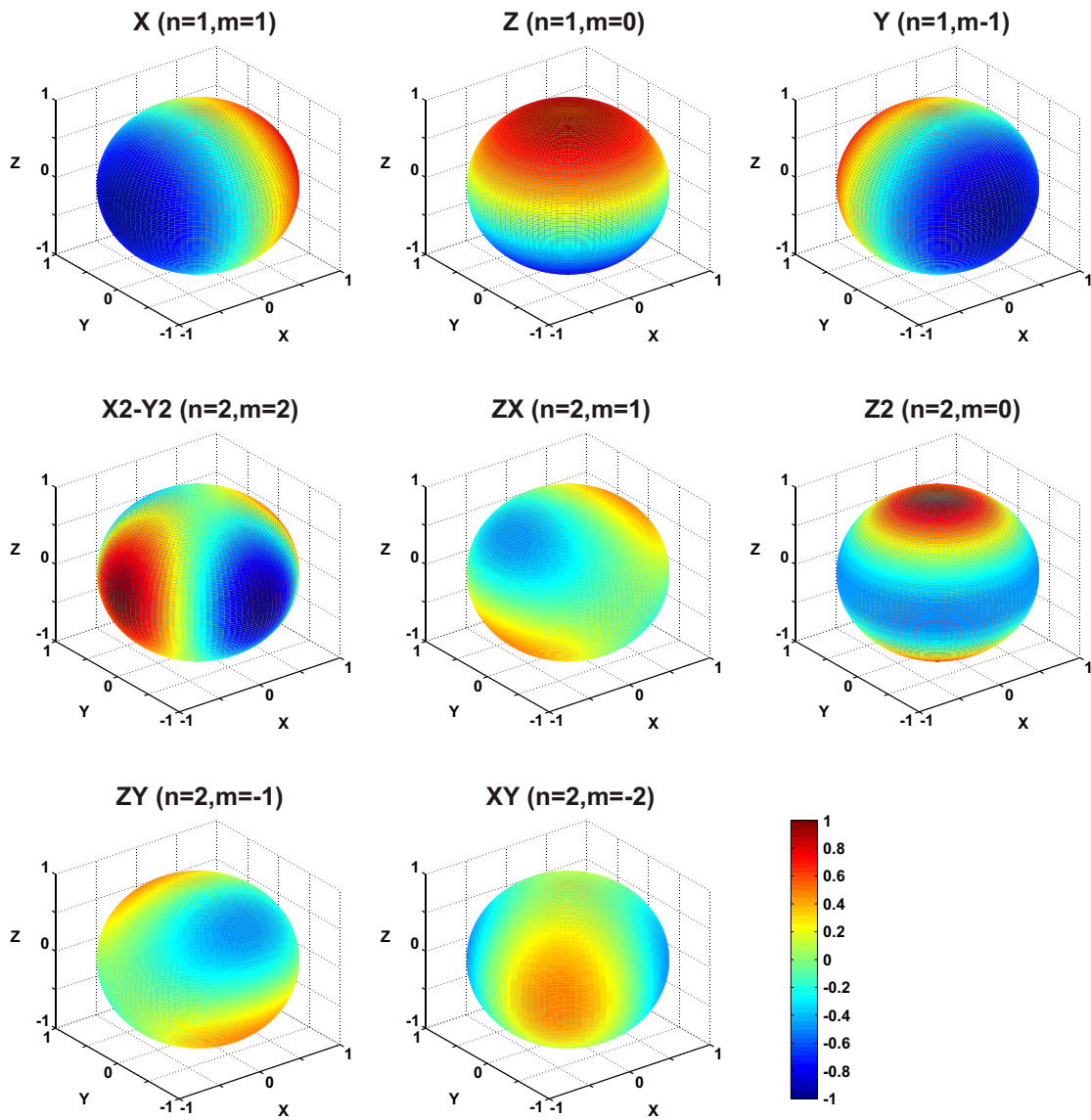


**Figure 1.4:** First and second order spherical harmonic functions. The functions have been normalized for the unity cube volume to the  $[-1, 1]$  range and are visualized for a unity sphere.

# Chapter 2

## Techniques for $^1\text{H}$ MR Spectroscopy

### 2.1 Single Voxel Spectroscopy

During the last 20 years a variety of different pulse sequences have been proposed for *in vivo* single voxel spectroscopy [44]. They mainly differ by the way the excitation pulses are used (slice selective versus non-slice selective) and by the number of acquisitions required to generate a volume localized spectrum. Recently, the so-called *single-shot* techniques PRESS (Point RESolved Spectroscopy, [45]) and STEAM (STimulated Echo Acquisition Mode, [46]) prevailed since only one acquisition is needed for the volume localization. The susceptibility to artifacts, therefore, is inherently lower compared to *multi-shot* techniques where several acquisitions are necessary.

In general, three subsequent 90 degree RF pulses are known to generate three FIDs, four normal spin-echoes and one stimulated echo [47]. Their timing depends on the RF pulse timing and the relative amplitudes are determined by the nutation angles. Magnetic field inhomogeneities, however, may produce additional *multiple* echoes. For localized spectroscopy with STEAM, slice-selection gradients are added during the irradiation of the RF pulses to select a particular voxel volume that corresponds to the intersection of the three slices [46](Fig. 2.1). Since only the stimulated echo is to be acquired, several so-called crusher gradients are used to dephase the other signals. Magnetization outside the selected STEAM voxel is not exposed to all three RF pulses and is therefore not refocused or not even excited. Phase cycling schemes are also possible to eliminate unwanted echoes, but they are less preferable, since the single-shot character of the method would be lost.

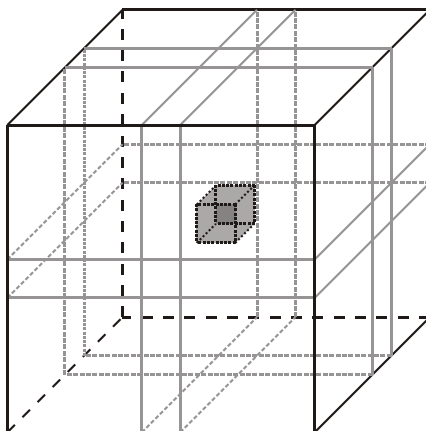


**Figure 2.1:** *STEAM localization. The spatially selective excitation of a cube volume with STEAM for *in vivo* MR spectroscopy is achieved by 3 slice-selective 90 degree RF pulses. Only the spins within the intersection of the 3 slices experience all pulses and contribute to the stimulated echo.*

Most of the brain metabolites are J-coupled, so that J-coupling, chemical shift and spin displacement lead to a considerable time evolution of the magnetization in a STEAM sequence [48, 49]. During the mixing time  $T_M$  between the pulses #2 and #3 the magnetization has no transverse component and no spin-spin-relaxation is apparent. Consequently, this period doesn't contribute to the echo time  $T_E$  and very short echo times can be realized [8], which is one of the main advantages over the PRESS technique. The theoretically achievable signal for STEAM, however, is only one half of the spin-echo method PRESS (and can be further reduced in real applications [44]). In recent years, shorter echo times were also achieved with PRESS under certain conditions [50] and since sensitivity is inherently critical in *in vivo* MR spectroscopy, the selection of the most appropriate technique depends on the particular experimental design. In this thesis, STEAM was considered the most reasonable sequence due to the realizable short echo times and due to an increased insensitivity to imperfections of the exact RF pulse angles compared to PRESS.

## 2.2 Conventional Chemical Shift Imaging

If MR spectroscopy is extended by a spatial encoding scheme, the signal from a spin density distribution  $\rho(\vec{r}, \nu)$  of equation (1.13) accumulates an additional phase and becomes

$$s(t, \vec{k}) = \iint \rho(\vec{r}, \nu) e^{-t/T2^*} e^{2\pi i \nu t} e^{2\pi i \vec{k} \cdot \vec{r}} d\vec{r} d\nu \quad . \quad (2.1)$$

The Fourier transform of all spatial and the spectral dimension then provides a spatially resolved array of MR spectra rather than a single voxel spectrum only [51, 52]. This chemical shift imaging (CSI) technique (which is also called MR spectroscopic imaging, MRSI) is widely used to measure spatially resolved metabolic maps of the brain. The acquisition time that is necessary to achieve a given SNR is determined by the experimental setup (e.g. magnetic field strength, RF coils) as well as methodological parameters like the field-of-view (FOV) or the required spatial resolution. SNR is proportional to the CSI voxel volume and (for homogeneous k-space coverage) increases with the square root of the acquisition time [53].

The substitution of one phase encoding direction with an echo planar imaging (EPI) readout can reduce the minimal acquisition time considerably [54, 55]. In addition, other fast CSI techniques with different types of gradient wave forms [56, 57] or a SPIRAL readout [58] are used to minimize the minimal acquisition time for CSI. The conventional phase encoding and the fast CSI techniques, however, share the same dependence on the acquired SNR per time [44, 56]. In other words, there is no net gain in data acquisition speed with the fast techniques and more averaging is required for the fast techniques to achieve the sensitivity of conventional CSI. But higher demands on the gradient performance for the fast techniques and an increased susceptibility to artifacts make these techniques less preferable than the conventional phase encoding for the purpose of acquiring a maximum number of  $^1\text{H}$  brain metabolites at maximum spectral quality.

## 2.3 Acquisition Weighted Chemical Shift Imaging

A reduction of spatial contaminations resulting in an improved spatial response function (SRF) can be achieved by applying a spatial low-pass filter to the k-space data. This can be done either as post-processing or by a corresponding k-space sampling scheme during the experiment [52, 54, 59, 60]. The sensitivity of latter approach called acquisition weighted CSI is always higher than after post-processing filtering and makes it the preferable method [61].

Different approaches exist in order to quantify the reduction of spatial resolution for the use of spatial filters either in k-space or in image space (e.g. [15]). Here, a definition for the spatial resolution based on the SRF is used [62, 63]. The SRF describes the signal contributions of the entire FOV to the center voxel position. For a 1D imaging experiment the SRF is given by

$$SRF(x) = \frac{\sin\left(\frac{\pi x}{\Delta x}\right)}{N \cdot \sin\left(\frac{\pi x}{N \cdot \Delta x}\right)} . \quad (2.2)$$

The spatial resolution of the imaging system then can be defined as the minimum distance of two point-like signal sources that still can be separated. Applying the Raighley criterion [64] the width of the central peak of the SRF at 64% of the maximum amplitude is then considered the spatial resolution of the imaging modality. This approach reproduces the definition of the nominal spatial resolution of equation (1.31), since without filtering the width of the SRF at the 64% level corresponds to the voxel size [62](see chapter 8).

## 2.4 Water Suppression

Quantitatively, the biggest part of the human as well as the monkey body consists of water. The water content of all types of tissue is at least 2/3 with the exception of fatty tissue and bones. The exact values are in the range of 40 Mols, but depend on anatomy, sex, age and health status. In the healthy human brain, water concentrations of 83% and 70% were reported for the gray and white matter, respectively [65]. Concentrations of the detectable brain metabolites are, in contrast,  $10^3$ – $10^4$  times smaller [10] and therefore much harder to detect. For a limited dynamic range of

the RF receive channel, the amplitude resolution of the acquired metabolite signals is hampered, when the dynamic range is adjusted to the much stronger water signal. Increased dynamic ranges of state-of-the-art receivers can partially overcome that problem, but baseline distortions are still problematic [66]. Recently, the removal of the water signal by a subtraction scheme of two spectra was presented. In the first acquisition a frequency selective inversion of the metabolite magnetization is applied and hence the metabolites signals are not affected by the subtraction [67, 68]. The direct experimental suppression of the water signal, however, remains the preferable solution to the problem. Most of the water suppression techniques are based on the differing chemical shifts of water and the brain metabolites. If the water is excited exclusively by a frequency selective RF pulse, the water magnetization can be dephased (*spoiled*) without affecting the magnetization of the brain metabolites. This method called CHESS (CHEmical Shift Selective, [69]) can be repeated several times to improve the suppression factor. Since there is no interaction with the metabolite spins in CHESS, water suppression modules can be performed prior to every MR spectroscopy sequence and for STEAM even in the mixing time interval. The creation of unwanted echoes can be avoided by using irregular timing of the suppression modules [70]. Combinations of CHESS with PRESS were published as DRYPRESS [48, 70] those with STEAM as DRYSTEAM [70] and VAPOR [8]. The use of frequency selective pulses for water suppression, however, is inherently restricted to those metabolites that have chemical shifts considerably different from the water protons. The use of numerically optimized RF pulse powers and inter-delays in a series of 7 or 8 suppression modules with VAPOR (VARIABLE Pulse Power and Optimized Relaxation delays), furthermore, has been shown to provide a certain insensitivity of the water suppression from the RF power  $B_1$  and the spin-lattice-relaxation time  $T_1$ . Since this is a major issue for *in vivo* MR spectroscopy, VAPOR has been considered the method of choice here.

## 2.5 Outer Volume Suppression

In practice, RF pulses are time limited and an exact step-function-like frequency profile is not feasible. The STEAM localization pulses therefore have sidebands that lead to spin excitation from outside the required voxel volume. Besides the falsification of quantitative results for the selected MR spectroscopy volume, for *in vivo* MR spectroscopy of the brain those sidebands may cause lipid and fat contaminations originating from the cranial bone. Lipid and fat signals are 100–1000 times stronger than those of the detectable brain metabolites [10] and, therefore, even low amplitude sidebands may lead to strong artifacts [18–20]. Especially, skull



lipids cause broad resonances in the range of 0.9–1.9 ppm and may strongly hamper the spectrum quantification [10]. T2 times of brain metabolites are in the range of 100–500 ms [71] and are longer than those of water ( $\sim 80$  ms, [72]) or fat (1–20 ms, [73]). Consequently, good water and fat suppression are particularly important for MR spectroscopy methods that use short echo time of 10 ms or below. If the magnetization from outside the selected volume, however, is actively spoiled before the STEAM excitation, the risk of artifactual signal contributions is minimized. Several techniques have been proposed for this complementary approach of volume selection, called outer volume suppression (OVS), which mainly differ in the RF pulse profiles, the timing and the repetition modes (LOCUS [69], BISTRO [74]).

## 2.6 Spectrum Quantification

The main goal of MR spectroscopy is the detection and quantification of chemical compounds. *In vivo* MR spectra of the brain, however, consist of a superposition of a variety of more or less complex metabolite spectra [7, 21]. Furthermore, the appearance of the spectrum depends on experimental parameters like the  $B_0$  field strength or the sequence timing. Therefore, a simple integration of peaks is not possible and statistical methods are required to disentangle the spectral information. Different ways have been proposed to assess spectral composites of *in vivo*  $^1\text{H}$  MR spectra of brain metabolites and to achieve a reliable quantification either in time domain [27] or, equivalently, in frequency domain [28].

Here, the frequency domain method *LCModel* was used which determines the best possible fit of the measured spectrum with a Linear Combination of Model spectra [75, 76]. Metabolite concentrations and errors are calculated by a non-linear least square analysis. Differences of the *in vivo* vs. *in vitro* spectra in phase, line shape or baseline are taken into account by a constrained regularization method. The error of the spectral deconvolution and the quantification of substances are given as Cramér-Rao lower bounds (CRLB) which are the lowest possible standard deviations of all unbiased model parameter estimates [77]. Prior knowledge in terms of a set of basis spectra from the potentially detectable metabolites is used with this approach and has to be provided to run the analysis.

The particular metabolite spectra are commonly achieved by measuring them in solutions under identical experimental conditions. The effects of potential sequence imperfections (e.g. gradients or timing) as well as other experimental problems of the particular MR setup (e.g. eddy currents) are then already in the solution spectra and are, therefore, considered properly in the latter *LCModel* analysis. The draw back, however, is the high experimental effort that is needed to prepare the

solutions and to run the experiments. Furthermore any type of modification or readjustment of the MR spectroscopy setup, consisting of hardware or methods requires a new preparation of the short lasting metabolite solutions and the repetition of their measurements. Even if there is no principle limitation for the time frame of *in vitro* experiments, long experiment durations are required to achieve reasonable SNR.

An alternative to the experimental measurement of the brain metabolite spectra is their simulation based on the spectroscopic characteristics of the metabolites, i.e. the chemical shifts, the J-couplings and the number and type of nuclei. This approach is far more flexible and requires only minimal effort, once the computational infrastructure has been provided. In addition, SNR is no issue for simulated spectra and the risk of systematic errors in the analysis of brain spectra, e.g. due to imperfections of the metabolite concentrations in the model solutions, is eliminated. The drawback of the simulation approach is that hardware or experiment specific artifacts are not considered.

The amplitudes of the metabolite signals from *in vivo* MR spectra from the brain depend (besides the spin magnetization of the metabolites) on many experimental parameters like RF coil performance, the voxel geometry, the  $B_0$  field strength, the receive channel characteristics and the MR sequence including the adjustment quality. In practice, an absolute quantification of the metabolite signals and concentrations is difficult and, therefore, quantitative standards are used like a water probe that is placed during the experiment beside the head to be targeted [78]. However, these *external* standards are prone to systematic errors, e.g. due to differing  $B_1$  conditions in the standard and the brain. Well-known *internal* standards like the tissue water [79] or particular brain metabolites from the same MR spectroscopy voxel do not have that problem and are better suited as quantitative references. Mostly, NAA or total creatine (Cr + PCr) are used as internal standard, since these metabolites are easy to detect and to quantify due to their prominent singlet resonances at 2.02 ppm and 3.03 ppm, respectively.

## 2.7 Field Homogenization

### 2.7.1 Field Homogenization: 'Shimming'

The term *shimming* describes the homogenization of the magnetic field inside the volume-of-interest (VOI) for MR examinations [80]. This can be achieved by placing an ensemble of ferromagnetic objects with proper size and position into the magnetic field (*passive shimming*) [40]. Passive shimming is not only used to improve the field homogeneity of the MR scanner, but also to compensate for field distortions induced by the subject [41, 81, 82]. However, a flexible shim method is required to account for varying conditions and passive shimming alone is not well suited to this task, because the physical mounting of many metal pieces is time consuming and inflexible. In practice, the utilization of passive shimming has been mostly limited to special applications like the use of intra-oral passive shimming of the frontal cortex in humans by diamagnetic mouth inserts [38, 83, 84] or shimming the mouse brain by an optimized combination of paramagnetic and diamagnetic passive shims [85]. As stated in section 1.10, magnetic field inhomogeneities can be expressed by spherical harmonic functions. *Active shimming* capitalizes on this principle by using a set of appropriate electrical coils, each generating a magnetic field component that corresponds to one specific spherical harmonic. By superimposing a shim field of the same magnitude but opposite sign to the distortion, the field inhomogeneity is minimized [40, 80, 86–89]. Analytical and iterative approaches have been proposed to optimize the active shimming procedure for accuracy and speed [90–92]. For *in vivo* conditions, it was demonstrated that the inclusion of second- and possibly third-order shim-terms can considerably improve the field homogeneity and thus the data quality for *in vivo* MR spectroscopy [91, 93, 94].

### 2.7.2 Mapping and Analysis of Magnetic Fields

Shimming techniques require the exact knowledge of the field distortion that is to be removed<sup>1</sup>. MR imaging techniques can measure magnetic fields based on equation (1.34) either as the full 3D field distribution [95] or as representative subvolumes. These subvolumes can be like the surface of a sphere (*homogeneity sphere*) [96] or diagonal sticks that cross the region to be analyzed [91]. The advantage of the lat-

---

<sup>1</sup>The passive shimming with diamagnetic mouth inserts is an exception for which the field distortion needs not to be known. The origin of the field distortion is minimized with this technique rather than to compensate the generated inhomogeneities.

ter sparse sampling methods is that the experimental (and computational) time to measure and analyze the field distribution is strongly reduced. If there are strong fluctuations of the magnetic field within the region-of-interest, these techniques, however, bear the risk of missing relevant information.

In this thesis, magnetic fields were measured in two different ways:

For full 3D field mapping, two FLASH (Fast Low Angle SHot) images were acquired at different echo time and the magnetic field distribution was calculated from the corresponding phase images. Based on equation (1.34) the difference in echo time  $\Delta TE$  for two similar scans was used to accumulate a difference in the magnetization phase  $\Delta\phi$  and to calculate the (relative) field distribution in Hertz. If necessary, 3D phase unwrapping [97] was applied before the field decomposition into the spherical harmonic functions with the algorithm presented in [98].

A second way of measuring magnetic field distributions was achieved with the mapping and analysis tool FASTMAP [91, 99]. A sparse sampling algorithm measures the field distribution along diagonal projections through the cube volume to be analyzed. Then, the 3D field distribution is calculated and decomposed into spherical harmonics, before the appropriate shim currents are adjusted to remove the field distortion by active shimming. Here, the FASTMAP sparse sampling was used for a fast determination of 3D field distributions only.

# Chapter 3

## MR Spectroscopy of the Brain

In this chapter the significance of the visual system in neuroscientific research is summarized. Previous MR spectroscopy studies of function in the visual cortex and other brain areas are reviewed and a detailed neuroscientific motivation for the use of high resolution  $^1\text{H}$  MR spectroscopy to explore the living brain is given.

The 20 most prominent brain metabolites from  $^1\text{H}$  MR spectra of the healthy brain are characterized with respect to their chemical structure, their biochemical significance and their spectroscopic properties. This is followed by an analysis of the problems of the spectral separation of some relevant brain metabolites: glutamate versus glutamine and creatine versus phosphocreatine.

### 3.1 MR Spectroscopy in Neuroscience

Understanding what the brain does is one of the most exciting topics in the natural sciences and of high relevance for the diagnosis and treatment of psychiatric and neurologic diseases. The brain is a highly heterogenous and complex system that can perform different tasks such as the evaluation of sensory input, the maintenance of vegetative processes or the body's motor control. Much of what is known about the brain today, was only possible due to the invention of new physical techniques like microscopy, electrophysiology/EEG (electro-encephalography), PET (positron emission tomography) and MR. Nowadays it is known for many brain functions where they are located in the brain. Although localization is a basic requirement and is useful for medical diagnosing and surgical planning, for a true understanding, the knowledge of the underlying mechanisms is needed. For example, MR imaging

can only yield the locus of a certain function, but not what processes are taking place. Communication among nerve cells is based on electrical and chemical signals. More specifically, transmitting information from one neuron to the next involves the release of chemical compounds, so called *neurotransmitters*. Furthermore, the concomitant energy requirement is reflected by the concentrations of related metabolites. A number of neurological dysfunctions are related to neurotransmission (e.g., Parkinson, Huntington) and metabolism (creatine deficiency). MR spectroscopy can provide neurochemical information from localized portions of the living brain and enables the non-invasive quantification of a variety of neurotransmitters and substances of the brain's energy metabolism [100, 101].

All experiments described in this thesis focus on MR spectroscopy in the visual cortex taking advantage of the elaborate knowledge that exists about this part of the brain. Moreover, our perception of the world is dominated by vision. Among all sensory modalities most of the cortical surface is devoted to vision.

## 3.2 The Visual Cortex: Function and Significance

The duty of the visual system is to provide coherent 3D percepts from 2D retinal patterns of stimulation. The visual cortex is located in the occipital lobe at the back of the brain. Based on criteria with respect to differences in cytoarchitecture, connectivity, topography, and functional characteristics about 40 areas have been defined in macaque visual cortex [102]. Information transmitted by the retinal ganglion cells is relayed in the thalamus to the primary visual cortex (V1) and subsequently projected to higher visual areas [103–105]. Earlier areas are retinotopically organized whereas higher visual areas are more dedicated to certain perceptual processes like objection recognition, color and motion processing. Hierarchical feedforward processing in visual cortex is probably oversimplified, e.g. there exist numerous parallel and feedback pathways.

The functional units of visual areas are subcolumnar functional aggregates, termed canonical microcircuits, whose operation shapes the local, modular properties of the area. A pronounced characteristic of these microcircuits is their weak feedforward input (e.g. thalamic input), strong excitation-recurrence and electrically inseparable excitation-inhibition events [106–108]. To understand how different functional properties, such as orientation, direction or color selectivity arise in these areas and how they are modified by learning or after nervous system injury an integrative approach is required that investigates both the electrical and the neurochemical processes.

### 3.3 Compounds in $^1\text{H}$ MR Spectroscopy of the Brain

Based on  $^1\text{H}$  MR spectroscopy measurements, changes of metabolite concentrations related to different type of sensory stimulation were reported for several substances including lactate [109–116], glucose [109,115,116], glutamate [115–117] and the conversion of phosphocreatine to creatine [118]. Such studies unambiguously provide important information on the brains neurochemistry and metabolism. Based on the limited spatial resolution they fail, however, to address questions regarding the organization of cortical microcircuitry, the principles of regional information processing, and the role of sensory versus modulatory inputs [119]. Animal-preparations are appropriate for such investigations as they can combine MR spectroscopy studies with other, invasive, neuroscientific techniques, that can examine electrical and chemical processes. The non-human primate model is ideally suited for the latter approach, as the sensory systems of the monkey are comparable in their organization to those of humans. In addition, the monkey sensory areas, here for instance the monkey visual system, offer considerable practical advantages for achieving the best possible resolution in MR spectroscopy experiments.

In general, a variety of metabolites contain nuclei that are detectable using MR techniques. If these substances are of biochemical relevance, new insights into the brain's physiology can be gained. MR spectroscopy of substances containing  $^{31}\text{P}$  enables the measurement of the energy metabolism in the brain,  $^{13}\text{C}$  labeling experiments provide tracking of metabolic pathways.  $^{23}\text{Na}$  and  $^{19}\text{F}$  are less often used. The most relevant nucleus for *in vivo* MR spectroscopy of the brain, however, is the  $^1\text{H}$  nucleus. This is because the gyromagnetic ratio is highest for all stable isotopes and therefore its sensitivity in MR experiments is higher than for all other nuclei. Since all organic compounds consist of hydrogen and the natural abundance of the  $^1\text{H}$  nucleus is almost 100% compared to other hydrogen isotopes, many brain metabolites are detectable *in vivo* with  $^1\text{H}$  MR spectroscopy [7].

In the following, the most prominent  $^1\text{H}$  metabolites in the *in vivo* brain are briefly summarized in alphabetic order of the main constituents. They are characterized with focus on their relevance for the brain's neurochemistry and with respect to their experimental accessibility with  $^1\text{H}$  MR spectroscopy. The chemical structures were taken from literature [21] and the details are reviewed in Appendix A. The exchangeable protons are indicated by asterisks and the assignments of the molecular groups follow the IUPAC nomenclature. For all metabolites the MR spectrum was calculated at 7 Tesla field and for a STEAM sequence with TE 10 ms and TM 10 ms based on the chemical shifts, J-couplings and number of nuclei as reported in [21]

(see section 5.7). An exponential line broadening of 5 Hz was applied and the spectra were normalized to the strongest spectral signal amplitude of the regarded substances. To this end, the phosphorylcholine (PCho) singlet at 3.22 ppm was used as a quantitative reference<sup>1</sup>. In other words, the signal amplitudes of all compounds are consistently scaled by this value and provide a direct comparison of the particular signal strengths for identical concentration values.

### 3.3.1 Alanine (Ala)

Alanine is a non-essential amino acid with a chemical structure similar to lactate for which the  $^3CH_3$  and the  $^2CH$  protons form a spectroscopic  $AX_3$  system<sup>2</sup> [21]. After being metabolized to pyruvate, it can enter the tricarboic acid (TCA) cycle [44].

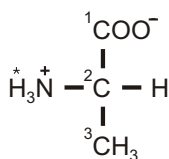


Figure 3.1: *Ala structure*

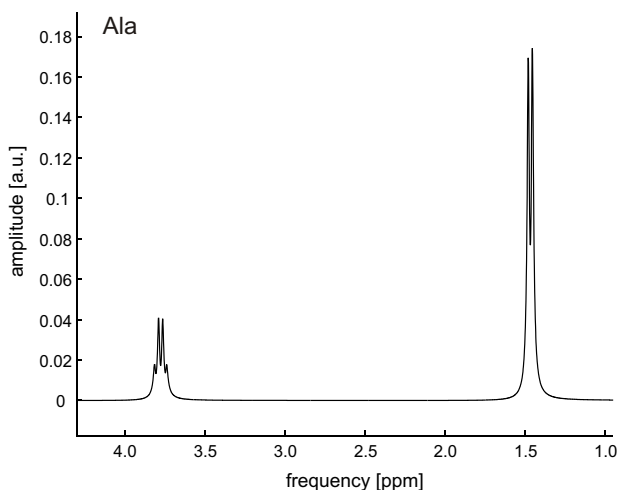


Figure 3.2: *Ala spectrum*

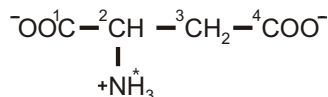
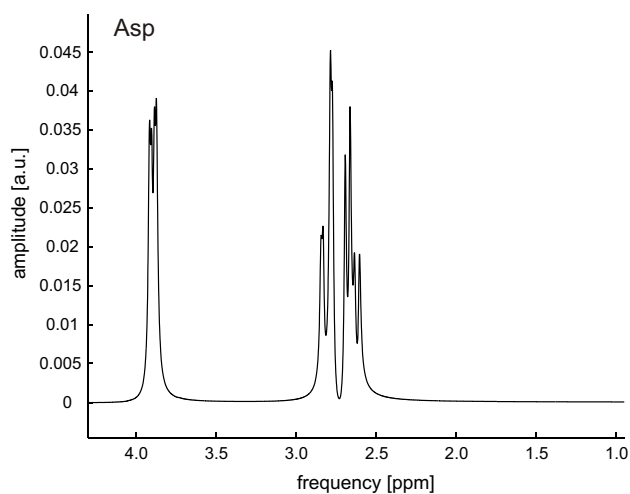
### 3.3.2 Aspartate (Asp)

Aspartate is a non-essential, dicarboxylic amino acid that is formed by transamination of the TCA cycle. It serves as a precursor for the synthesis e.g. of proteins and can promote energy production via its metabolism in the TCA cycle. The  $^3CH_2$  and the  $^2CH$  groups form a spectroscopic ABX system [21].

<sup>1</sup>Here and in the following, the ppm values assign chemical shifts  $\delta$

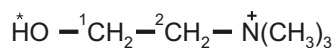
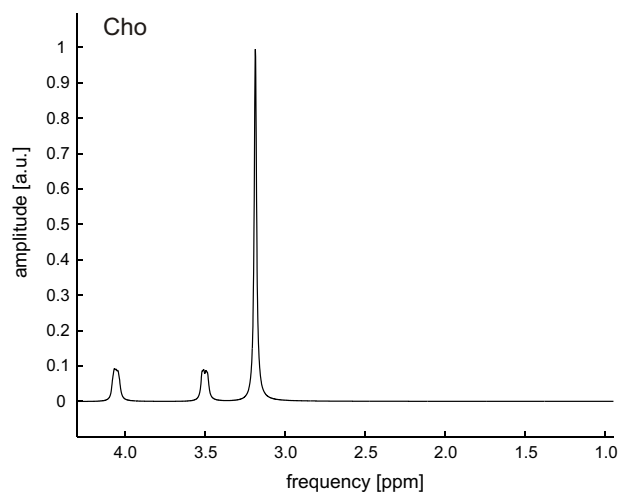
<sup>2</sup>In the chemical structures, superscript is used to enumerate the carbon atoms and the number of atoms is given in subscript

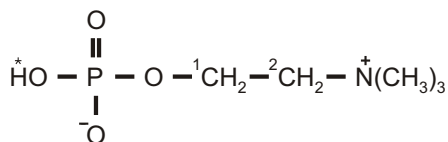
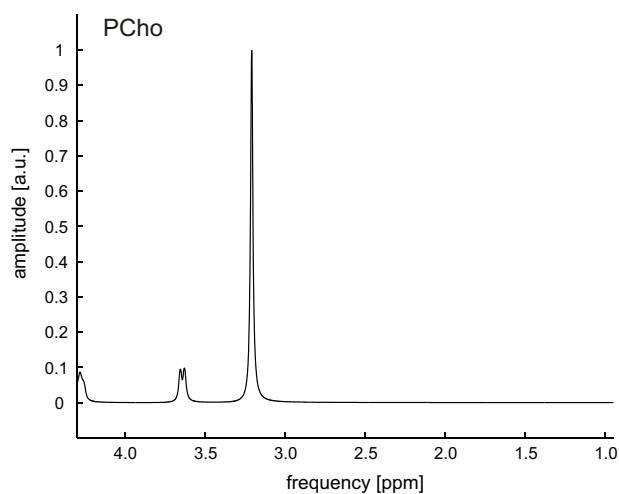
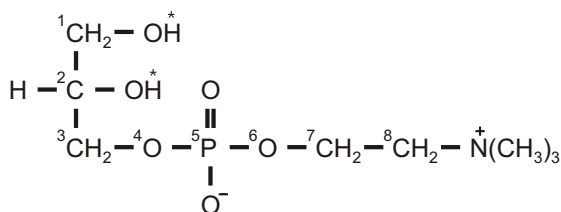
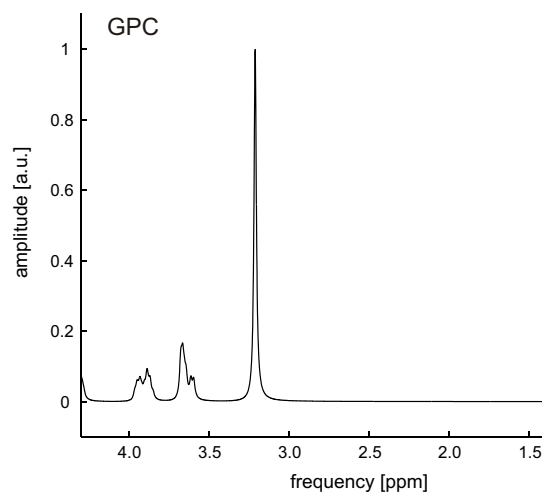


Figure 3.3: *Asp structure*Figure 3.4: *Asp spectrum*

### 3.3.3 Choline Containing Compounds (Cho, PCho, GPC)

Several choline containing compounds are uniformly distributed in the brain, i.e. choline (Cho), phosphorylcholine (or phosphocholine, PCho) and glycerophosphorylcholine (GPC).

Figure 3.5: *Cho structure*Figure 3.6: *Cho spectrum*

**Figure 3.7:** *PCho* structure**Figure 3.8:** *PCho* spectrum**Figure 3.9:** *GPC* structure**Figure 3.10:** *GPC* spectrum

They are involved in the synthesis and degradation of phospholipids which are essential for the normal cellular membrane composition [44]. Furthermore, choline is a precursor for acetylcholine which acts as a neuromodulator in the brain. The total choline concentration in the brain is 1–2 mM<sup>3</sup>, the contribution of choline itself, however, is far below 1 mM. The three methyl groups with their 9 magnetically equivalent protons lead to strong singlet resonances around 3.2 ppm for the different cholines. However, they can't be resolved under *in vivo* conditions.

<sup>3</sup>The unit mM (millimols) is commonly used in the field of MR spectroscopy as an abbreviation of the volume density millimols per liter

### 3.3.4 Creatine (Cr) and Phosphocreatine (PCr)

Creatine (Cr) is a non-protein amino acid, that is synthesized in kidney, liver and pancreas. The phosphorylation of creatine to the high energy substrate phosphocreatine (or creatine phosphate, PCr) via the enzyme creatine kinase provides an energy reservoir for keeping adenosine triphosphate (ATP) levels constant by the conversion of PCr back to Cr. In the brain Cr and PCr are present in neurons and glial cells [120].

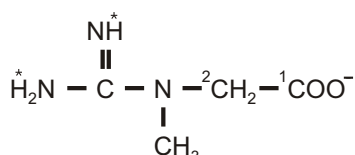


Figure 3.11: *Cr structure*

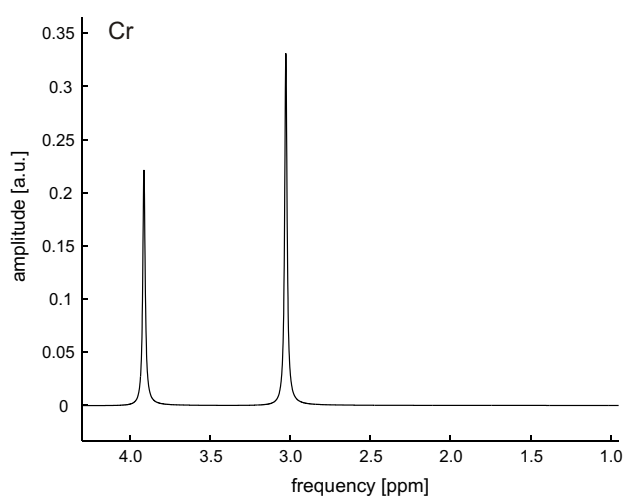


Figure 3.12: *Cr spectrum*

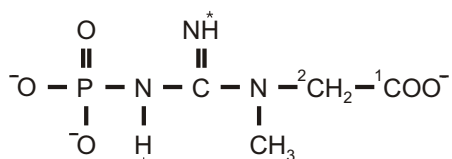


Figure 3.13: *PCr structure*

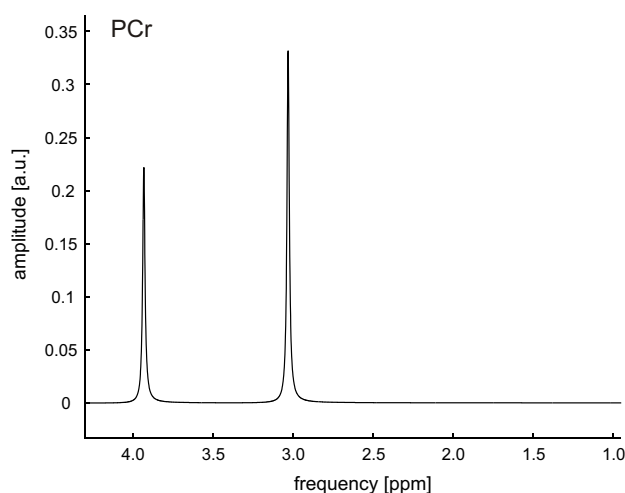


Figure 3.14: *PCr spectrum*

Furthermore, PCr is thought to be an phosphorus buffer and acting as an energy transporter that connects the energy production within mitochondria with the sites

of energy consumption [44]. Two prominent peaks are observed at 3.03 ppm and 3.93 ppm which can be attributed to the methyl and methylene protons of creatine and phosphocreatine [44].

### 3.3.5 $\gamma$ -Aminobutyric Acid (GABA)

$\gamma$ -aminobutyric acid (GABA) is an ionotropic and inhibitory neurotransmitter. It is thought to be built by decarboxylation of glutamate (and therefore effectively from glutamine), but additional synthesis pathways are assumed [121]. GABA is found in the brain and the spinal cord and acts on (at least) two different receptor types [121]. GABA has three methylene groups which can be considered as a spectroscopic  $A_2M_2X_2$  spin system and forms spectral multiplets centered at 1.89 ppm, 2.28 ppm and 3.01 ppm [21].

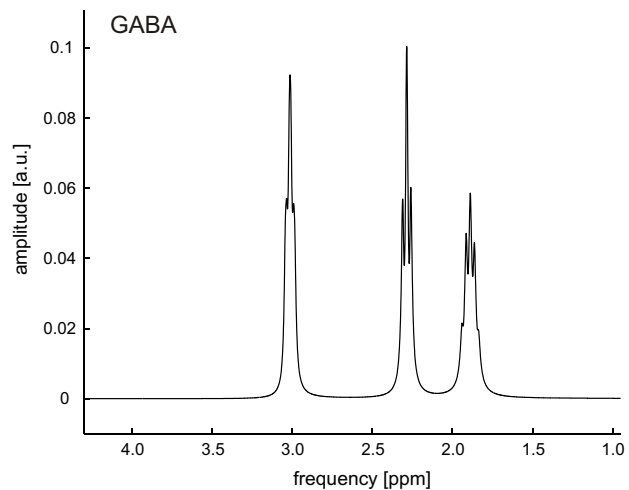
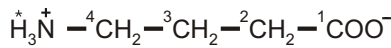


**Figure 3.15:** *GABA structure*

**Figure 3.16:** *GABA spectrum*

### 3.3.6 Glucose (Glc) and Lactate (Lac)

Glucose is the main substrate for the neuronal energy metabolism. Together with oxygen it is metabolized into water and carbon dioxide to replenish the cerebral ATP reservoirs by (anaerobic) glycolysis and in the (aerobic) TCA cycle [122, 123]. The triggering of glycolysis by glutamate has been proposed as a potential mechanism for the coupling of neuronal activity and energy metabolism [9]. Glucose is the precursor of neurotransmitters like GABA and glutamate and can be incorporated

into lipids, proteins, and glycogen [9]. For glucose two anomers exist at portions of 36% and 64% that lead to complex multiplet patterns.

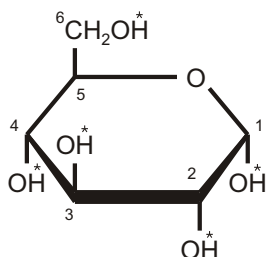


**Figure 3.17:** *Glc structure*

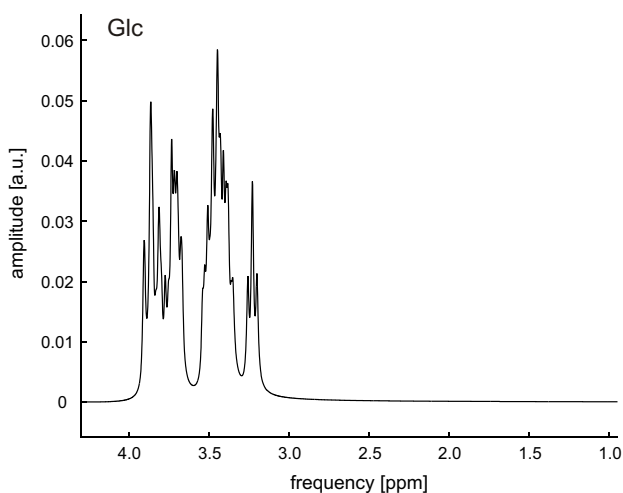


**Figure 3.18:** *Glc spectrum*

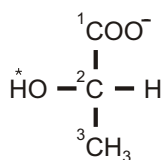


**Figure 3.19:** *Lac structure*

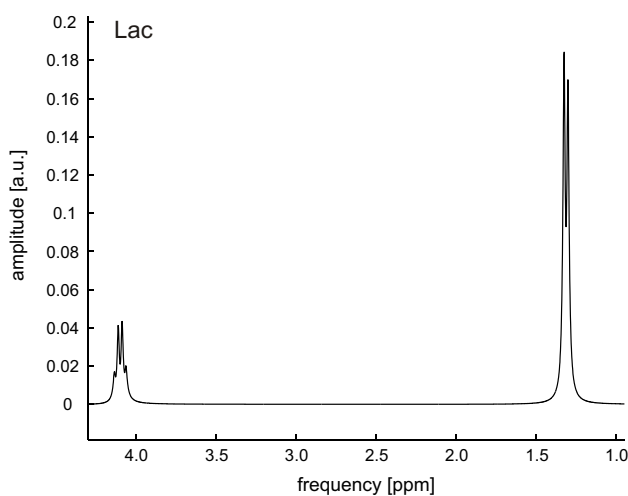


**Figure 3.20:** *Lac spectrum*

Lactate (Lac) is the product of the anaerobic glycolysis that is observed during physiological effort or under pathological conditions like ischemia or hypoxia [9,124]. Its role for the energy metabolism of the brain under aerobic conditions, however, is only poorly understood and a matter of current discussion [125–127]. Concentrations in the normally oxygenated brain are in the range of  $\sim 1.0$  mM. The methyl and methine groups of lactate form a spectroscopic  $A_3X$  spin system [21]. The detection of lactate with  $^1\text{H}$  MR spectroscopy methods is difficult due to potential influences

of the water suppression on the 4.11 ppm quartet signal and lipid signal from the skull bone which might interfere with the doubled signal at 1.33 ppm [44].

### 3.3.7 Glutamate (Glu)

Glutamate (Glu) is a low molecular weight, acidic amino acid, which is the most important excitatory neurotransmitter in the primate central nervous system [124]. The neurotransmitter is found in different types of brain cells, although the concentrations are highest in neurons. In addition, glutamate is part of the TCA and the urea cycle, and not exclusively found in the brain as being related to neuronal activity. Furthermore, it is physiologically linked to glutamine in the glutamate-glutamine cycle [128]. A partial invisibility of glutamate in  $^1\text{H}$  MR spectroscopy has been reported [44]. Glutamate has two methylene and one methine group that form an AMNPQ spin system [21]. Since the J-coupling constants of the glutamate protons are in the order of their chemical shifts, strong second order effects are observed and the spectral pattern becomes complex and strongly field dependent [21,129,130]. Glutamate concentrations in the brain are 9–12 mM [100,101], however, splitting into many low amplitude signals make it hard to detect.

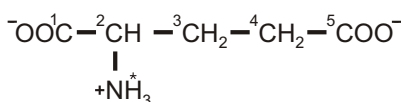


Figure 3.21: *Glu structure*

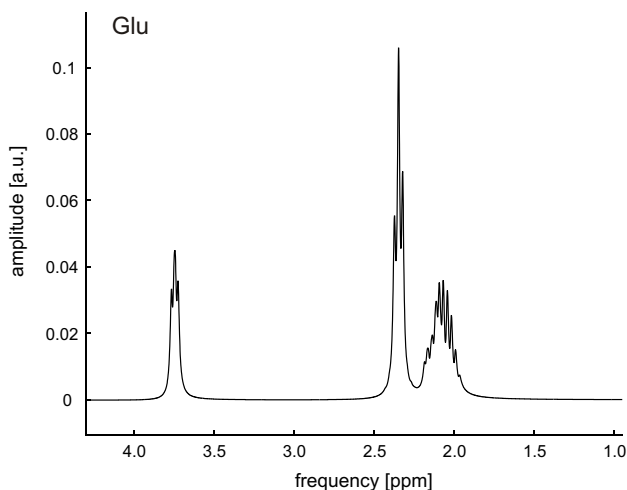
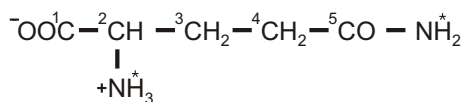


Figure 3.22: *Glu spectrum*

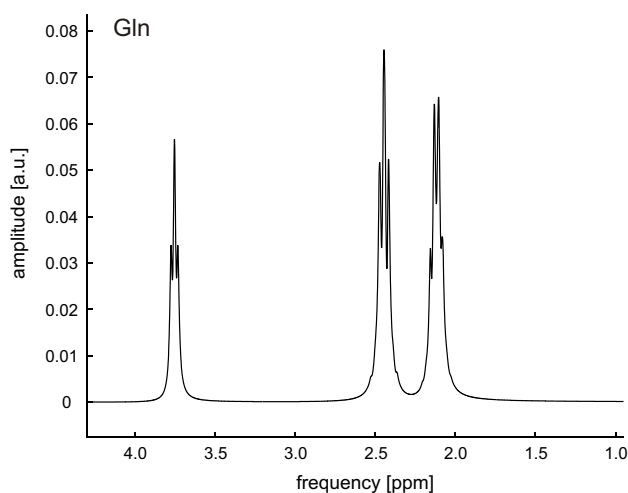
### 3.3.8 Glutamine (Gln)

Glutamine (Gln) is an inhibitory neurotransmitter built from glutamate by glutamine synthetase in the glutamate-glutamine cycle [124]. It is located in astrocytes

and plays an important role in ammonia detoxification, the regulation of glutamatergic neurotransmission and as a transport form of amino nitrogen [100]. Like glutamate, glutamine has two methylene and one methine group that lead to multiplet structures at 2.46 ppm and 3.75 ppm, respectively [21]. Due to the strong second order coupling effects, the MR spectroscopy pattern critically depends on the experimental parameters of magnetic field strength and MR sequence timing [130, 131].



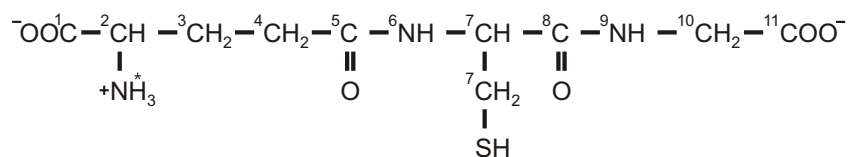
**Figure 3.23:** *Gln* structure



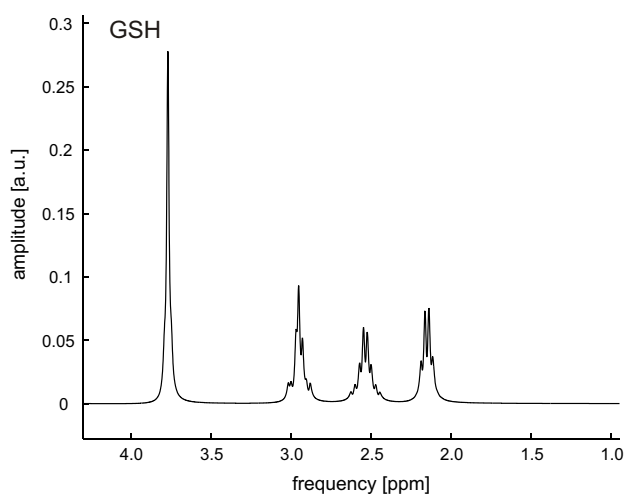
**Figure 3.24:** *Gln* spectrum

### 3.3.9 Glutathione (GSH)

Glutathione (GSH) is a non-essential tripeptide that can be synthesized from cysteine, glutamate or glycine. It is primarily located in astrocytes and is the major intracellular non-protein thiol acting as a buffer in order to maintain the intracellular redox state.



**Figure 3.25:** *GSH structure*

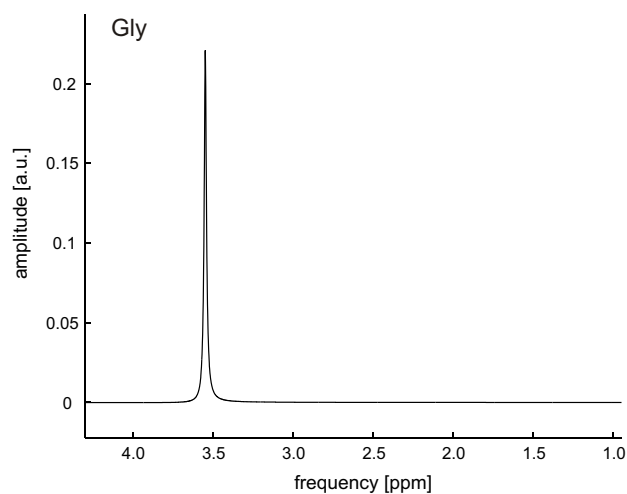
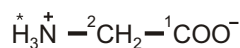


**Figure 3.26:** *GSH spectrum*

### 3.3.10 Glycine (Gly)

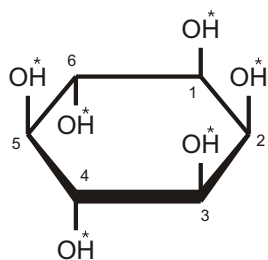
Glycine is a glucogenic protein amino acid that is of major importance for the synthesis of a variety of proteins, peptides, ATP, glutathione, creatine, glucose, and others. It has inhibitory properties in the spinal cord and is also apparent in the brain. The potential role as antioxidant is still under discussion. It contains two methylene protons that resonate at 3.55 ppm [21].



Figure 3.27: *Gly structure*Figure 3.28: *Gly spectrum*

### 3.3.11 Myo-Inositol (Ins) and Scyllo-Inositol (Scyllo)

*Myo*-inositol is a 6-carbon cyclic sugar alcohol with concentrations of  $\sim 5$  mM in the human brain. The exact function of inositol in general and its different derivatives is still poorly understood, however, inositol is considered a growth factor for mammalian cells. It is thought to be involved in the regulation of cell volume and might act as a storage form of glucose. The best known function of inositol is that it provides a precursor reservoir for second/third messenger substances and thereby links hormone-receptor binding with intracellular activity [100]. The detection and quantification of *myo*-inositol is hampered by the overlapping of the prominent *myo*-inositol resonance with the methylene protons of glycine at 3.55 ppm and the overlapping of the *myo*-inositol resonance at 3.27 ppm with choline and taurine. *Scyllo*-inositol, the second most abundant inositol isomer, can be observed since all protons resonate at the identical chemical shift of 3.35 ppm [44].



**Figure 3.29:** *Ins structure*

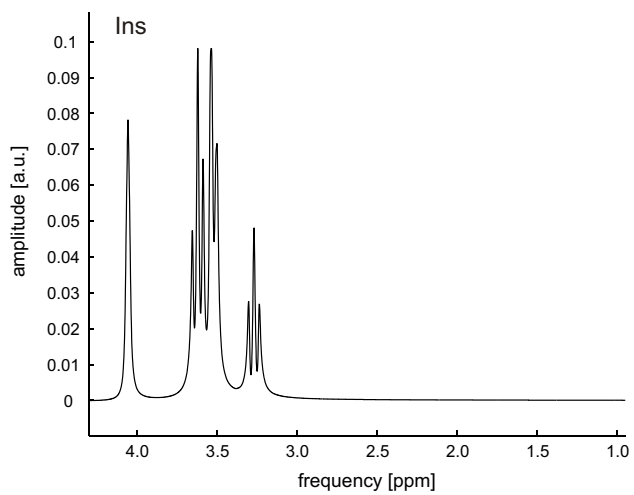


**Figure 3.30:** *Ins spectrum*

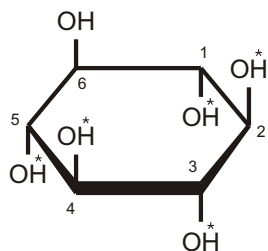


**Figure 3.31:** *Scyllo structure*

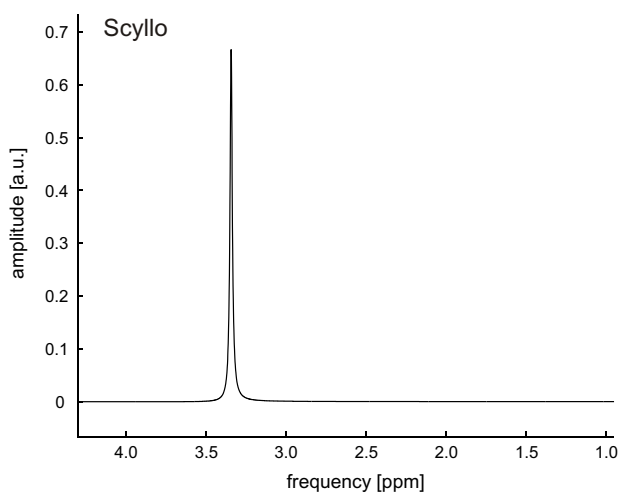


**Figure 3.32:** *Scyllo spectrum*

### 3.3.12 N-Acetylaspartate (NAA)

N-acetylaspartate (NAA) is an amino acid that is exclusively found in the central and peripheral nervous system. The concentrations in the brain are second highest (after glutamate) and depend on region, age, and health status [132]. Its exact physiological functions are still not clear [133], however, potential involvements as a storage for aspartate, a precursor for NAAG and osmotic functionalities are discussed. Due to its exclusive appearance in neurons and axons, and its absence from mature glia cells, NAA can be used as neuronal marker [134]. The higher neuronal density in gray brain matter is reflected by higher amounts of NAA ( $\sim 8\text{--}11$  mM) compared to white matter ( $\sim 6\text{--}9$  mM) [71, 135]. In pathologies with concomitant degeneration of neurons a decrease of NAA levels is observed [136, 137]. In  $^1\text{H}$  MR spectroscopy, the methyl group of NAA gives rise to the most prominent peak in *in vivo* brain spectra, located at 2.02 ppm.

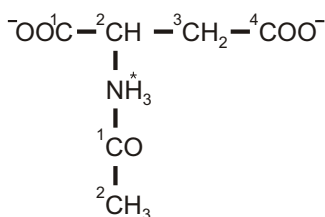


**Figure 3.33:** NAA structure

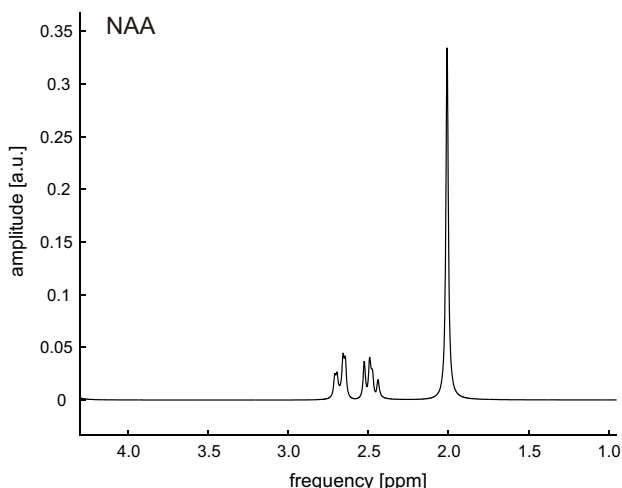


**Figure 3.34:** NAA spectrum

Since the frequency standard TMS can not be used in *in vivo*  $^1\text{H}$  MR spectroscopy, the singlet peak of NAA is commonly used as internal quantitative and frequency standard [44]. The position of the methyl peak of NAA remains relatively stable under physiological changes of temperature or pH. No modulations of the 2.02 ppm resonance are observed for varying echo times and NAA concentrations remain mainly unaffected under acute metabolic disturbances [135]. If NAA is used as quantitative standard, potentially overlapping signals of glutamate (2.04 ppm), GABA (1.91 ppm) or other metabolites with N-acetyl groups (like NAAG) have to be considered [44].

### 3.3.13 N-Acetylaspartylglutamate (NAAG)

N-Acetylaspartylglutamate (NAAG) is a dipeptide of N-substituted aspartate and glutamate with an heterogenous distribution in the brain. Potential functions for excitatory neurotransmission or a storage of glutamate are discussed.

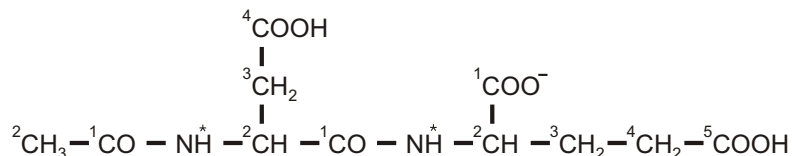


**Figure 3.35:** NAAG structure

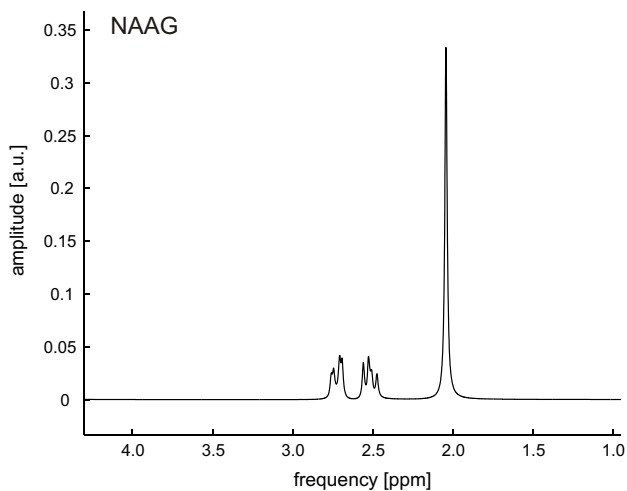


**Figure 3.36:** NAAG spectrum

### 3.3.14 Phosphorylethanolamine (PE)

Phosphorylethanolamine (PE) is a phospholipid that is formed from ethanolamine by phosphorylation using ATP. It is involved in the brain's lipid metabolism and anabolism of cell membranes.

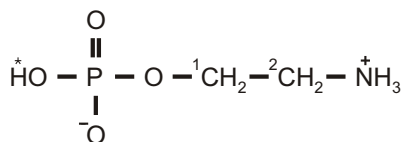


Figure 3.37: PE structure

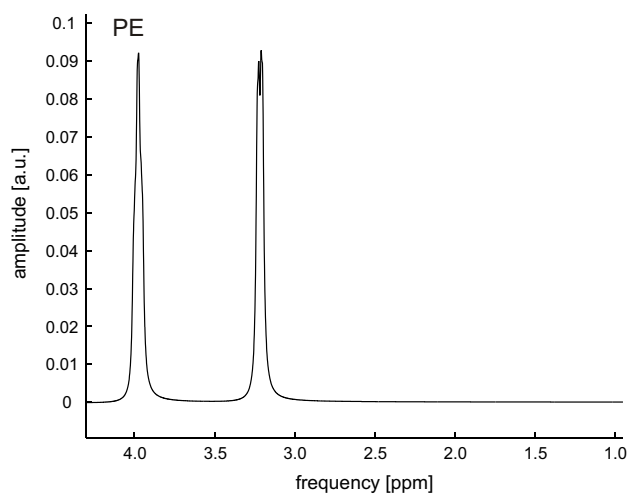


Figure 3.38: PE spectrum

### 3.3.15 Taurine (Tau)

Taurine is a non-protein amino acid that is synthesized in astrocytes. It has antioxidative properties and is needed for the osmoregulation of cells and the modulation of neurotransmitter activity [138]. The two adjacent methylene groups can be considered as an  $A_2X_2$  spin system [21]. The detection of taurine is demanding since the 3.27 ppm resonance can not be distinguished from the overlapping choline and inositol signals. In the brain taurine is found in all cell types.

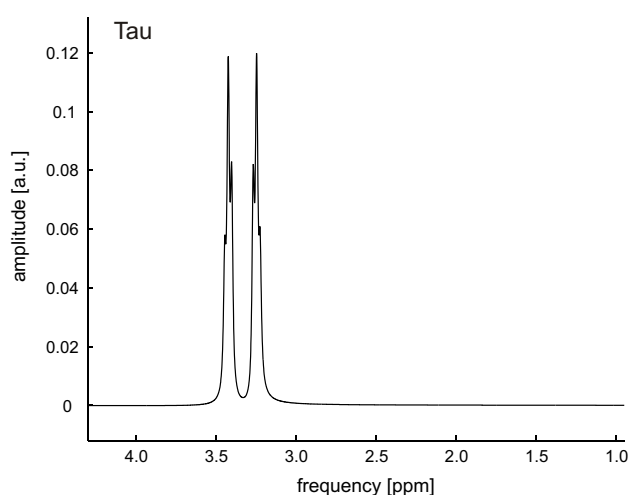
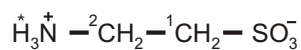


Figure 3.39: Tau structure

Figure 3.40: Tau spectrum

### 3.3.16 Macromolecules and Lipids

There are several lipid and fat compounds known to contribute to the  $^1\text{H}$  MR spectra of the brain as a macromolecule (MM) baseline that is underlying the signals of other brain metabolites. The macromolecule baseline has to be minimized by experimental minimization of spatial contaminations and has to be specifically considered for the quantification of the metabolic compounds. The characterization and quantification of the baseline is a main problem of *in vivo* MR spectroscopy, especially at short echo time [16–20].

## 3.4 Spectral Separation of $^1\text{H}$ Brain Metabolites

The goal of *in vivo*  $^1\text{H}$  MR spectroscopy of the brain is the detection of metabolite signals in order to achieve an independent quantification of the neurochemical substances. The strongest experimental limitation arises, however, by the inherently poor sensitivity of MR methods that are based on the Boltzmann spin polarization. According to equation (1.3), an increase of the static  $B_0$  field leads to increased spin polarization and therefore an improved sensitivity. The SNR of  $^1\text{H}$  MR spectroscopy may be increased more than linearly, if the susceptibility related line broadening at higher field is less than linear [139]. Strong magnetic fields are also advantageous to reduce second order coupling effects and to improve the spectral dispersion.

The studies of brain activity with MR spectroscopy methods focus on the quantification of neurotransmitters and substances related to the brain's energy metabolism, since these are directly or indirectly linked to functional activity. The problem therefore no longer is the separation of single peaks or multiplet structures from the same compound but the distinction of different potentially overlapping compounds as will be discussed in the next two sections.

### 3.4.1 Glutamate vs. Glutamine

Based on the central role of glutamate and glutamine for neurotransmission and brain metabolism, their independent quantification is of primary interest. The spectral separation of glutamate and glutamine *in vivo* is possible using  $^1\text{H}$  MR spectroscopy techniques, but the highest spectral quality is required [140]. The  $^2\text{CH}$  and the  $^3\text{CH}_2$  groups of glutamate and glutamine resonate at  $\sim 3.75$  ppm and  $\sim 2.10$  ppm, respectively, and a separation based on these structures is not possible under *in vivo* conditions. The  $^4\text{CH}_2$ -groups, however, lead to complex multiplet

structures at 2.35 ppm for glutamate and at 2.45 ppm for glutamine. Figure 3.41 shows simulated spectra of glutamate (dotted line) and glutamine (dashed line) at a physiological concentration ratio of 3:1. In practice, the summation spectrum of both metabolite signals would be measured (solid line). The simulations were done for different magnetic field strengths of 1.5 T, 4.0 T and 7.0 T, at *in vivo* achievable line widths at those fields similar to [141]. At high magnetic fields, the

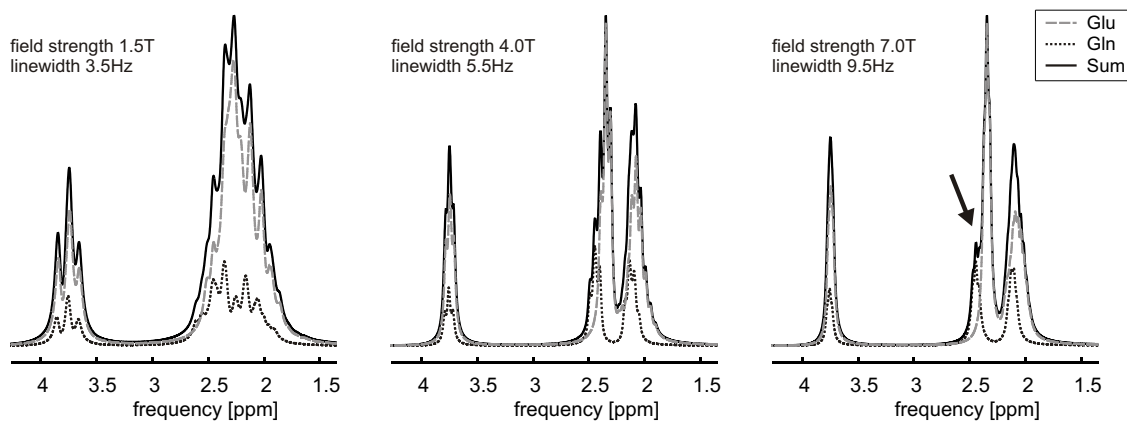


**Figure 3.41:** *Glutamate/glutamine separation.* Glutamate (dashed gray) and glutamine (dotted black) spectra at a physiological concentration ratio of 3:1 are shown for three different field strengths and *in vivo* achievable line widths. For high field and good shim, the metabolites can be disentangled from the summation spectrum (solid black) at the 2.45/2.35 ppm position (assigned by an arrow).

details of the multiplet structures are lost due to the concomitant broadening of the spectral lines *in vivo*. The increased absolute frequency shift of the  $^4\text{CH}_2$ -signals relative to each other, however, enables the spectral separation of glutamate and glutamine [141,142]. The benefit of better SNR and simplified spectra at high fields can only be exploited if optimal shimming is achieved, as field distortions due to susceptibility effects also increase with field strength [142].

### 3.4.2 Creatine vs. Phosphocreatine

Creatine and Phosphocreatine are a second set of substances of particular interest in neurochemistry based on their central role for the brain's energy metabolism. The separation of these compounds with  $^1\text{H}$  MR spectroscopy is even more challenging, since both substances show strongly overlapping singlet peaks only. The  $N(\text{CH}_3)$ -groups of creatine and phosphocreatine resonate both at 3.03 ppm and the chemical shift difference of the  $^2\text{CH}_2$ -signals at 3.91 ppm for creatine and 3.93 ppm for phosphocreatine is very small. For a Larmor frequency of 300 MHz at 7 Tesla,

the absolute frequency spacing is as small as 6 Hz. Simulations of equal concentrations of creatine and phosphocreatine [143] at *in vivo* achievable line width are shown in figure 3.42 (with a presentation similar to figure 3.41 or [141]). In this figure, however, the frequency axis is scaled to provide the same absolute frequency spacing per unit axis length. In other words, doubling the field strength results in double length of the frequency axis.

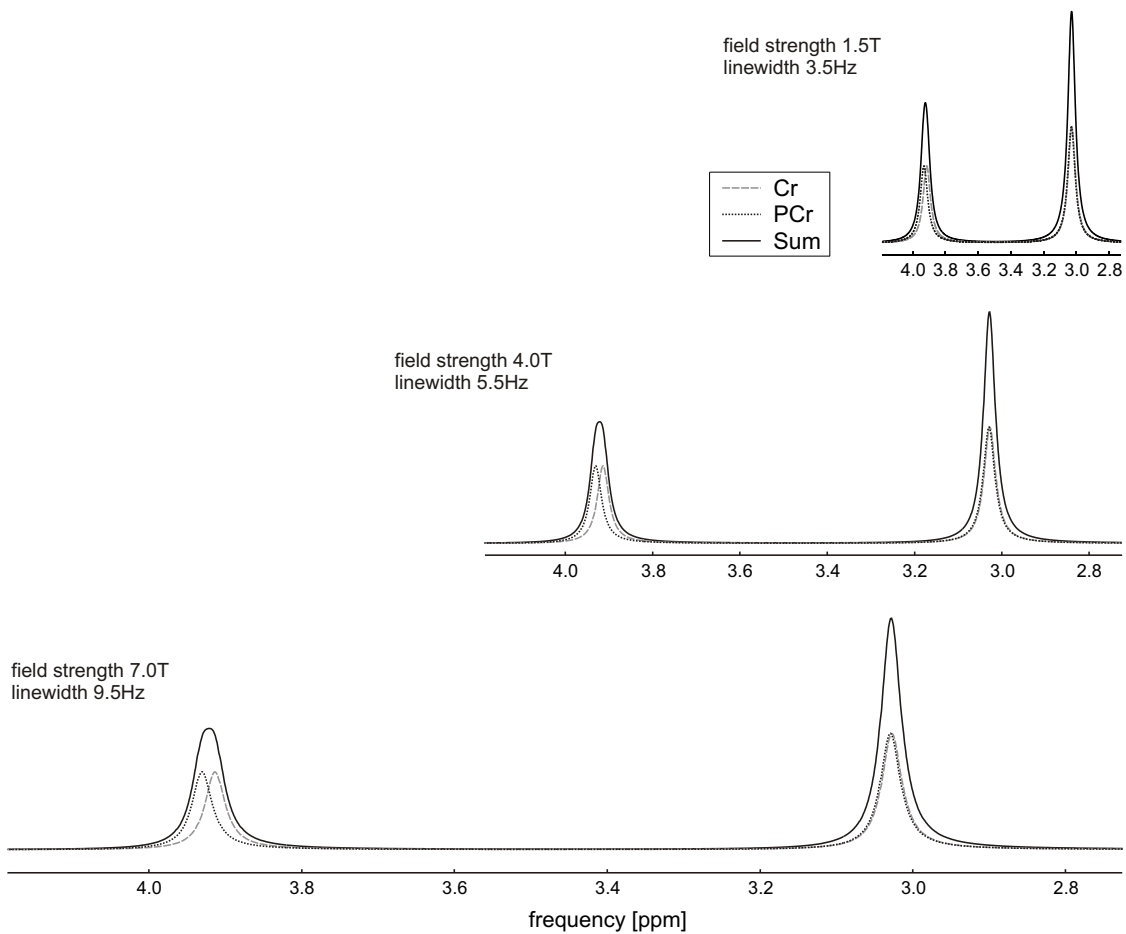


**Figure 3.42:** *Creatine/phosphocreatine separation. An improved separation of Cr (dashed gray) and PCr (dotted black) at higher field is only achieved under excellent shimming conditions, when the increased absolute frequency shift is larger than the susceptibility induced line broadening effect.*



Since the creatine and phosphocreatine protons are not J-coupled, the appearance of the spectra remains unchanged with increasing field strength. An improved separability of peaks therefore can only be achieved, if the broadening of the peak linewidths can be kept smaller than the improved separation based on the absolute frequency splitting. At 9.4 T and 11.7 T, splitting of creatine and phosphocreatine has been achieved in the rat that led to a dip between the peaks [8, 118, 144]. At 7 T in the primate this is not to be expected in the near future under *in vivo* conditions. However, under optimal shimming conditions the peak separation can be improved compared to MR spectroscopy at lower field strengths (Fig. 3.43). Statistical methods have to be used for a deconvolution of the spectral peaks and the quantification of the metabolites (see section 2.6).

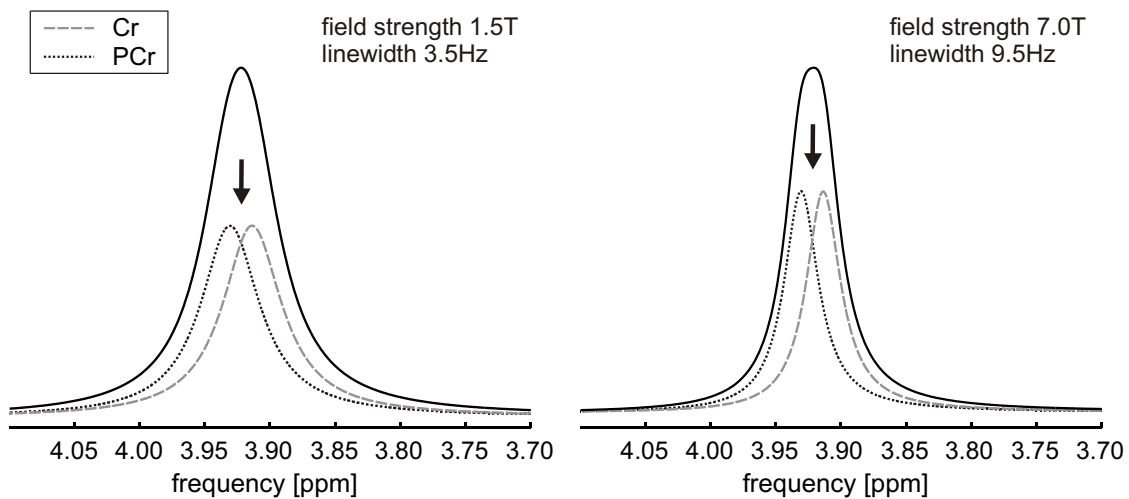


**Figure 3.43:** Creatine/phosphocreatine separation of the  $^2\text{CH}_2$  signals. At 7 Tesla (300 MHz) the chemical shift difference of 0.02 ppm for the Cr (3.91 ppm) versus the PCr (3.93 ppm) singlets corresponds to 6 Hz. Excellent shimming is required to effectively gain from the high field strength and to achieve an improved separation of the peaks.

# Chapter 4

## Experimental Setup

### 4.1 7 Tesla Magnet

All measurements described in this thesis were performed with a vertical 7 T/60 cm Bruker Biospec system (Bruker BioSpin, Ettlingen/Germany) dedicated to MR imaging and spectroscopy in the monkey [145, 146].

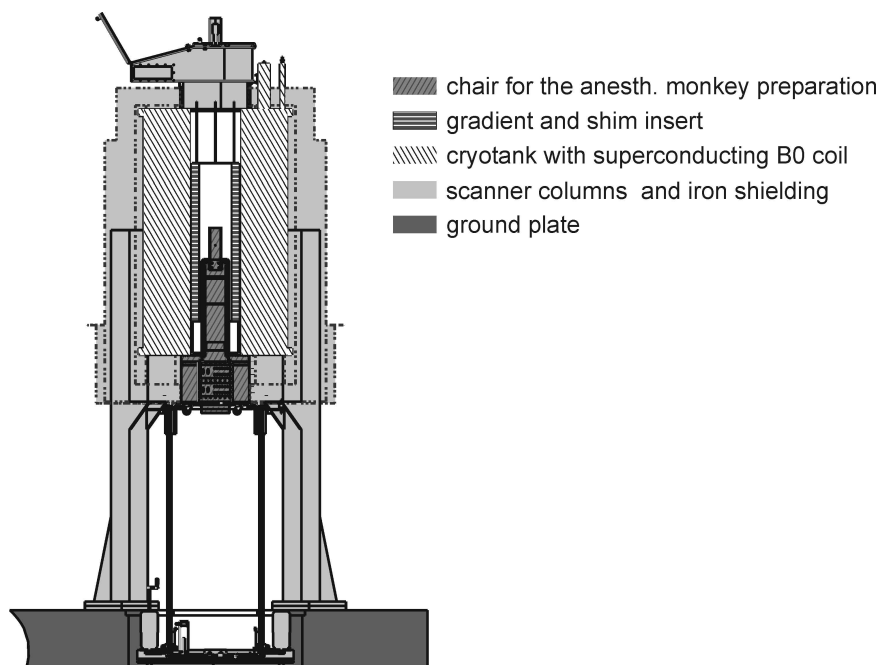


**Figure 4.1:** Vertical Bruker BioSpec 7 Tesla/60 cm Scanner for MR experiments with awake or anesthetized macaque monkeys. The chair with the monkey is placed below the vertical magnet and lifted up to position the monkey's head to the iso-center of the magnet.

## 4.2 Magnetic Field Gradients

The system was originally equipped with a Bruker gradient and shim insert BGA38 (maximum strength 80 mT/m, rise time  $<200 \mu\text{s}$ , Bruker BioSpin, Ettlingen/Germany). Since the gradient and shim insert broke multiple times, it has been substituted by a Siemens insert AC44 (40 mT/m,  $<200 \mu\text{s}$ , Siemens Medical Solutions, Erlangen/Germany) designed for 3 Tesla *Allegra* MR scanners for the investigation of human heads.

## 4.3 Radio-Frequency System

A custom-made saddle coil (300 MHz) built in collaboration with Dr. Hellmut Merkle (NIH, Bethesda/USA) was used for spin excitation [146]. Signal acquisition for spectroscopy was done with an actively-decoupled 35-mm RF surface coil (Bruker BioSpin, Ettlingen/Germany). For large scale field mapping solely the saddle coil was used for spin excitation and signal reception.

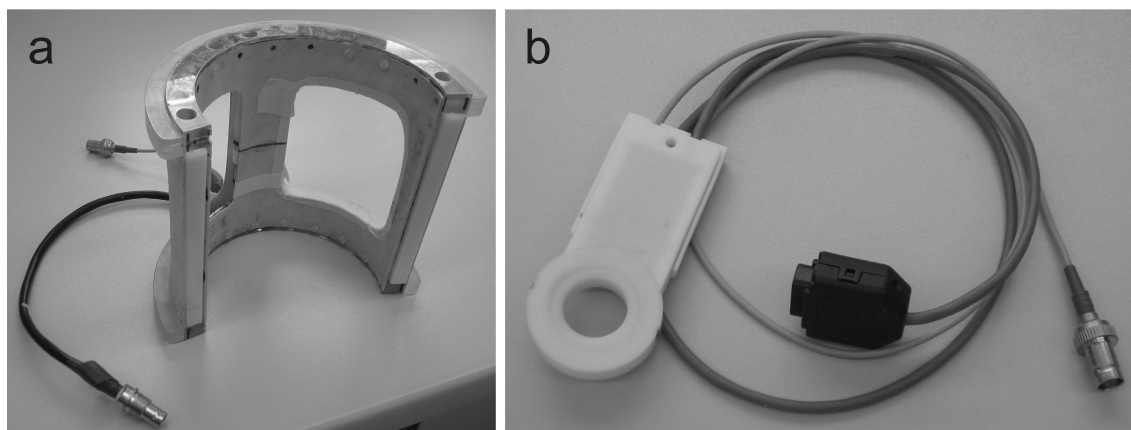


**Figure 4.2:** Radio-frequency (RF) coils for MR imaging and spectroscopy. A home-built saddle coil was used for VAPOR, OVS and STEAM excitation (a) before the spectroscopy signals were received with a surface RF coil with a diameter of 35 mm (b). For large scale field mapping the saddle coil alone was used.

## 4.4 Anesthetized Monkey Setup

For the *in vivo* measurements adult macaque monkeys (*macaca mulatta*, 6–9 kg) were used in an anesthetized preparation. All procedures and experiments were approved by the local authorities (Regierungspräsidium) and were in full compliance with the guidelines of the European Community (EUVD 86/609/EEC) for the care and use of laboratory animals.

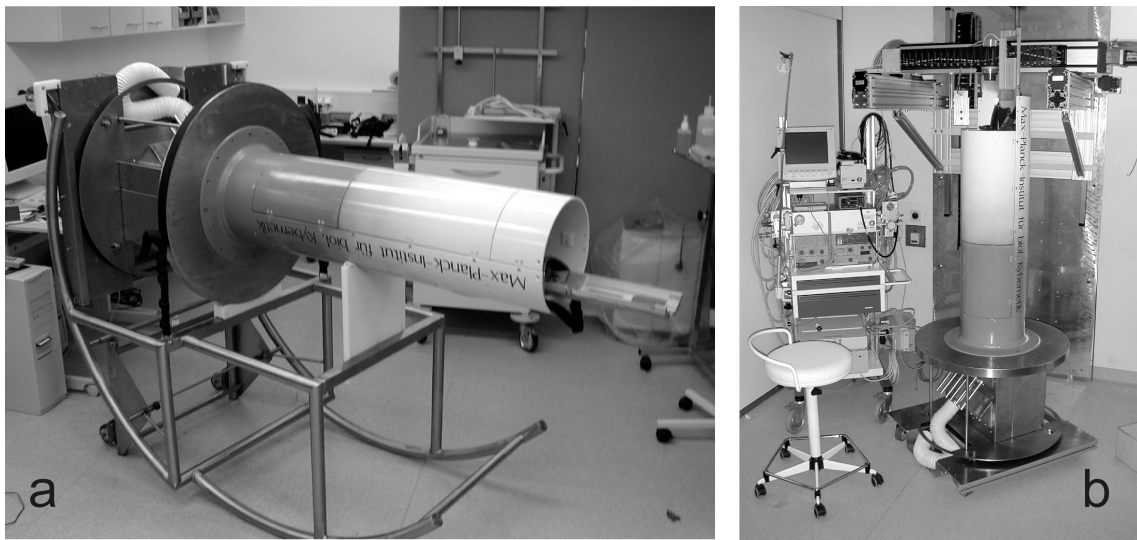


**Figure 4.3:** *Experimental monkey setup: chair and anesthesia machine. (a) Firstly, the monkey was anesthetized on the horizontally positioned chair. Then, the swing mechanism was used to lift up the chair to an upright position (b, right). During the entire experiment the monkey’s physiology and vital functions were controlled by the anesthesia machine (b, left) and recorded for later analysis.*

Surgical procedures, anesthesia, and details of the animal setup were described previously [147]. Head fixation was achieved with a one-point head post made of non-magnetic plastics (*peek*) and the anesthesia ensured a stable positioning of body and head with only respiration related motion remaining [146].

Oblique geometry handling with respect to the laboratory coordinate system for imaging, shimming and spectroscopy was avoided by a 30 to 45 degree rotation of the monkey's head. The saddle coil was placed to the back of the monkey head and the surface coil was positioned over the visual cortex of one hemisphere. Due to the rotation of the monkey head relative to the magnet's main axis, the surface coil was effectively placed coplanar to the magnets x-z-plane and optimally placed to perform MR experiments of the visual cortex which was the target region in all examinations.

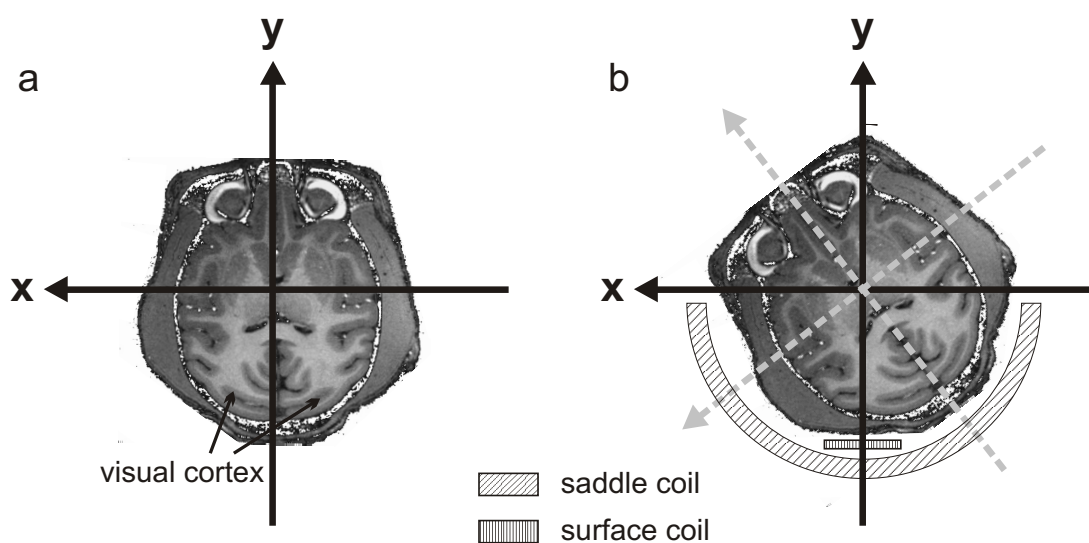


**Figure 4.4:** *Head and RF coil positioning. For a straight head positioning the visual cortex was rotated 30 to 45 degrees with respect to the scanner's coordinate system (a). Therefore, the monkey head was rotated to align the (primary) visual cortex with the scanner's coronal x-z-plane (b). Consequently, there was no need for oblique geometry handling in any of the imaging, shimming or spectroscopy applications. A saddle coil (half circle) was used for spin excitation and a surface coil (bar) placed over the visual cortex of one hemisphere for signal reception.*

# Chapter 5

## Implementation and Quality Management

### 5.1 Implementation and Optimization of MR Spectroscopy and CSI Methods

#### 5.1.1 Pulse Sequence for MR Spectroscopy and CSI

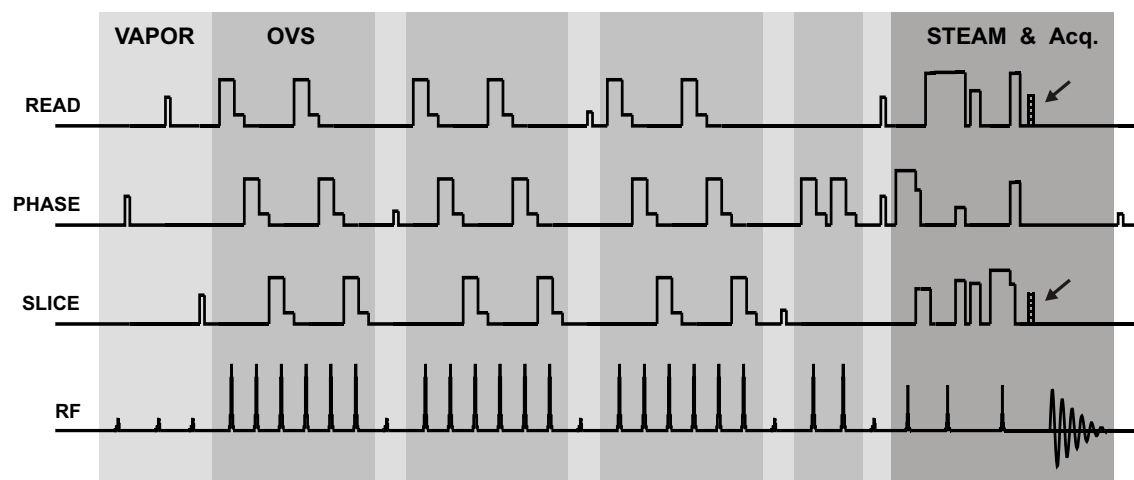


**Figure 5.1:** Scheme of the MR spectroscopy sequence: interleaved outer volume suppression (OVS) and water suppression (VAPOR) is followed by a single voxel excitation with STEAM and the acquisition (Acq.) of the second half of the stimulated echo. A phase encoding (arrows) can be added to allow for chemical shift imaging. (time axis from left to right; gradients: READ, PHASE, SLICE; radio-frequency: RF)

A STEAM sequence was implemented for MR spectroscopy and extended by conventional and acquisition weighted phase encoding to enable chemical shift imaging (CSI) (Fig. 5.1). The accuracy of the spatial excitation profile was achieved by three sinc shaped RF pulses with 5 side lobes that had been filtered by a cosine function. The excitation profile of the pulses is shown in figure 5.2a as the direct Fourier transform of the time domain profile of the RF pulse and compared to the full Bloch simulation for a set of realistic parameters used for single voxel MR spectroscopy in the primary visual cortex (V1) of the macaque (compare chapter 9).

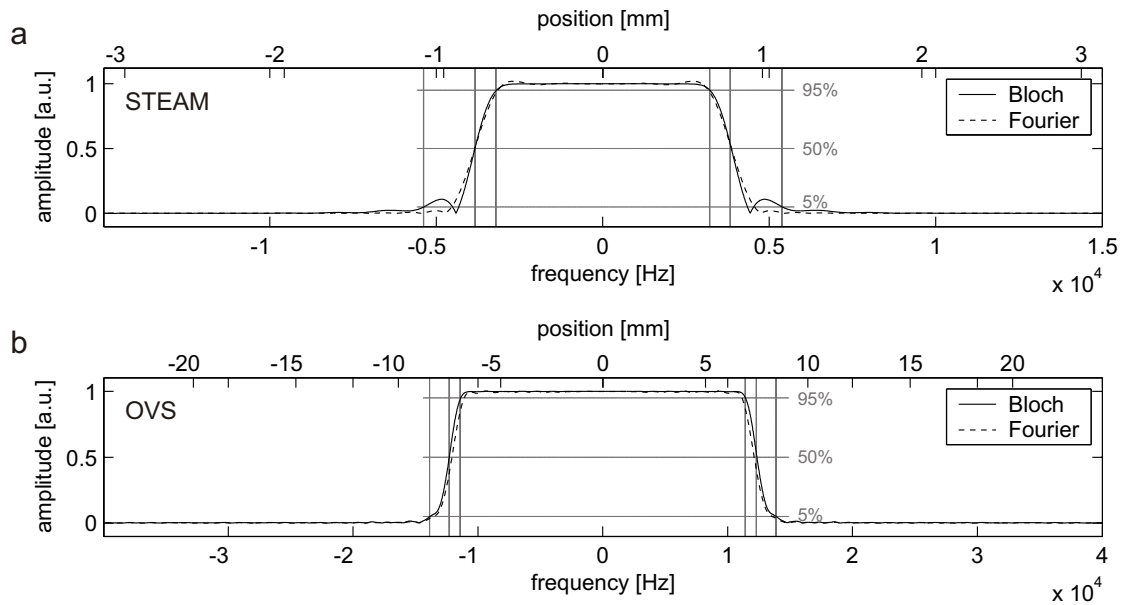


**Figure 5.2:** Analysis of frequency/excitation profiles of the RF pulses used for STEAM localization and outer volume suppression (OVS). (a) The direct Fourier transform (dashed) of the 5 lobe sinc RF pulse for STEAM excitation is compared to the result of Bloch simulations (solid). (b) Analysis of the excitation profile of an adiabatic hyperbolic secant pulse used for OVS.

Even if the Fourier transform of the RF pulse, i.e. the linear small angle approximation, rapidly decays to zero outside the assigned frequency band, the full Bloch simulation shows considerable side bands. To suppress these side bands in the spectroscopy sequence, 4 outer volume suppression (OVS) modules with 20 adiabatic hyperbolic secant pulses were implemented and applied prior to the STEAM localization (Fig. 5.1). The spatial profiles of the full 3D STEAM and OVS modules were then experimentally tested using a 1D imaging readout projection of the water signal (Fig. 5.3/5.4). No influence on the localized STEAM signals were observed when the gap size between the OVS module and the STEAM voxel was chosen to 0.5–1.0 mm, but the side lobes of the STEAM profile were strongly reduced.

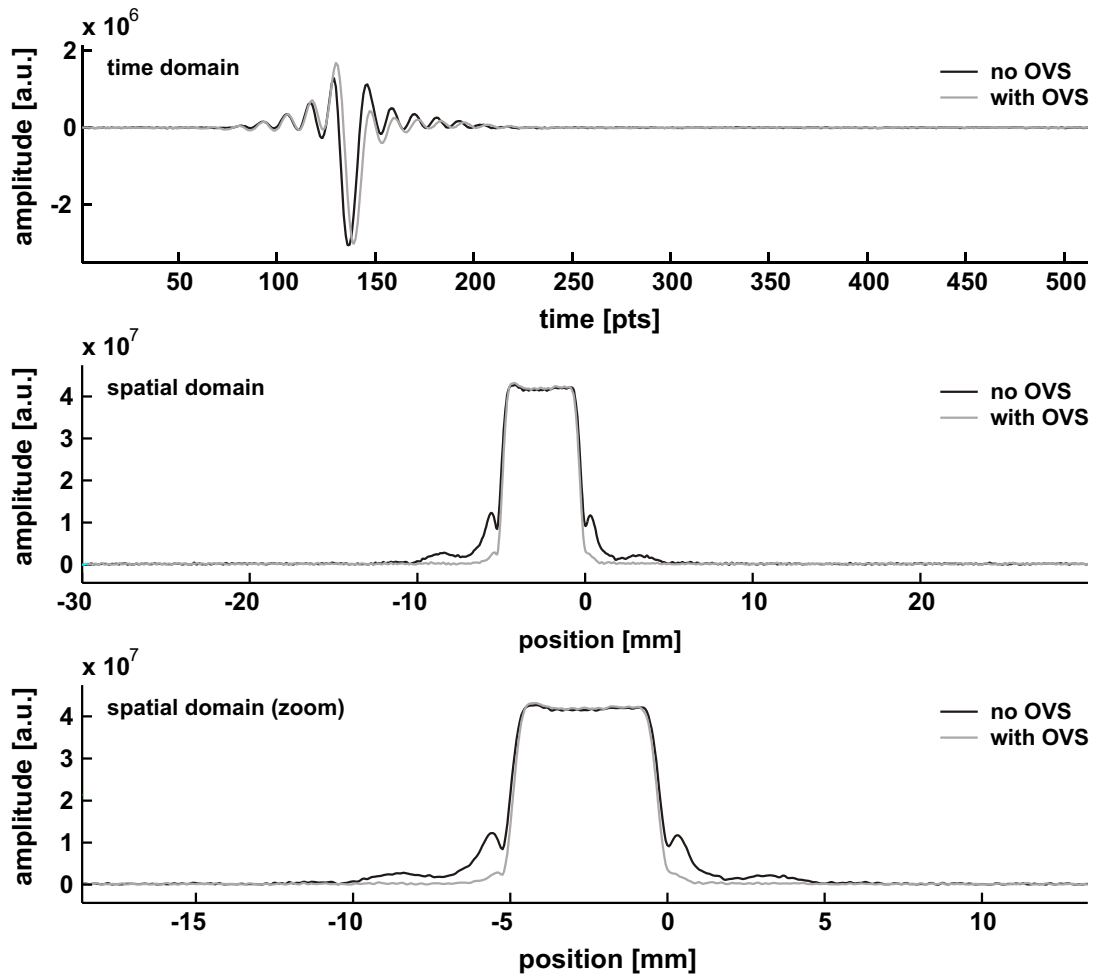


**Figure 5.3:** STEAM excitation profile w/o outer volume suppression (OVS). Without OVS, the 5 mm STEAM profile showed considerable side bands (black line). With OVS the sidebands were strongly reduced, however, the STEAM profile remained unaffected (gray line).



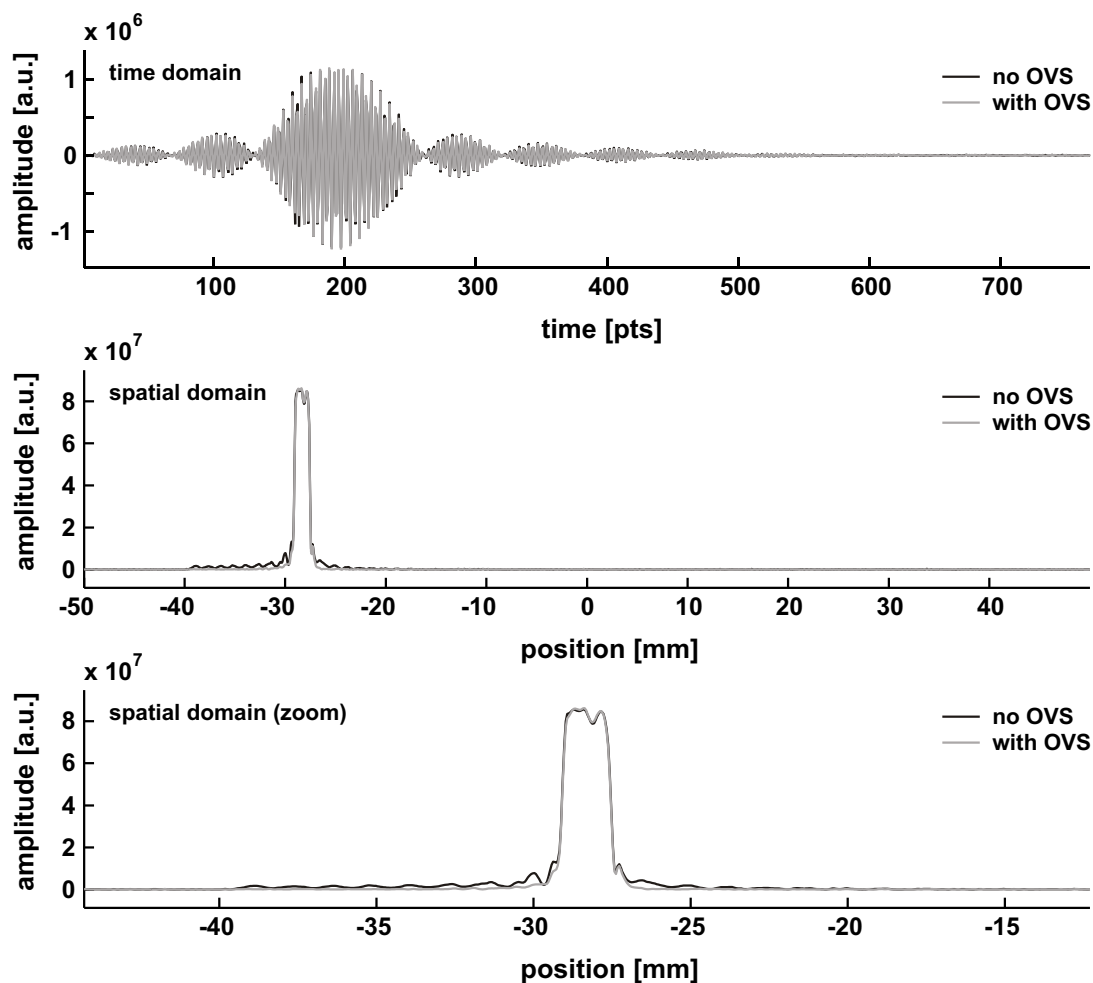


**Figure 5.4:** *STEAM* excitation profile w/o OVS for very small voxels. Even for a voxel with a thickness of only 1.6 mm and gaps between the *STEAM* voxel and the OVS slices of 0.5-1.0 mm the signal strength of the *STEAM* voxel was not affected, but the side bands were strongly reduced.

Water suppression was achieved by asymmetric, numerically optimized RF pulses with VAPOR [8], consisting of 7 CHESS modules with inter-delays of 150–100–100–90–90–55–25 ms. The suppression module was adjusted to remove more than 99% of the signal within a frequency band of 150 Hz (95% at 190 Hz) and less than 1% outside the frequency bandwidth of 315 Hz (5% at 275 Hz), which was experimentally validated on a well-shimmed water phantom by shifting the synthesizer frequency similar to [8] (Fig. 5.5). Thereby, good water suppression was achieved, but relevant metabolite signals at 4.1 ppm and below remained unaffected.

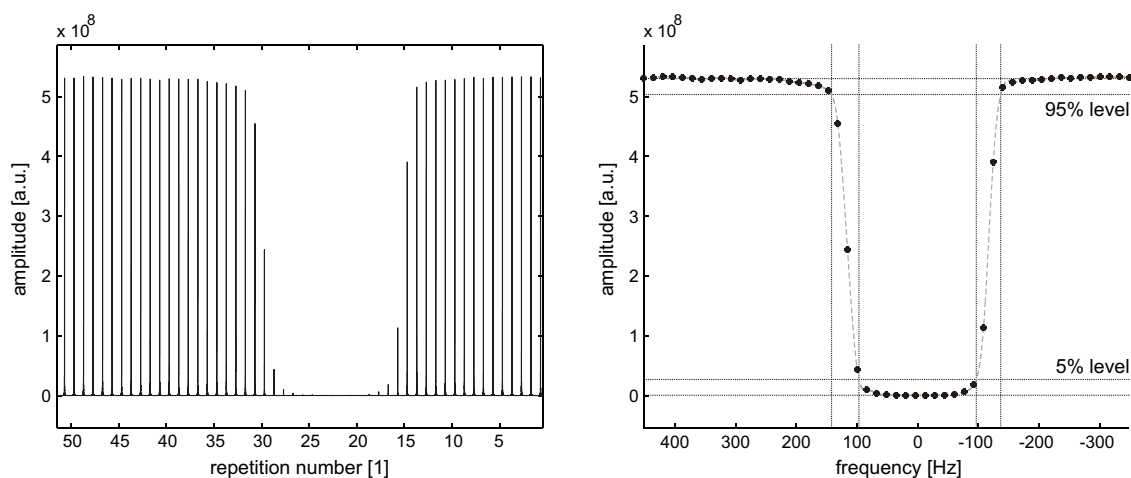


**Figure 5.5:** *Experimental verification of the VAPOR frequency profile. A series of water scans with shifted synthesizer frequency (left) provided the frequency band for which the water signal was suppressed more than 95% or less than 5% (right).*

### 5.1.2 Single Voxel MR Spectroscopy

The quality of the MR spectroscopy sequence was tested *in vitro* on a phantom that contained water and three tubes of water solution where glutamate and NAA have been added at different concentrations. The results of a single voxel  $^1\text{H}$  MR spectroscopy experiment (VOI  $10 \times 10 \times 10 \text{ mm}^3$ , TE 10 ms, TM 10 ms, repetition time TR 2 s, number of average NA 512) from a phantom compartment with 50 mM NAA and 40 mM glutamate is shown in figure 5.6.

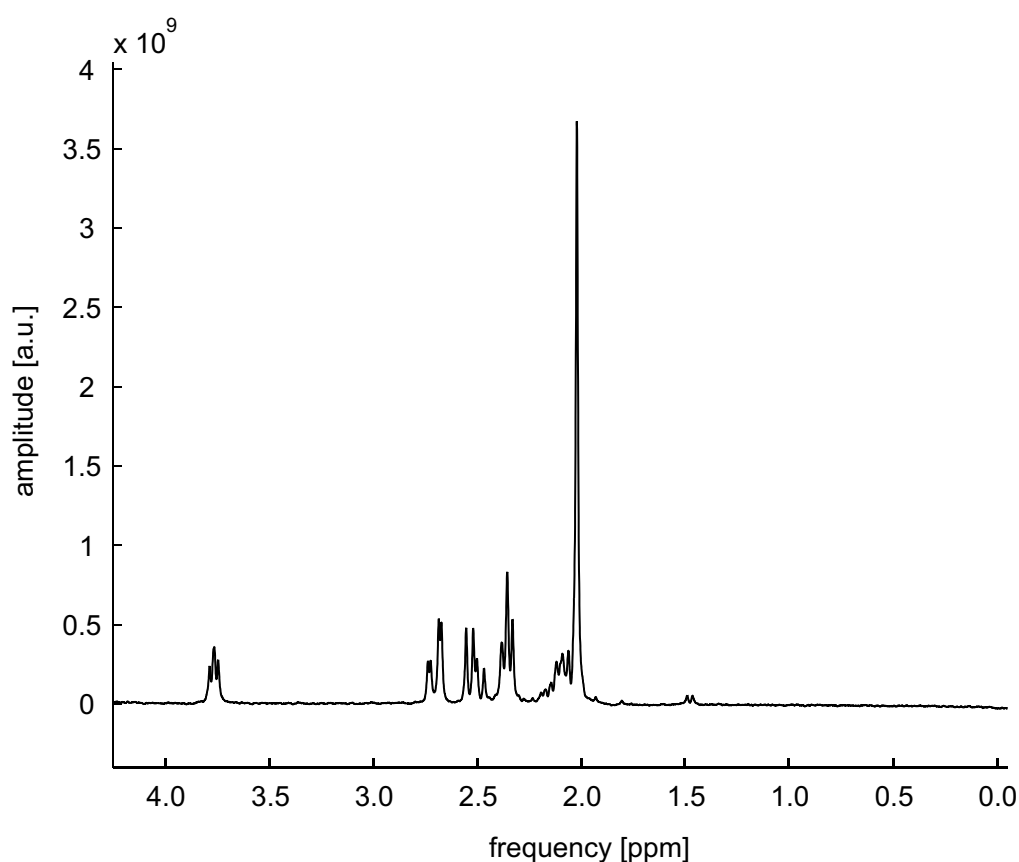


**Figure 5.6:**  $^1\text{H}$  MR spectrum at 7 Tesla (300 MHz) from a metabolite phantom of 50 mM NAA and 40 mM glutamate. No first order phasing was required and the baseline was flat.

Based on the very good shim (FWHM of 2.2 Hz for the NAA singlet at 2.02 ppm), an exponential line broadening of 1.5 Hz was applied before the Fourier analysis to avoid ripple artifacts. The spectrum was eddy current corrected and zero-order phased, however, first-order phasing was not necessary and the baseline was flat outside the metabolite regions without correction.

The same MR sequence then was applied in the macaque monkey brain *in vivo* with VOI  $5 \times 5 \times 5 \text{ mm}^3$ , TE 10 ms, TM 10 ms, TR 4 s, NA 1024 (Fig. 5.7). Again, no first order phasing nor baseline correction was required and the overall excellent appearance of spectrum proved the quality of the MR sequence and its adjustment. The water line width of the MR spectroscopy voxel was 10.5 Hz and the creatine + phosphocreatine (Cr + PCr) singlet at 3.03 ppm had a FWHM of 9.0 Hz. For comparison: the principal lower line width limit for  $^1\text{H}$  MR spectroscopy at 7 T of the awake human brain was estimated to 9.5 Hz for the same creatine peak [141].

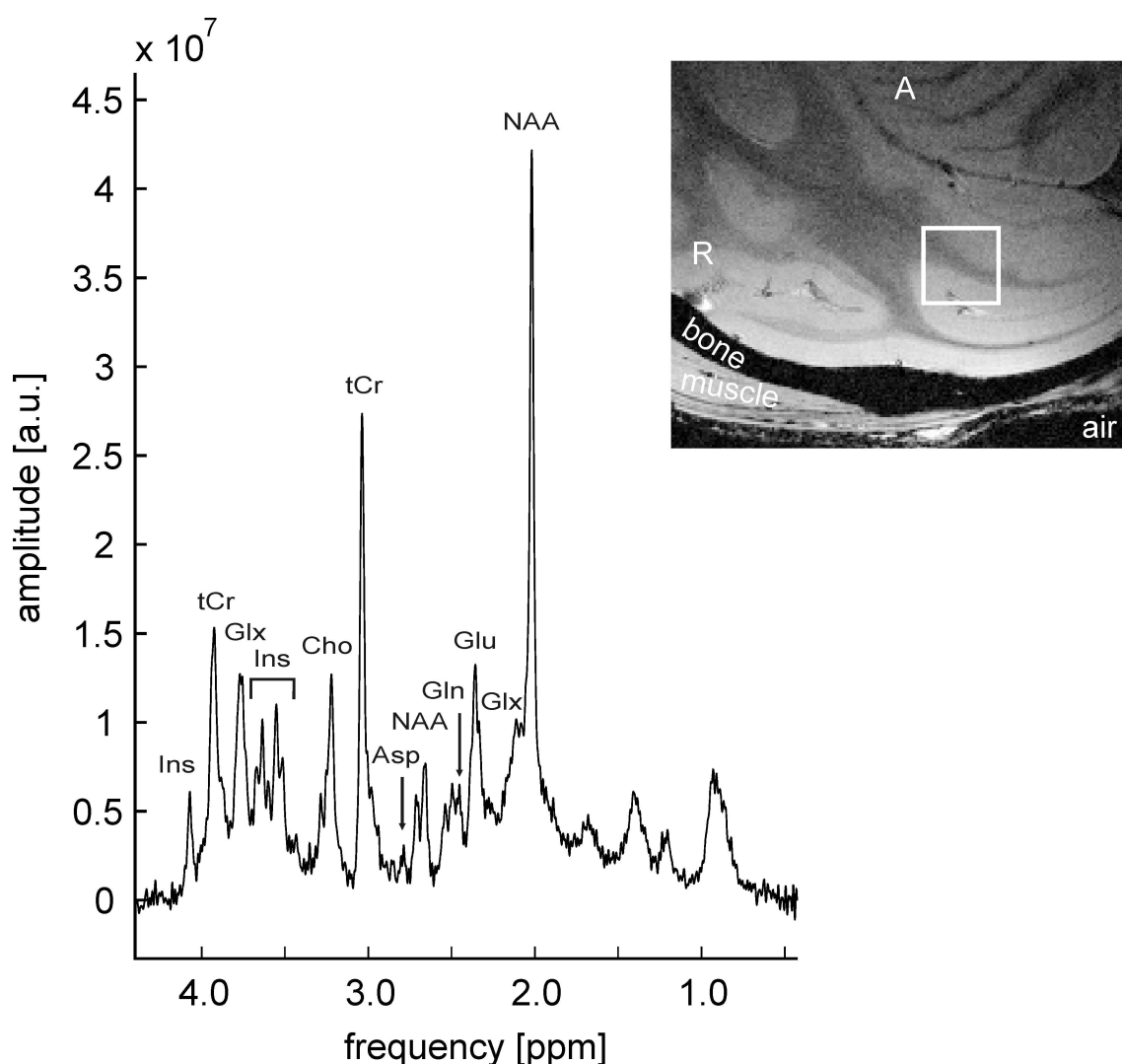


**Figure 5.7:**  $^1\text{H}$  MR spectrum from the monkey visual cortex at 7 Tesla (300 MHz). No first order phasing was required and the spectral baseline was flat. A line width of 9 Hz (FWHM of the Cr + PCr singlet at 3.03 ppm) and good SNR enabled the spectral deconvolution of more than 10 metabolites at  $\text{CRLB} < 20\%$  for a  $5 \times 5 \times 5 \text{ mm}^3$  volume (white box). (A: anterior, R: right)

### 5.1.3 MR Spectroscopic Imaging

The MR chemical shift imaging sequence was tested on the same metabolite phantom and optimized protocols were generated for different geometries. Figure 5.8 shows a spectroscopy matrix (left) and a gray scale map that was achieved by integrating the water signals at 4.7 ppm. Here, the STEAM localization was restricted to a  $5 \times 5 \times 5 \text{ mm}^3$  cube voxel centered to the  $25 \times 2 \times 25 \text{ mm}^3$  coronal CSI FOV (TE 10 ms, TM 10 ms, TR 3 s, NA 1). The  $13 \times 13$  phase encoding matrix was spatially zero-filled to  $39 \times 39$  before the spatio-spectral Fourier transformation. The STEAM localization as well as the functionality of the spatial CSI encoding can be seen.

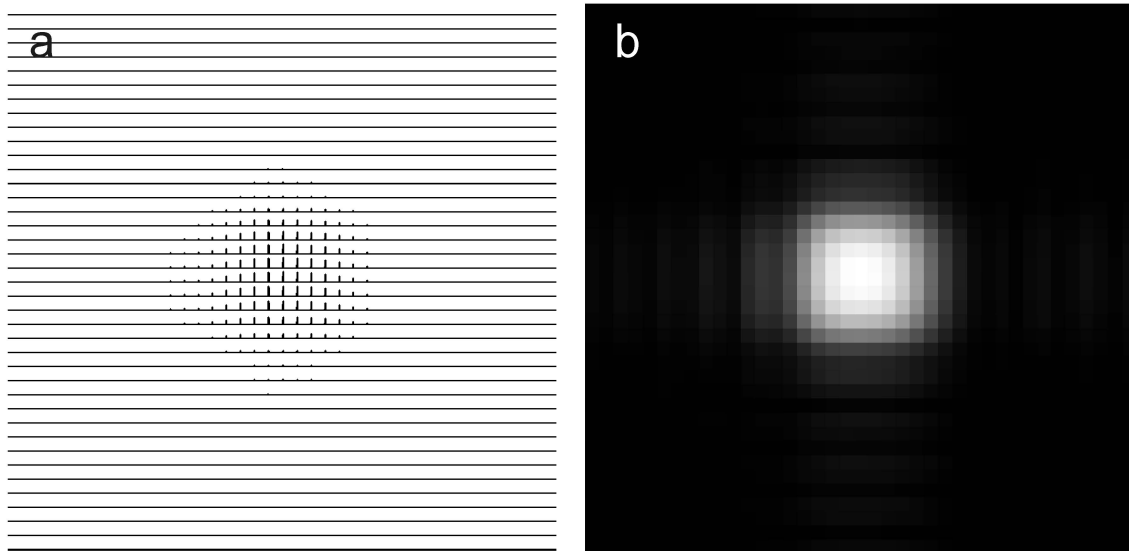


**Figure 5.8:** MR chemical shift imaging matrix (left) and spectral integration map of the water signals (right) from a  $5 \times 5 \times 5 \text{ mm}^3$  STEAM voxel centered to the coronal  $25 \times 2 \times 25 \text{ mm}^3$  CSI FOV in a water phantom.

The functionality of the CSI method for the spatial localization of brain metabolites was tested by applying the MR sequence for mapping the NAA content within a vertically positioned circular tube of the metabolite phantom (Fig. 5.9a, black circle, imaging: FLASH, FOV  $90 \times 125 \text{ mm}^2$ , matrix  $512 \times 512$ , zoom on CSI FOV). The NAA compartment, thereby, was to be distinguish from the surrounding water area via differing metabolite concentrations. Here, the STEAM and the CSI FOV's were selected equally to  $40 \times 40 \times 3 \text{ mm}^3$  with TE 10 ms, TM 10 ms, TR 3 s, and a CSI matrix of  $21 \times 21$  phase encoding steps. For post-processing a spatial smoothing with a 2D Gaussian filter function with a sigma of 3, spatial zero-filling to  $35 \times 35$ , 5 Hz exponential line broadening, eddy current correction, spectral zero-filling of

2 k complex data points to 4 k were applied before the 3D spatio-spectral Fourier transformation. The (magnitude) spectral matrix is shown in figure 5.9b for the frequency range of  $-0.5$  to  $3.6$  ppm. The position of the metabolite signals fitted the tube position and no significant signals, e.g. tails of the water resonance, were observed in any of the spectra demonstrating good shim and water suppression. The encoding of the spectral integration values of the NAA singlet peak at  $2.02$  ppm into gray scale values led to a bright circular spot at position of the NAA tube, but the surrounding phantom and air compartments remained dark, i.e. no NAA was detected.

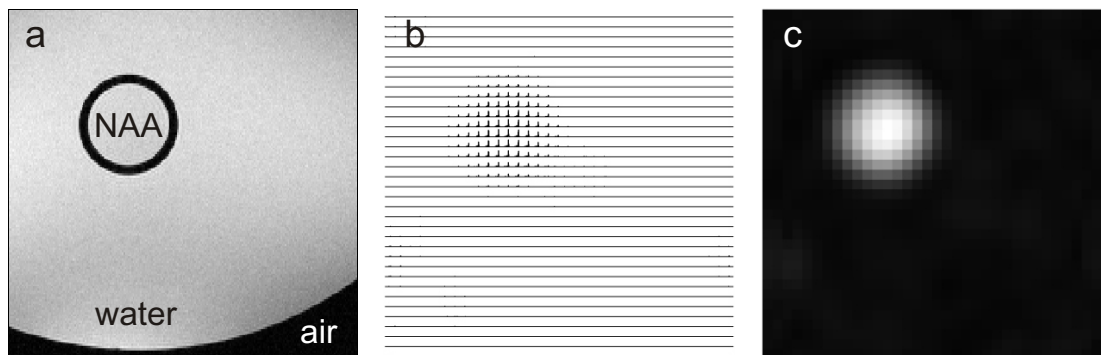


**Figure 5.9:** *MR spectroscopic imaging of a metabolite phantom. (a) Axial slice section through a vertically positioned metabolite tube (black circle). The compartment outside the tube contained only water, inside 50 mM NAA were added. (b) Spectral matrix. (c) Integration map of the NAA singlet peak at 2.02 ppm.*

## 5.2 Performance and Quality Measures

The stability of the MR system and the summation properties of scans with respect to the attainable SNR (as defined in Ref. [148]) were measured on a phantom via the water resonance and the metabolite resonances of total creatine (Cr + PCr) at 3.03 ppm and N-acetylaspartate (NAA) at 2.02 ppm. Correlation coefficients  $>0.99$  were achieved for all fits of the SNR against the square root of the average number. The SNR, however, increased by 11% (as determined from slope fitting), when an additional preamplifier (Advanced Receiver Research, Burlington/USA) was attached between the RF coil and the receive channel of the MR scanner, which demonstrated that the observed noise was not exclusively subject- and receive coil-related.

Sensitivity and spectral quality in MR spectroscopy critically relies on scanner performance, and specifically on signal/frequency stability and minimal noise injection. To check for potential problems of the receive channel or external noise injections, signals at zero RF power and zero gradients, i.e. noise signals, were acquired before starting the experiment, and using the actual MR spectroscopy sequence. The data were Fourier transformed without further processing and four different metrics were used to evaluate them: 1) The ratio of the global mean and standard deviation was considered a measure for a global DC offset; 2) the ratio of the global maximum value and the global standard deviation as a measure for single outliers. 3) The spectral data were binned into 20 frequency windows of 250 Hz and local and global baseline fluctuations were measured by the standard deviation of the window means divided by the global standard deviation. 4) Fluctuations of the relative amplitude power of particular frequency bands were determined from the ratios of the standard deviation of the particular windows and the global standard deviation of the entire data set. The calculation of the standard deviation of the vector of window ratios then provided a single scalar measure. In all cases, the smaller the measure values, the better the receive channel properties. The experimental acquisition and the subsequent analysis required less than 1 minute.

The determined values for the normalized ratio of means and the standard deviations of the noise analysis were  $<0.03$  in phantom experiments and  $<0.05$  under *in vivo* conditions in all cases. The maximum noise amplitudes divided by the global standard deviation were found to be in the range of 3.3–4.0 *in vitro* and 3.3–4.1 *in vivo*. Values for the window-based standard deviations of the means and the standard deviations of the frequency bands were 0.07–0.11, in the phantom and 0.05–0.08 in the monkey, respectively. Notably, no additional noise injection was observed due to the anesthesia machine and the electronic supervision of the monkeys vi-

tal functions. This was tested in a phantom study with the full anesthesia setup attached and *in vivo* in the monkey. The performance of the STEAM acquisition including the performances of the magnetic field gradients, the RF amplifier and the receive channel were controlled from a series of MR spectroscopy scans without water suppression prior to the acquisition of metabolite spectra. The phase stability of the STEAM excitation was analyzed in the time domain on the first point of the acquisition signal. For the analysis of Larmor frequencies and peak amplitudes, an exponential line broadening and spectral zero-filling were applied before the Fourier transformation to the frequency domain. A spline interpolation further increased the point resolution of the water peak. The magnitude amplitude and the frequency of the maximum position were determined and the mean values as well as their standard deviations were calculated. Linear fitting of the frequency values provided the system drift as a function of time and was used to remove major linear drifts before the standard variation was calculated. Thus, the measure was independent of the acquisition duration and was focused on the frequency spread rather than on major drifts. A Fourier analysis of the time domain phases, and the frequency domain peak amplitudes/positions was applied to check for periodic distortions. Depending on the number of repetitions and the repetition time the data acquisition and analysis took 3–6 minutes.

The phase variation of the time domain signal was  $(1.0 \pm 0.9)$  degrees (mean  $\pm$  std) in phantom experiments, increasing to  $(4.3 \pm 2.3)$  degrees *in vivo*. The frequency variation of the water peaks after linear detrending was determined to be  $(0.03 \pm 0.01)$  Hz in the phantom, and  $(0.56 \pm 0.36)$  Hz *in vivo*. Variations of the maximum amplitudes of the magnitude spectra were larger in the monkey  $(0.93 \pm 0.58)\%$  (mean  $\pm$  std.) compared to phantom studies  $(0.22 \pm 0.16)\%$ .

### 5.3 Frequency Lock Algorithm

The system's MR frequency (including hardware and subject) was observed to be changing over time (see section 5.4). To quantify the major frequency drifts and to correct for them, a frequency lock algorithm was implemented similar to those used in analytical chemistry. By a regular determination of the water Larmor frequency for the particular MR spectroscopy voxel, the synthesizer and the receiver frequency were readjusted and the major long term frequency drifts were eliminated during the experiment. Thereby, the spectral line width was minimized and stable localization and suppression modules throughout the entire acquisition period were guaranteed.



## 5.4 MR Frequency Stability

No dominant peaks were observed in the Fourier analysis of the time and frequency domain amplitudes, phases and frequencies of serially acquired water spectra in phantoms (Fig. 5.10a,b).

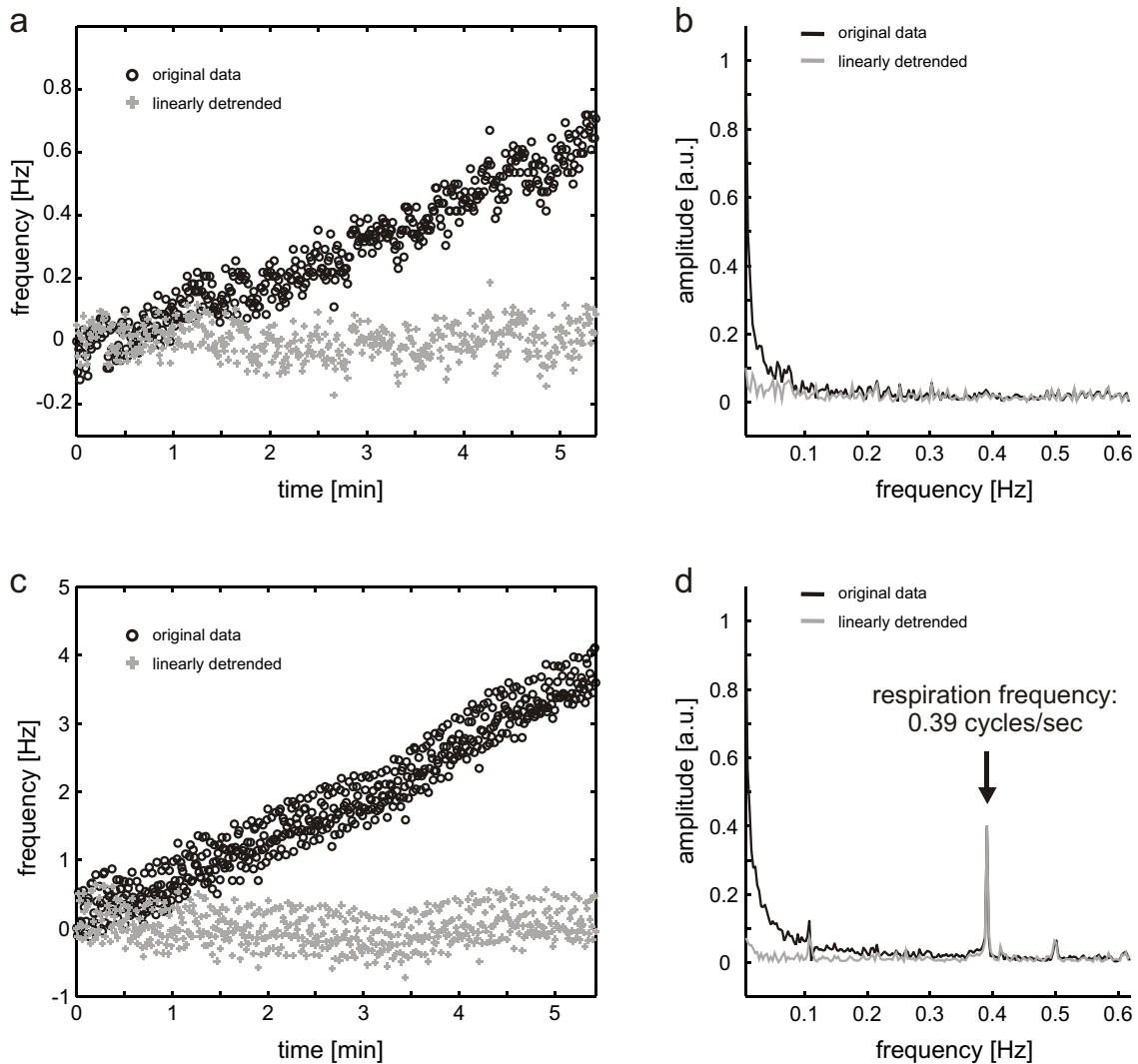


**Figure 5.10:** Analysis of the MR system frequency. (a) The system MR frequency drift in phantom experiments was mostly linear (black: original data, gray: linearly detrended). (b) No dominant periodicity was observed in the Fourier analysis of the MR frequency development and the low frequency tail disappeared after the linear trend was removed from the time domain data. (c,d) In the monkey, an additional periodicity of 0.39 Hz was observed which was attributed to the monkey respiration.

In all *in vivo* experiments, however, a regular frequency oscillation of 0.5–2.0 Hz peak-to-peak with a periodicity of 0.39 Hz was measured for the MR system frequency which matched the respiration frequency of the anesthetized monkey of 0.39 cycles/s (Fig. 5.10c,d). In addition, long term drifts of the MR system were observed that were mostly linear, but differed considerably in the range of  $\pm 10$  Hz *in vitro* as well as *in vivo*. The origin of these drifts is unknown, but gradient heating as observed by other groups during high duty-cycle gradient switching [149] was unlikely to be the reason, due to the long repetition time of 3 s for the spectroscopy applications. A frequency lock interval of 1.5–2.0 minutes was selected to ensure that during interleaved scan periods these drifts were well within the range of the frequency oscillations caused by regular lung ventilation. Notably, blood pressure measurements during acquisition would have induced a reversible frequency change and were, therefore, always carried out between acquisition periods. A representative record of the system frequency and the physiological parameters heart rate and expiratory CO<sub>2</sub> concentration are given in figure 5.11a,b,c. During maintenance of anesthesia, the variations of heart rate and expiratory CO<sub>2</sub> were small and only a quasi-linear frequency drift of 5.3 Hz/h was observed. In two exceptional cases, larger physiological changes of heart rate, blood pressure, expiratory CO<sub>2</sub> and body temperature were observed. They correlated well with strong irregular frequency variations which, therefore, could not be corrected for by the frequency lock approach. For stable physiological conditions during the first 55 min of the study, long term drifts were minimal and the spread of the MR system frequency was solely due to respiration (Fig. 5.11d: MR system drift, Fig. 5.11e: heart rate, Fig. 5.11f: expiratory CO<sub>2</sub>, data markers: +). During physiological disturbances of heart rate and expiratory CO<sub>2</sub> (55–100 min), strong variations of the MR frequency were observed. When the disturbances of the lock frequencies were recognized, the acquisition of metabolite spectra was interrupted and 3 series of water scans with 200/200/100 repetitions were acquired (TR 3 s, Fig. 5.11d: 1/2/3, data markers: \*). To improve readability, here only every fifth data point is shown (with an effective TR of 15 seconds). After reestablishment of stable physiological conditions (100–125 min), the MR system frequency stabilized at a new level of 25 Hz offset and, once again, only frequency changes due to respiration were observed.

The analysis of the series of spectra from period 1 and 2 yielded strong frequency drifts during the period of physiological disturbances rather than particular frequency jumps. Furthermore, a transient increase of up to 6.5 Hz in the line width (FWHM) of the water peaks was measured which is in agreement with the correlation of hypercapnia and BOLD reported in [150]. The phase stability of the first points in the time domain was not affected by physiological disturbances (standard deviation of periods 1&2: 5–6 degrees, period 3: 7 degrees), however, the amplitudes

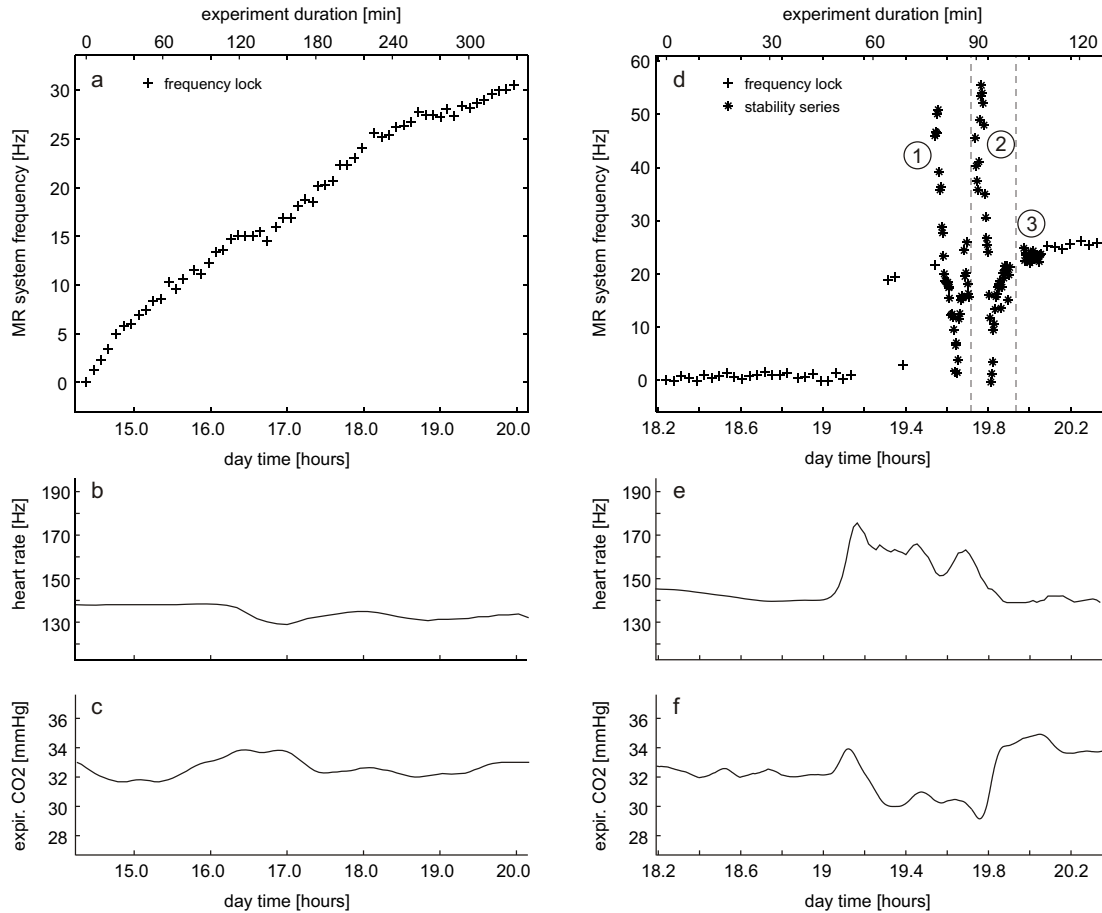


**Figure 5.11:** Correlation of the MR system frequency (including hardware and subject) and the subjects physiology. A slow drift of the system frequency of 5.3 Hz/h and a respiration-related frequency scattering (a) were observed during maintenance of anesthesia when the variations of the subjects heart rate (b) and expiratory  $\text{CO}_2$  concentration (c) were small. (d,e,f) In an exceptional case strong frequency drifts were observed during physiological disturbances (55–100 min). After reestablishment of stable physiological conditions (100–125 min), the system frequency stabilized at a 25 Hz offset level and only the breathing related frequency spread remained.

were strongly affected (std.dev. / mean of periods 1&2: 3-4%, period 3: 0.6%). This effect was even increased for the peak amplitudes in frequency domain (std.dev. / mean of periods 1&2: 4-12%, period 3: 0.5%). The stronger amplitude variation in the frequency domain than in the time domain fits well with the observed line width effects. For the minimal line width changes during period 3, the amplitude measures in time and frequency domain are comparable. Gross changes of physiological parameters like blood pressure, heart rate and body temperature were found to be correlated with strong oscillations of the MR system frequency. Extensive monitor-

ing of the animals vital functions, which is routinely performed during anesthesia, not only guaranteed the wellbeing of the animal but also served as a reasonable online indicator for irregular frequency fluctuations.

## 5.5 First Order Localized Shim Algorithm

Analytical and iterative methods have been proposed to provide optimal shimming. In general, analytical methods are preferred, since for iterative algorithms the required number of iterations strongly increases with increased parameter space and the convergence to an optimum value is not always guaranteed. Analytical methods, however, require the full or at least partial mapping of the magnetic field which is time consuming and not necessarily the case for iterative algorithms. Since very small voxel volumes were to be shimmed here, e.g. for performing MR spectroscopy in V1, very high resolution field mapping would have been required. Thus, a semi-iterative shim algorithm was implemented for a fast adjustment of the three first order shims. The algorithm performs a maximization of the FID length which is equivalent to a maximization of  $T2^*$  or the minimization of the field inhomogeneity (equ. (1.12)). The particular first order shims were serially modified and a Gaussian fitting routine (available from the Bruker ParaVision software) was used to determine the optimum shim value. The procedure was applied to all three first order terms and was repeated 2 to 3 times with increasing step resolution.

## 5.6 Software for Experiment Adjustment and Execution

The ParaVision software (Bruker BioSpin, Ettlingen/Germany) provides many hundred parameters of different types and classes to handle the 7 Tesla MR scanner. In addition, more parameters can be defined for the coding of user-defined MR sequences. Consequently, the search and adjustment of parameters during MR experiments becomes complex and inefficient. To this end, several software tools were developed that summarize the relevant experimental parameters and allow an easy and time-efficient definition of experiments and the adjustment of critical parameters. The software package itself is *Tcl* based and links the sequence software, the parameter handling and the experiment execution in ParaVision to the data analysis procedures that were provided mainly by *C* programs.

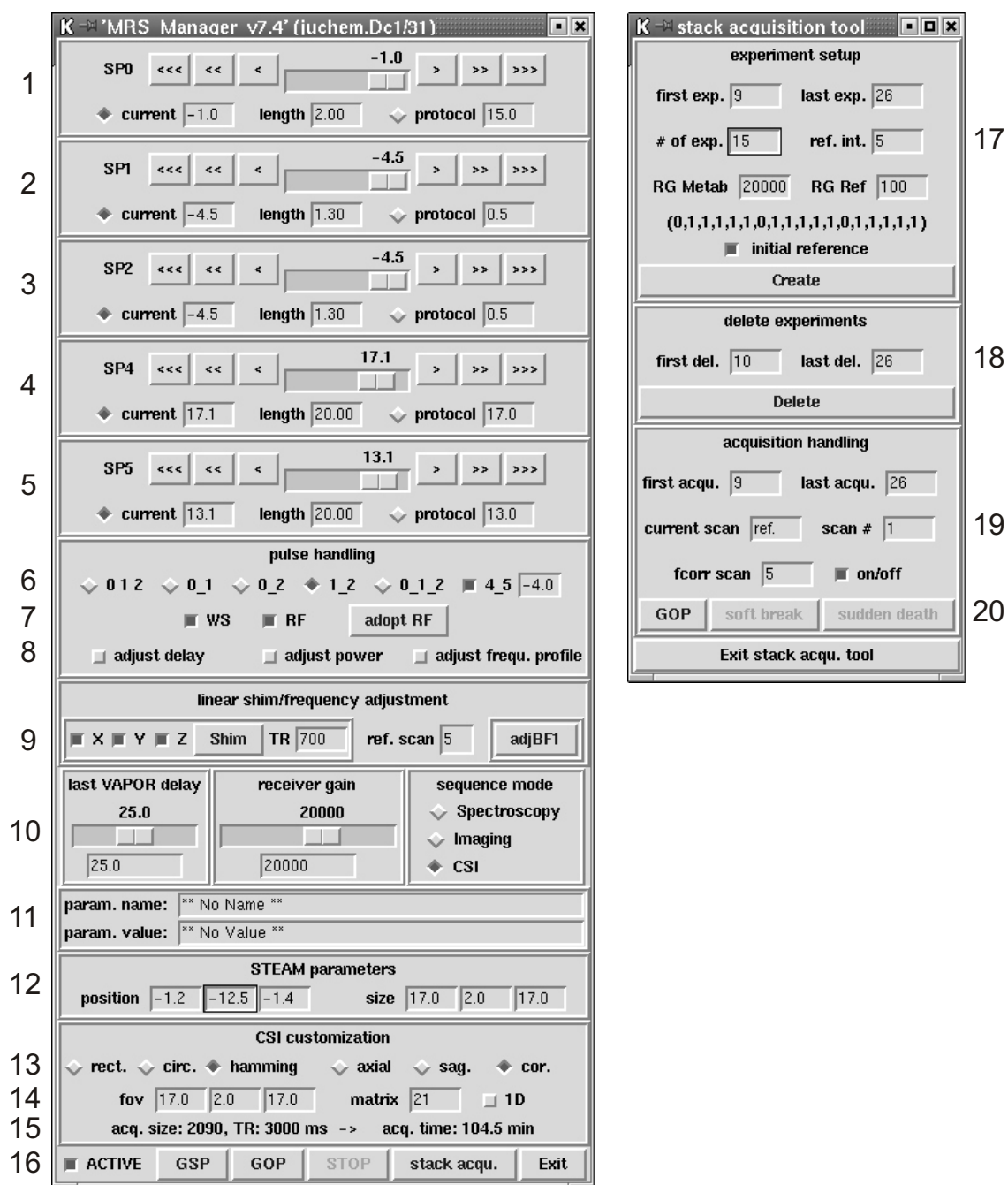


**Figure 5.12:** Software tools for the adjustment, quality control and execution of all type of MR spectroscopy and chemical shift imaging experiments. For explanations see text.

Figure 5.12 shows two of these tools. Others, like the OVS adjustment tool, are not shown for the sake of brevity. The length and the power of the three RF pulses for STEAM can be adjusted by the panels 1–3 and for VAPOR water suppression using the panels 4 and 5. The flags of number 6 provide the possibility to link particular pulses which significantly lowers the adjustment effort. The flags of number 7 enable the switching of the water suppression or the power of the RF pulses only. The optimization and adjustment procedures described in the previous sections were also implemented here to enable their time efficient execution. If one of the flags from number 8 is selected, an additional control panel appears and the parameters for the analysis or optimization for the delay between the VAPOR water suppression and the STEAM module, the optimum RF pulse powers for VAPOR or the VAPOR frequency profile can be selected. As an example, the data series of the RF power adjustment for VAPOR is shown in figure 5.13.

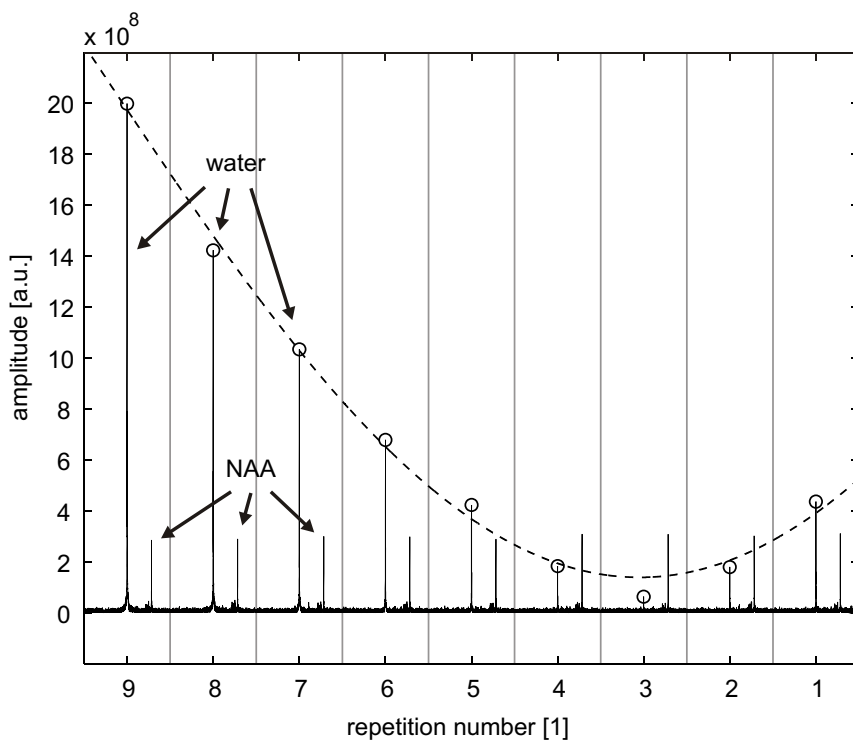


**Figure 5.13:** Algorithm for the adjustment of the RF power for VAPOR water suppression from a series of MR spectroscopy scans. The water signals show a clear minimum, but the metabolite resonances are not affected by the water suppression.

A series of  $^1\text{H}$  MR spectroscopy scans is acquired at variable RF power for the water suppression pulses. The amplitudes of the water peaks at 4.7 ppm show a strong dependence on the RF power adjustment for VAPOR and a clear minimum value is observed at repetition number 3 for which the RF power adjustment is optimal. Due to the well-defined frequency profile of VAPOR water suppression (see section 5.1) the water peak is suppressed almost to the noise level, but the metabolite resonances are not affected as can be seen e.g. from the NAA resonance at 2.02 ppm (compare Fig. 5.6). After defining a reference scan at number 9, localized first order shimming and the adjustment of the system frequency is possible. At number 10 the delay between the VAPOR and the STEAM module can be chosen, as well as the receiver gain and the MR spectroscopy method. Besides the options for single voxel MR spectroscopy and CSI, an imaging mode is supported that provides projections of the STEAM or the OVS profiles and allows a direct visual control of the sequence and RF pulse properties. All ParaVision or user-defined parameters can be modified using the interface of number 11. In number 12, the position and the size of the STEAM voxel is defined. Notably, the excited STEAM volume needs not to coincide with the imaging FOV for CSI. The CSI FOV, its orientation, the acquisition sampling scheme and the CSI matrix size are defined at number 13 and 14. At number 15, informational parameters are displayed assigning the total acquisition time for the currently selected set of parameters. The final row at number 16 allows to start the sequence in an adjustment mode (GSP), to start the experiment as selected (GOP), to stop it (STOP) or to exit the tool. The remaining button starts a subprogram that allows a fully automatic serial acquisition of all type of MR spectroscopy experiments with an optional inclusion of the frequency lock algorithm. The splitting of MR experiments into subunits was necessary to enable regular measurements of the monkey's blood pressure, for intermediate adjustments like the frequency lock, the acquisition of intermediate water references and in order to prevent data loss e.g. in case of a system crash. At number 17 and 18, protocols of interleaved metabolite and water reference scans, e.g. for eddy current correction, can be generated and deleted if required. The parameter setting of number 19 then defines the acquisition series and the usage of the frequency lock, before the serial experiment is started, interrupted or stopped at number 20.

## 5.7 Simulation of $^1\text{H}$ MR Metabolite Spectra

Most of the  $^1\text{H}$  brain metabolites have complex higher order spectra and an exact quantum mechanical calculation is required to describe them. Especially, the details of the MR sequence have to be considered to account for, e.g. coupling effects during the experiment [49, 151]. For the simulation of MR spectra the commercial NMR-SIM software package version 3.2 (Analytic Suite, Bruker, Ettlingen/Germany) was used to solve the quantum mechanical Liouville equation (equ. (1.4)) and to calculate the time evolution of the density matrix [152, 153]. With this program, homo- as well as heteronuclear spin systems with spin quantum numbers up to 2 can be simulated and relaxation processes are taken into account by a model based on the Bloch equations. Cross-correlation and cross-relaxation processes, however, are neglected.

The effect of a STEAM sequence on the spin systems was simulated by a pulse scheme that consisted of three 90 degree RF pulses. Broadband sinc RF pulses with 10 side lobes were used to achieve a homogeneous excitation profile over a frequency range of almost 50 ppm that certainly covered the relevant frequency band for  $^1\text{H}$  MR spectroscopy of brain metabolites between 0 and 10 ppm. The three FIDs and the unwanted echoes were spoiled by appropriate crusher gradients. In this idealized approach no slice selection gradients were applied for the STEAM pulses. This is a valid approximation if the transition zone of real RF applications is small compared to the center volume of the STEAM voxel for which the RF amplitudes are constant and of optimum strength. The parameters echo time TE, mixing time TM, magnetic field strength  $B_0$  and acquisition bandwidth BW were chosen according to the experimental conditions (TE 10 ms, TM 10 ms,  $B_0$  7 Tesla, BW 5 kHz). Since the simulations are essentially free of noise and line broadening, 32 k data points were simulated in the time domain. Notably, this is far more than the  $\sim 1$  k reasonable data points that can be acquired during *in vivo* MR spectroscopy experiments before the metabolite signals decay to the noise level. The metabolite Hamiltonians for the simulations were created based on literature values at appropriate number and type of nuclei, chemical shifts and couplings [21](see Appendix A). The MR spectra for all 20 simulated brain metabolites are shown in section 3.3.

For the generation of basis sets for the LCModel analysis of brain spectra, a consistent scaling and a frequency referencing had to be provided similar to the experimental measurement of the metabolite solutions. To this end, two singlet peaks were added to each spin system: formate at 8.44 ppm and TMS at 0 ppm. The calculation of the 20 metabolite spectra performed on a personal computer (Intel Pentium 4, 2.80 GHz) and the subsequent creation of a new set of basis spectra with



a normal PC required about 1 hour and made this approach preferable especially for the scientific use where the parameters are changing more often.

# Chapter 6

## Combined Passive and Active Shimming

Shimming is essential for all type of MR spectroscopy applications and becomes of even greater importance in high-field MR scanners, since susceptibility induced field distortions are increased at higher field strength (equ. (1.32),(1.33)). The compensation of the inhomogeneities therefore requires stronger shim fields, potentially exceeding the capabilities of the active shim device. In addition, regions of greatly differing magnetic susceptibilities, such as tissue-air transitions, e.g. in the vicinity of the ear canals or the cranial bone, may also require shim fields greater than those provided by active shimming. In practice, zero order terms, i.e. field offsets, that are small compared to the scanner field strength, do not pose problems and first order terms can be easily shimmed using the scanners gradient system. Second order terms, however, represent the main limitation in experimental setups when the shim requirements exceed the capabilities of the corresponding active shim device.

Considerable first and second order field distortions were observed in the visual cortex of the macaque monkey and, therefore, first and second order shimming is regularly applied to minimize the inhomogeneities. With the Siemens gradient/shim insert AC44, originally designed for human head scanners operating at a 3 Tesla field, active shimming at the 7 Tesla high field MR system was strongly limited. In fact, the shim strength requirements of the second order shim fields exceeded the available capabilities regularly for all second order channels multiple times. High quality second order shimming and consequently also MR spectroscopy were impossible to perform.

In the following, the development of a modular, passive second order shimming method is described. Simple ferro-shim geometries were derived in theory and optimized for maximum field strength and accuracy. The placement of modular ferro-shim assemblies for the experimentally most relevant second order shim terms in close proximity to the subject allowed the reproducible creation of shim fields many times larger than those of the scanners built-in electronic shim device. Subsequently, active shimming with the scanners shim device provided flexible fine tuning of the shim fields to the particular experimental conditions. The power of the combined passive (ferro-magnetic) and active (electronic) shimming approach to improve the quality of brain MR spectroscopy was demonstrated by shimming the macaques visual cortex in the 7 Tesla high-field MR scanner.

For the generation of strong and reproducible passive shim fields at minimized mass requirements permalloy sheets were used (Ni-Fe-alloy, VAC Vacuumschmelze, Hanau/Germany) due to the high saturation magnetization and the small remanence and coercivity. The permalloys saturation polarization was determined to be  $(0.752 \pm 0.004)$  T with a superconducting quantum interference device (SQUID) magnetometer (Quantum Design MPMS-XL, San Diego/USA, 300 K, 0–3 T) at the Max-Planck-Institute of Microstructure Physics in Halle/Germany (Fig. 6.1). It was reached at approximately 0.4 T without any observable coercivity. The density of the metal alloy was measured as  $(8.611 \pm 0.002)$  g/cm<sup>3</sup>.

A measure for the degree of similarity of the (theoretical or experimental) passive shim fields  $B_{shim}$  and the spherical harmonic target fields  $B_{harm}$  was needed for the quantitative evaluation of the accuracy of the passive shim fields. To this end, the classical Pearson-product-moment correlation was modified as follows:

$$R^2 = 1 - \left( \frac{\sum_{i=1}^n B_i^{shim} B_i^{harm}}{\sqrt{\sum_{i=1}^n (B_i^{shim})^2 \sum_{i=1}^n (B_i^{harm})^2}} \right)^2 \quad (6.1)$$

The magnetic field values  $B_i$  of all  $n$  spatial positions are equally weighted and the measure is invariant under global linear transformations, such as scalings and shifts. Due to the Cauchy-Schwarz inequality the quotient is bounded in the range  $[-1, 1]$ ; the modified  $R^2$  value is therefore zero for identical fields, approaching 1 as the field differences increase. By removing the subtraction of the means from the Pearson-product-moment, it provided a measure of the identity of two groups of point pairs,

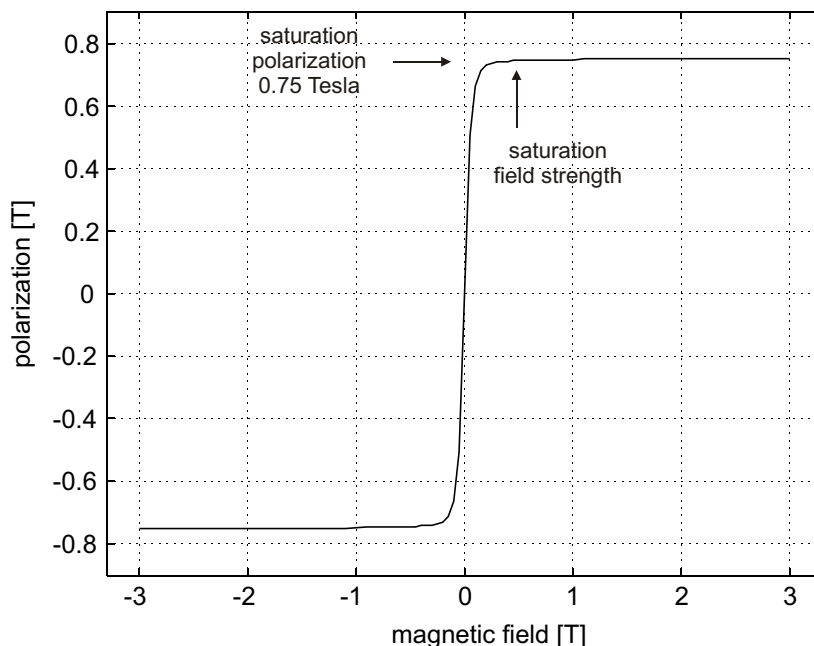


**Figure 6.1:** Magnetization curve of the permalloy used for passive shimming. The saturation magnetization was reached at  $\sim 0.4$  T and no coercivity was observed.

where relative offsets are considered as a decrease of similarity. The modified  $R^2$  value, however, is a single scalar and does not provide any information about the nature of contamination. In a second step of quality assessment the theoretically optimized shim fields were decomposed into first-to-fourth order spherical harmonic functions which provided a direct measure of the type and strength of residual deviations.

## 6.1 Theoretical Design and Optimization of Passive Shim Fields

The goal of the geometrical design for passive shimming was to achieve both maximum accuracy and design simplicity. Based on the theory of dipole fields and basic symmetry considerations, ferro-shim geometries were chosen that would be most promising for the generation of the second order spherical harmonic fields (Fig. 6.3).

A cylinder geometry was selected as the basic design block in order to easily achieve rotational and planar symmetries. Calculations were used to validate and optimize the identity of the created shim fields and the spherical harmonic target functions.

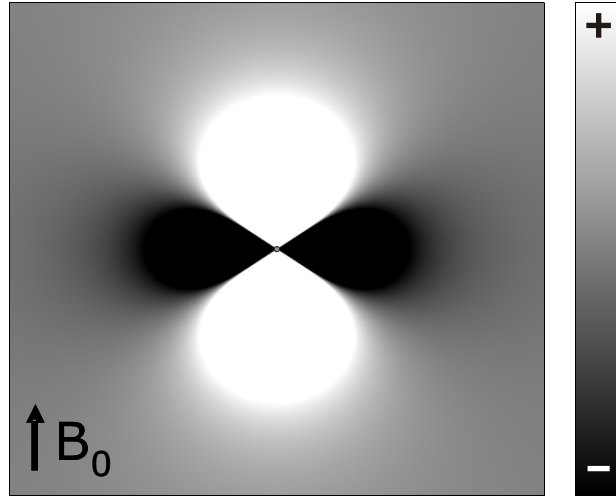


**Figure 6.2:** *Magnetic field of a dipole. The field of a magnetic dipole is positive above and below the dipole and negative in its horizontal periphery. At the 'magic angle' of 55 degrees the dipole field is zero.*

Given the magnetic susceptibility of the permalloy and the dimensions of the tube, the expected shim fields were computed for different shim geometries when placed into a homogeneous magnetic field for which the saturation state of the magnetization was reached. The shim elements were discretized by a finite number of volume elements and a dipole field was attached to each volume element. The total field distortion was computed by superposition of the fields of the individual dipole fields. This dipole model has been shown to produce the correct field distribution at the limit of small volume elements [154, 155]. The shim field distributions were calculated on an isotropic 3D data grid of size  $101 \times 101 \times 101$  voxels. The ferro-shim geometries, by convention, were placed on the surface of an hypothetical cylinder with a diameter of 100 times the spacing of the point grid. Although spherical harmonics are dimensionless functions, shim fields have physical units. Since the spatial pattern of the passive shim fields was to be analyzed and optimized, rather than particular values, first the arbitrary scaling was removed. The integral of the root mean square differences within a 3D cube volume between the magnetic field and the spherical harmonic field was then determined and minimized. To this end, a single optimized global linear transformation (i.e. a multiplication factor and an offset) was determined for the passive shim field. The numerical routine used for minimization was stopped when relative changes of both the scaling and the offset value dropped below 0.01%, which was always achieved in less than 10 iterations. The approach could be also understood as mimicking the physical process of shimming (mounting/unmounting of ferro-shim, frequency correction). Notably, the  $R^2$  value was not

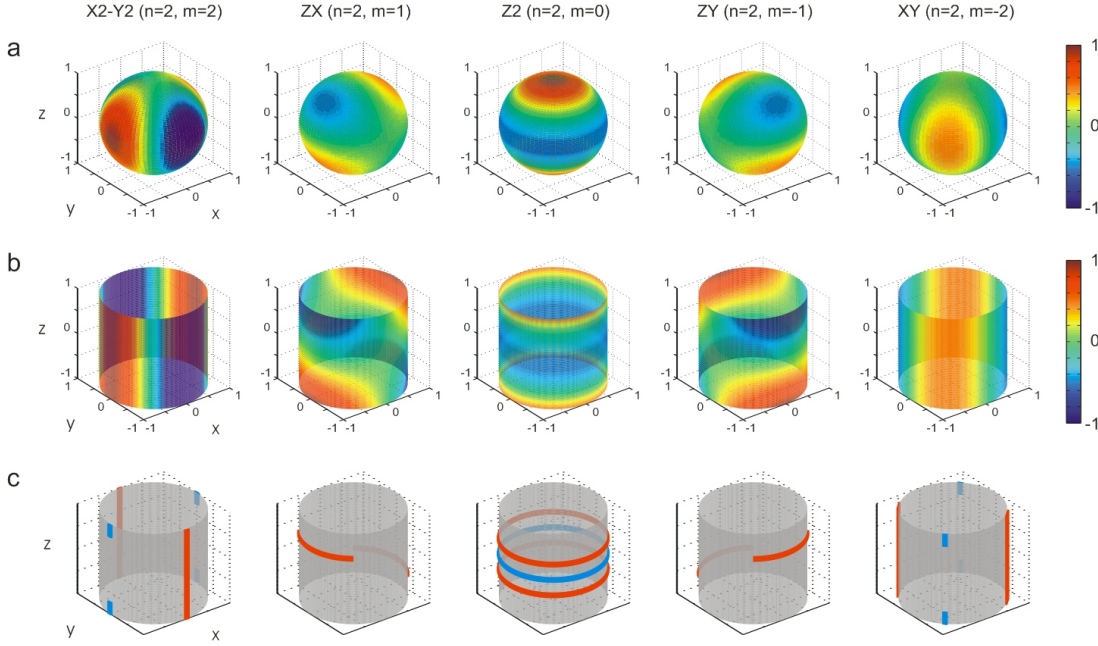


**Figure 6.3:** 3D visualization of the normalized second order spherical harmonic functions  $X2-Y2$ ,  $ZX$ ,  $Z2$ ,  $ZY$ ,  $XY$  ( $n=2$ ,  $m=-2,-1,0,1,2$ ) for a sphere (a) and for a cylinder section (b). (c) Theoretical optimization of the ferro-shim design yields simple geometries of 2 pieces per shim term (red) for the generation of passive shim fields that approximate the corresponding spherical harmonics. The experimental effort for passive shimming with  $+Z2$  and the amount of ferro-shim required for the  $X2-Y2$ ,  $XY$ , and  $+Z2$  terms could be minimized at tradeoffs in the shim field accuracy (blue).

used here as a target function for the determination of the optimal global linear transformation, since the measure was too sensitive and quickly approached 1 for considerably different field distributions. In contrast, the use of a conventional norm as the target function was numerically more stable. For evaluation and optimization of the permalloy geometries the centered  $27 \times 27 \times 27$  grid points (N 19683) of the full FOV were considered as the sensitive region for  $R^2$  determination, which is 27%. Cubic spline interpolation was used to determine the optimum geometry condition for which  $R^2$  was minimal. The robustness of the shim fields against non-optimal dimensioning of the shim geometries was determined as the range of the  $R^2$  function around the optimum geometry, for which the  $R^2$  values increased less than 0.01.

The  $X2-Y2$  and  $XY$  shim fields were generated by pairs of ferro-shim lines placed vertically to the front and to the back of the shim tube or to opposite diagonal sides, respectively (see Fig. 6.3c, red). The shape of the generated  $X2-Y2$  and  $XY$  shim fields critically relied on the ratio of the length of the shim lines versus their

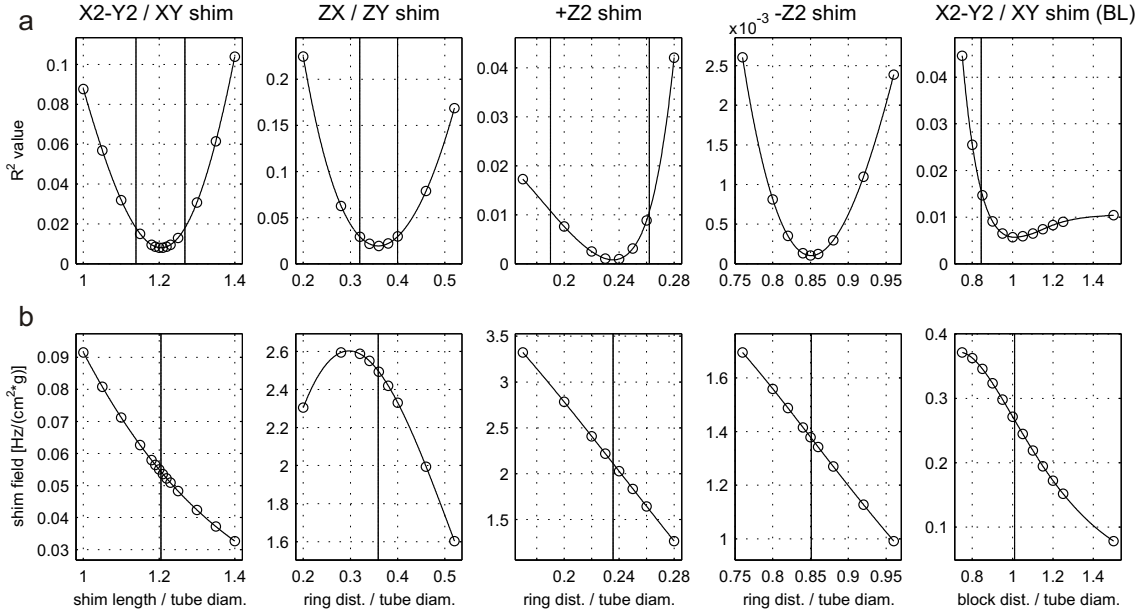


**Figure 6.4:** Theoretical optimization results for the generation of passive shim fields similar to the second order spherical harmonics X2–Y2, ZX, Z2, ZY and XY with the ferro-shim geometries of figure 6.3.c. (a) For all second order terms, well-defined optimum geometries were found with  $R^2 < 0.02$ , so that the generated passive shim fields were highly similar to the corresponding spherical harmonic target fields. (c) Based on the permalloy’s saturation magnetization, the absolute strength of the shim fields was calculated as a function of the geometry. The analysis of the tradeoff block design (BL) for X2–Y2 / XY shimming revealed a 4.9-fold increase of shim power at the cost of a –Z2 contamination.

distance given by the tube diameter with an optimum ratio of 1.20 ( $R^2=0.01$ ). For a shim tube diameter of 25 cm, the optimal length of the vertical ferro-shim lines was 30.1 cm. For geometrical variations smaller than 0.07 ( $\sim 1.6$  cm), the  $R^2$  value increased by less than 0.01. Based on the saturation magnetization of the permalloy, the created shim field was calculated to be  $0.054 \text{ Hz}/(\text{cm}^2\text{g})$ . Two quarters of a loop placed at the opposite sites of the shim tube were used to generate ZX / ZY shim terms (Fig. 6.3c). For a ratio of 0.36 for the vertical distance of the ring parts as compared to the tube diameter, a minimal  $R^2$  value of 0.02 was found (9.0 cm for a tube diameter of 25 cm). The tolerances against the vertical displacement were determined to be 0.04 ( $\sim 1.0$  cm) and the absolute ZX / ZY shim fields were calculated to be  $2.50 \text{ Hz}/(\text{cm}^2\text{g})$ . For the 4 tesseral second order shim fields, 90 degree rotations of the ferro-shim assemblies or a mirroring with respect to the center axial plane was enough to flip the polarity for the X2–Y2 / XY shims and the ZX / ZY shim terms, respectively. The zonal Z2 shim, however, required a qualitatively different shim constellation to achieve positive and negative polarity. In both cases,

a parallel pair of loops was used, as proposed in [40], but separate optimizations of the ring distance versus the tube diameter were necessary to approximate the correct shape and polarity (Fig. 6.3c, red. For  $+Z2$ , a minimum  $R^2$  value of  $10^{-3}$  was achieved at a ratio of the ring distance versus the ring diameter of 0.24 (5.9 cm). The tolerance against misadjustment of the geometry ratio was determined to 0.05 and 0.03 at the low and the high ratio side, respectively (-1.1 cm / +0.7 cm). A minimum  $R^2$  value as small as  $10^{-4}$  was determined for  $-Z2$  at a geometry ratio of 0.85 (21.3 cm). Shim strengths were determined as  $2.11 \text{ Hz}/(\text{cm}^2\text{g})$  and  $1.38 \text{ Hz}/(\text{cm}^2\text{g})$  for the  $+Z2$  and  $-Z2$  shim fields, respectively.



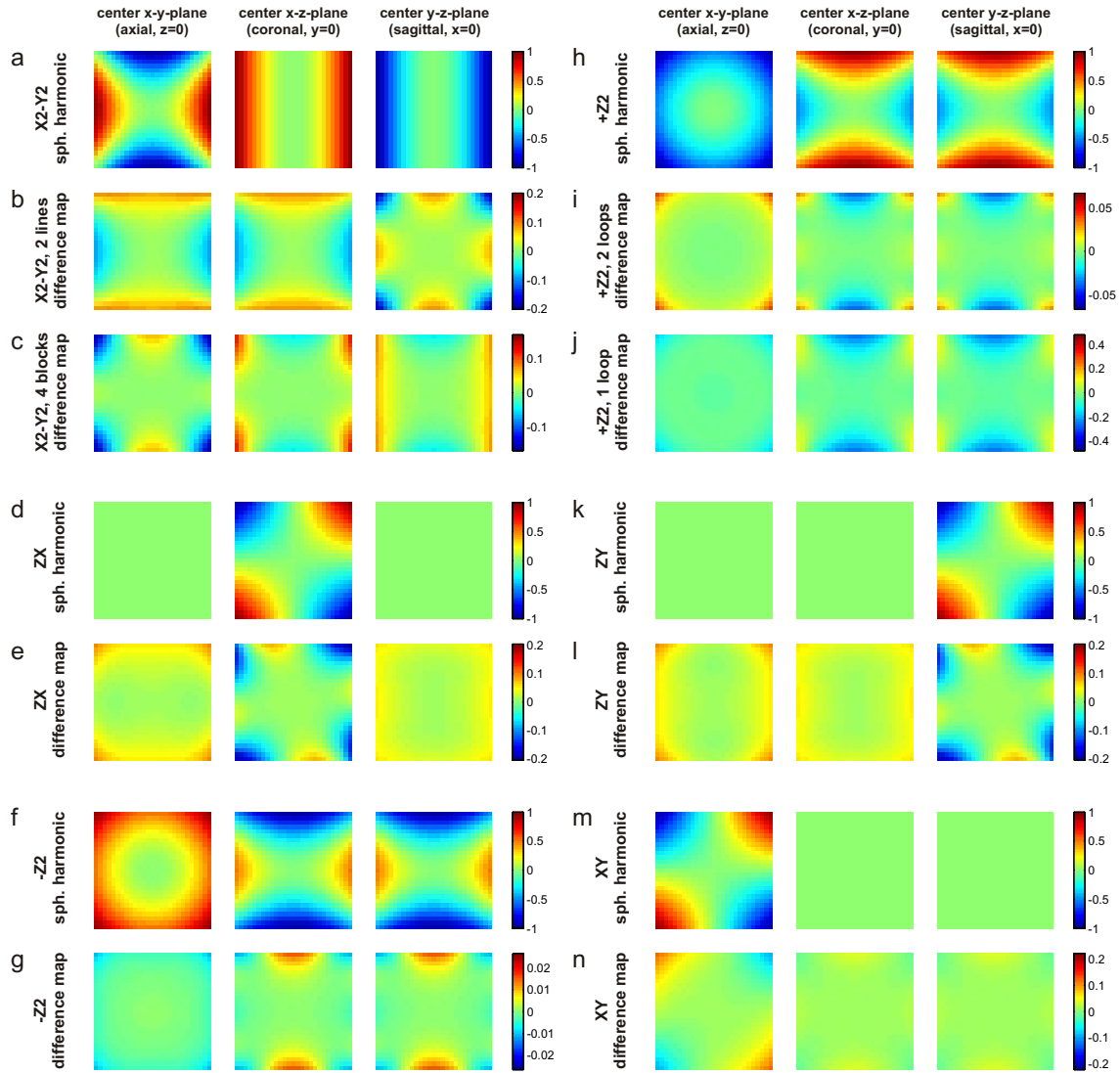


**Figure 6.5:** *Quality assessment of the theoretically optimized passive shim fields. The three center slices are shown for each of the second order spherical harmonic target fields (a,d,f,h,k,m) and followed by difference images of the attained passive shim fields minus the target fields (in a.u.). In (c) the -Z2 contamination of the 4 block shim design for X2-Y2 was removed before the difference analysis.*

### 6.1.1 Tradeoffs for X2-Y2, XY and +Z2 Shimming

The ferro-shim mass that was needed to generate the X2-Y2 / XY fields was many times higher than for the other exact shim terms. This could be understood by taking into account the strong mutual cancellation effects that were necessary for the X2-Y2 / XY field profiling. The replacement of the 2 vertical ferro-shim lines by 4 blocks with vertical spacing at 90 degree intervals led to a field distribution

**Table 6.1:** Results of the passive shim optimization. The optimum  $R^2$  values are summarized for all second order terms (X2–Y2, ZX, Z2, ZY, XY) and for the tradeoff geometries, i.e. the block design (BL) for X2–Y2 / XY shimming and the single loop approach for the generation of +Z2. The optimized geometry ratios are given as dimensionless numbers and (in [cm]) for the realization of a 25 cm tube diameter (real.). The experimentally measured field values per mass (in [Hz/(cm<sup>2</sup>g)]) are similar to the theoretically predicted ones. Notably, the artifactually induced –Z2 contribution of the block design was removed before the  $R^2$  calculation. (s: single loop, d: double loop, BL: block design)

shim term	X2-Y2/XY	ZX/ZY	+Z2(d)	-Z2	(BL)	+Z2(s)
$R_{opt}^2$	0.01	0.02	0.001	0.0001	0.01	0.05
optimized ratio	1.20	0.36	0.24	0.85	1.01	-
opt. ratio (real.)	30.1	9.0	5.9	21.3	25.2	-
theo. field/mass	0.054	2.50	2.11	1.38	0.27	4.94
exp. field/mass	0.056 (0.001)	2.36 (0.12)	1.98 (0.02)	1.26 (0.01)	0.27 (0.01)	4.61 (0.06)

that was a combination of X2–Y2 / XY and –Z2 shim fields (Fig. 6.3c, blue). Due to the vertical gaps between the blocks the mutual cancellation effects were greatly reduced and the amount of ferro-shim that was necessary to generate the same strength of the X2–Y2 / XY shim field was 4.9 times smaller than that of the 2 line element approach. A minimal  $R^2$  value of 0.01 was found for a ratio of 1.01 for the vertical block distance versus the tube diameter. A reasonable tolerance limit could be determined only at the low ratio side (0.17 / 4.1 cm) because  $R^2$  values remained small for larger vertical distances of the ferro-shim blocks. For the +Z2 shim term the double loop structure was reduced and simplified to a single loop centered horizontally around the iso-center. The generated field distribution matched the theoretical target function, but the overall accuracy of the generated shim field was reduced relative to the two-loop approach. A difference calculation of the attained passive shim fields and the spherical harmonic target fields confirmed the previous results (Fig. 6.5).

### 6.1.2 Field-of-View Dependence of the Passive Shimming

The optimization of the theoretical ferro-shim geometries included a FOV that was 27% of the shim tube diameter. An analysis of the shim field accuracy as a function of the FOV size was done to determine (for the optimization result at 27% FOV) the maximum FOV for which the spherical harmonic target fields were sufficiently well approximated. Notably, the –Z2 contribution was removed from the block design

field distributions  $X2-Y2 / XY$  before the  $R^2$  value calculation. The shim fields almost perfectly approximated the spherical harmonic target functions for small FOV size, and the reduction of the shim field accuracy was moderate for voxel sizes up to 40–50% of the shim tube diameter (Fig. 6.6).

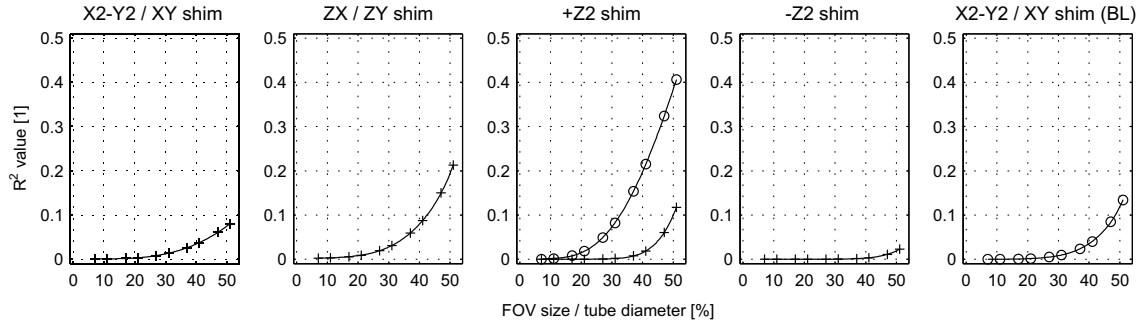


**Figure 6.6:** Comparison of the theoretically optimized passive shim fields and the second order spherical harmonic target fields as a function of FOV size. The optimization results from a FOV of 27% the tube diameter are shown for the best solutions (Fig. 6.3c, red; symbol: +) and for the 4 block shim tradeoffs (BL) for  $X2-Y2 / XY$  and the single loop solution for  $+Z2$  (Fig. 6.3c, blue; symbol: o). The passive shim fields closely approximate the target fields for reasonably small FOVs.

### 6.1.3 Analysis of the Residual Field Contaminations

The deviations of the theoretically computed shim fields from the spherical harmonic target fields were analyzed by fitting the passive shim fields to the first-to-fourth order spherical harmonics. Because all shim geometries were chosen to be symmetrical with respect to the three main axes, first order terms, i.e. linear field gradients, were not observed. The attained second order field contributions are shown in table 6.2. They were normalized with respect to the corresponding field term to evaluate the desired versus non-desired field contributions. For all except of one of the passive shim fields, the field terms to be generated exceeded the unwanted ones by at least a factor of 10. The only exception was the X2–Y2 tradeoff shim achieved with 4 blocks of ferro-shim, for which the  $-Z2$  contamination was about three times larger than the desired field term. Because strong and accurate  $+Z2$  shim fields were easy to accomplish, the drawback for the generation of strong X2–Y2 / XY shim fields was of only minor importance. In all cases third order contributions were negligible and values of the fourth order field contributions ( $[Hz/cm^4]$ ) did not exceed  $\pm 1\%$  of the generated second order shim fields ( $[Hz/cm^2]$ ).

**Table 6.2:** *Analysis of the passive shim fields by spherical harmonics decomposition. For all theoretically generated passive shim fields the contaminations from other terms are at least a factor of 10 smaller. The only exception is the block design for the X2–Y2 / XY shimming for which an artifactual  $-Z2$  term is induced that can be easily experimentally compensated.*

	X2-Y2	ZX	Z2	ZY	XY
X2-Y2	1	0	0.05	0	0
X2-Y2(BL)	1	0	-2.99	0	0
ZX	-0.05	1	-0.05	0	0
Z2(s)	0	0	1	0	0
Z2(d)	0	0	1	0	0
-Z2	0	0	1	0	0
ZY	0.05	0	-0.05	1	0
XY	0	0	0.01	0	1

## 6.2 Experimental Validation of Passive Shim Fields

Based on the quantitative optimization results, the theoretically derived field patterns and strengths were experimentally controlled on an agar gel phantom. A  $27 \times 27 \times 27 \text{ mm}^3$  FOV was used, corresponding to 11% of the 25 cm tube diameter. The passive shim field was determined from the condition of the mounted shim tube minus the field distribution without the shim tube which was fitted to first and second order spherical harmonics and removed by postprocessing. In some cases experimental mounting asymmetries of the ferro-shims caused first order shim terms, which were much smaller than the first order shim capabilities of the gradient system. Here, the focus was on the accuracy of the second order shim terms. Since these were partially masked by the first order contributions, the linear gradients were removed from the 3D field maps before the determination of the  $R^2$  value.

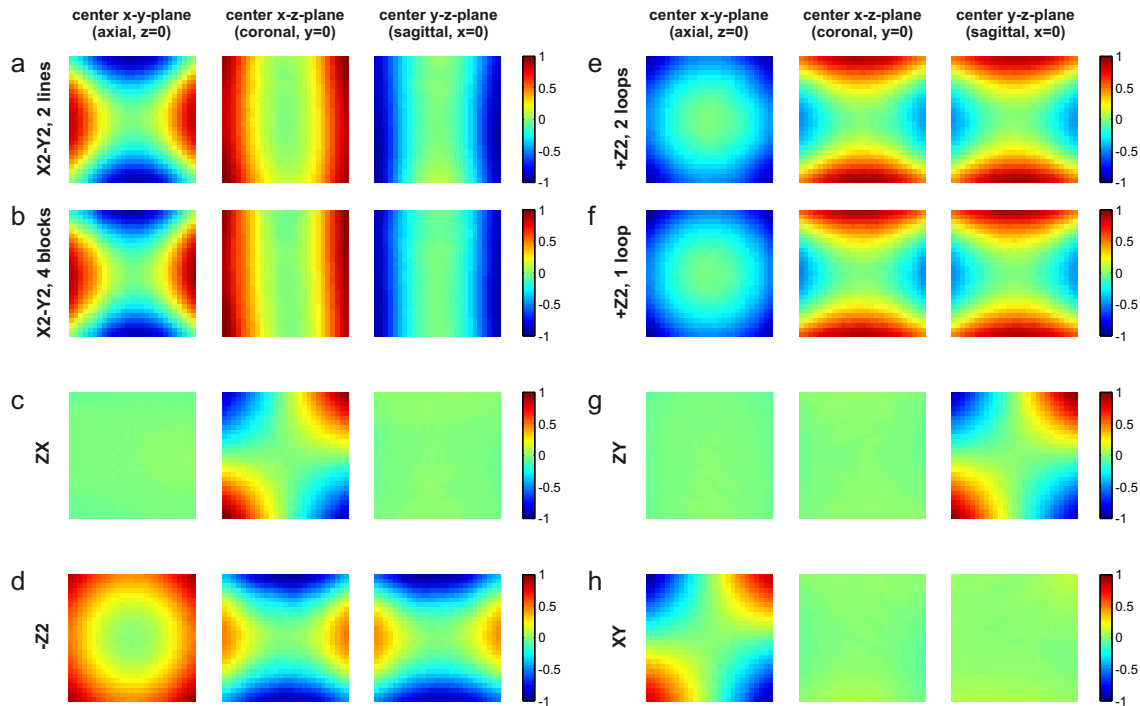


**Figure 6.7:** *Experimental validation of the generation of the second order passive shim fields on a gel phantom. A gradient echo FLASH imaging sequence with an isotropic resolution of 1 mm at 7.0/9.5 ms echo time was used to measure the field distributions from a  $27 \times 27 \times 27 \text{ mm}^3$  cube voxel (11% FOV, shim tube diameter 25 cm, in a.u.). The second order spherical harmonics were well approximated by the passive shimming and  $R^2 < 0.02$  was achieved in all cases.*

Phantom field mapping confirmed the theoretical optimization results of all shim fields and polarities. Modified  $R^2$  values below 0.02 were achieved in all cases, and deviations from the target field distributions were small (Fig. 6.7).

### 6.3 Combined Passive and Active Shimming in the Monkey

The passive shim tube was adjusted once for every particular experimental setup, according to the subject anatomy, target hemisphere, and head position. Field mapping with FASTMAP was used to quickly measure the field distortions in terms of the required shim fields (see section 2.7). The subject was taken out of the magnet and modular ferro-shims were mounted on the shim tube based on the established requirements. In practice, it proved to be advantageous to start with the strongest requirements, before the others were added. This was because experimental misadjustments could not be avoided per se. For the adjustment of a new shim tube 4–8 iterations (1–2 h) were required. Notably, the adjustment of a new shim tube required an almost complete removal of the field inhomogeneities by passive shimming to maximize the probability that the small dynamic range of active shimming was also sufficient for the following sessions.

The improvement of the achievable magnetic field homogeneity by combined passive and active shimming of the macaque monkey brain *in vivo* was addressed by quantitative field mapping (Fig. 6.8).

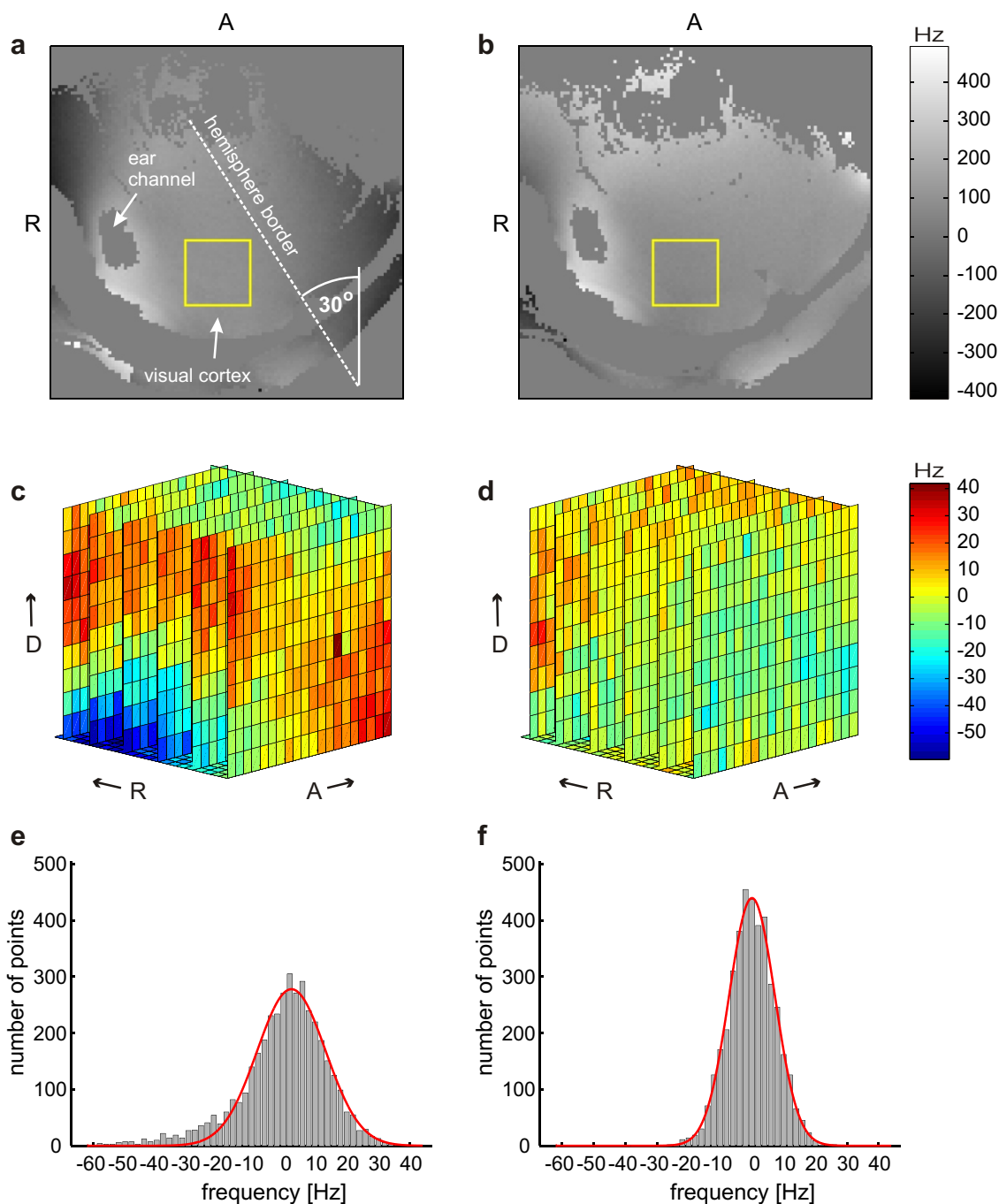


**Figure 6.8:** Comparison of the combined passive and active shimming with constrained active shimming only for field homogenization of the visual cortex of a macaque monkey at 7 T. Axial field maps from the 30 degrees rotated monkey head of the constrained (a) and of the combined (b) shimming are depicted (A: anterior, R: right, D: dorsal). The shimming volume, placed into the visual cortex gray and white matter, is indicated by the yellow box. Field deviations of several hundred Hertz remained over the whole brain volume after active shimming only (a), whereas the major large scale field distortions were removed by the combined shimming (b). Maximum frequency differences were about 100 Hz in the purely actively shimmed voxel (c) and further reduced by a factor of 2 after combined shimming (d). The FWHM of the Gaussian fitted frequency distribution was reduced from 25.4 Hz to 17.0 Hz (e,f).

The yellow box assigns the  $10 \times 10 \times 10 \text{ mm}^3$  ROI placed onto the visual cortex gray and white matter. The field distributions after active shimming only (given the current hardware constraints), and after shimming with the combined passive and active approach, were compared. A 3D field map was acquired at zero shim before the different types of shimming were applied to quantify the distortions of the magnetic field and thus the shim fields required to correct for them. Decomposition of the ROI's field distribution into spherical harmonics revealed second order terms of X2-Y2:  $3.9 \text{ Hz/cm}^2$ , ZX:  $-19.0 \text{ Hz/cm}^2$ , Z2:  $-75.0 \text{ Hz/cm}^2$ , ZY:  $33.6 \text{ Hz/cm}^2$ , XY:  $-3.3 \text{ Hz/cm}^2$ . A first and second order field decomposition of at least five field maps per shim channel in a previous phantom study provided the full correlation matrix of the currently installed AC44 shimming device. Linear regression of the data points yielded maximum shim field strengths of  $X = 589 \text{ Hz/cm}$ ,  $Z = 587 \text{ Hz/cm}$ , and  $Y = 511 \text{ Hz/cm}$  for the linear shim terms and  $X2-Y2 = 1.86 \text{ Hz/cm}^2$ ,  $ZX = 3.74 \text{ Hz/cm}^2$ ,  $Z2 = 5.21 \text{ Hz/cm}^2$ ,  $ZY = 3.69 \text{ Hz/cm}^2$ ,  $XY = 1.84 \text{ Hz/cm}^2$  for the second order ones at correlation coefficients  $>0.98$  in all cases. Considering the interdependencies of the shim channels for all 8 first and second order terms, the absolute field distortions translated to relative shim field requirements of X2-Y2: 365%, ZX: -465%, Z2: 1540%, ZY: -970%, XY: -130% with respect to the currently available active shim power. After constrained active shimming only large scale field fluctuations remained in the brain (Fig. 6.8a). Simple mounting of the shim tube, which had been adjusted in a previous session six weeks before, was enough to remove the main field inhomogeneities and to permit optimal first and second order active shimming. Although the shimming was focused on improving the homogeneity within the localized  $10 \times 10 \times 10 \text{ mm}^3$  cube volume inside the brain, the major large scale field fluctuations were considerably reduced (Fig. 6.8b). Strong frequency variations with a range of 100 Hz remained within the ROI after constrained active shimming, whereas the frequency spread was reduced by a factor of two in this case with combined passive and active shimming (Fig. 6.8c,d). The FWHM of the Gaussian fitted frequency distribution was reduced from 25 Hz to 17 Hz (Fig. 6.8e,f).

With the combination of passive and active shimming, line widths of 11–13 Hz for water and 9.5–12 Hz for the Cr + PCr resonance at 3 ppm were reproducibly achieved in  $5 \times 5 \times 5 \text{ mm}^3$  ( $125 \mu\text{L}$ ) MR spectroscopy voxels from the visual cortices of different monkeys and hemispheres.



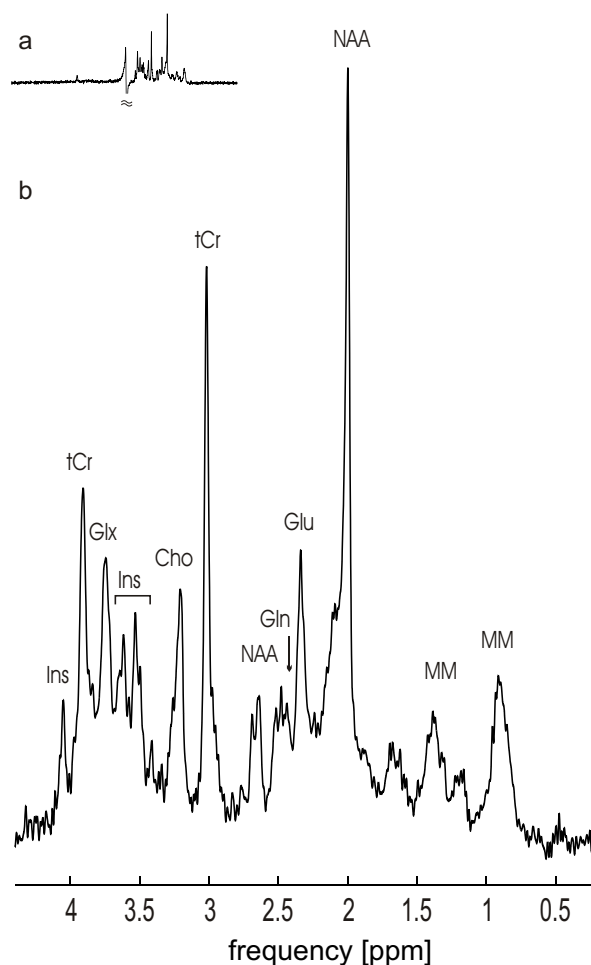


**Figure 6.9:**  $^1\text{H}$  MR spectrum from the visual cortex of a macaque monkey at 7 T (STEAM, NA 1024 / 51 min). A modest exponential line-broadening of 1 Hz was applied before Fourier transformation and zero-order phasing. First order phasing was not necessary, and the baseline was flat outside the spectral regions of metabolites and water without correction (a). Line widths were measured to 11.0 Hz for water and 9.6 Hz for the creatine + phosphocreatine (Cr + PCr) methyl singlet at 3.03 ppm. The spectral quality and SNR were sufficient to quantify more than 10 metabolites.

No additional artifacts such as  $B_0$  eddy currents or spikes were observed in any of the MR spectroscopy (or imaging) data that could be attributed to passive shimming. Neither baseline correction nor first order phasing was required in any of the experiments. In the presented spectrum more than 10 metabolites could be quantified from a voxel of visual cortex gray and white matter (Fig. 6.9). Notably, even  $\gamma$ -aminobutyric acid (GABA) was above the detection limit (as defined by a 20% CRLB threshold), glutamate could be separated from glutamine, and creatine from phosphocreatine.

## 6.4 Significance and Discussion

Simple ferro-shim geometries were derived to generate field distributions very similar to the second order spherical harmonic functions. Experimental frequency shifts caused by offsets inherent to the passive shimming and experimental imperfections accumulated up to  $\pm 3$  kHz. However, compared to the Larmor frequency of 300 MHz, at 7 T these field drifts could be considered as negligible with respect to potential effects on the signal strength and dispersion of the  $^1\text{H}$  brain metabolite spectra.

The measurement of the saturation magnetization of the permalloy allowed the calculation of absolute passive shim fields and enabled a direct comparison of theoretical optimizations and experimental results. The magnetization curve of the ferromagnetic permalloy saturated at an external magnetic field strength of  $\sim 0.4$  T. Consequently, there was no risk of memory effects in the 7 T MR system for repetitive use of the ferro-shims and the absolute shim fields generated by a particular shim tube could be expected to remain unchanged. The results are valid not only for the particular metal alloy and the magnetic field strength used in this study, but for all magnetic field strengths and ferromagnetic materials for which the saturation state is certainly reached. Rescaling the shim fields by the ratio of the saturation magnetization provides a direct guide for the generation of second order shim terms and the absolute strengths in other setups.

The size of the monkey head is approximately 50% of the human head in a linear dimension; spatial regions to be shimmed (for example for single voxel MR spectroscopy) are scaled down accordingly. The optimization analysis of a 27% FOV (6.8 cm for the tube diameter of 25 cm) was reasonable and sufficient for the monkey setup, since this FOV size covered a large part of the brain. However, depending on the particular shim term, even FOV sizes of 40–50% could be shimmed with reasonable accuracy. The passive shimming method can be applied to the human setup simply by scaling up the tube diameter and all shim dimensions by a factor of 2–3. Because tolerances against experimental variations scale accordingly, relative errors will be even smaller than those in the monkey setup. A Siemens gradient/shim insert AC44, originally designed for human head scanners operating at a 3 T field, was used for active shimming. Therefore, the active shim capabilities were not expected to meet the requirements for shimming the brain of the macaque monkey at 7 T. In fact, the available capabilities were regularly exceeded for all second order channels multiple times and were always highest for the Z2 term with values of 800–1500% of the available shim power. This finding of strong Z2 field distortions qualitatively fits with data from the human brain at 3 T [156]. For all monkeys, the shim requirements were qualitatively comparable for equal setups, but the ab-

solute values varied up to a factor of two, with the example presented in Fig. 6.8 posing the highest requirements. Strong X2–Y2 / XY shim field distortions favored the tradeoff approach of 4 blocks of ferro-shim (instead of 4 lines) for experimental purposes. The generation of strong and accurate +Z2 shim fields to compensate for the induced –Z2 terms was easy to achieve and the 4 blocks approach furthermore permitted the independent mounting and unmounting of all shim terms and avoided geometrical crossings. For Z2 shimming, both the ease of mounting a single loop and the 2.4-fold enhancement of the shim field at identical ferro-shim mass, made this approach preferable for the given geometrical conditions.

High reproducibility of the setup and of the positioning of the monkey head and the shim tube was considered as a key issue for reproducible shimming conditions. As determined by MR imaging, spatial deviations of the brain position were in the range of 0–2 mm between sessions and rotations were negligible. Moderate reproducibility of other setups (like clinical scanners) might be a limiting factor for the repetitive use of a fixed ferro-shim geometry for passive shimming. Minimum experimental effort was required to implement the simple ferro-shim geometries of only two (multi-layer) pieces per shim term. The ease of implementation suggests that the combination of active and modular passive shimming might be a reasonable way to overcome insufficient shim power even in less reproducible setups, where modifications in each session are required. Furthermore, MR imaging and spectroscopy in rodents, for which setups are also well-defined and inter-subject variations of the anatomy and the shim requirements are limited, could use passive shimming based on a default shim tube for a pre-shim adjustment. This method of combined modular passive and active shimming is of high practical relevance in particular for high field MR setups and/or shimming of regions which inherently require high second order shim fields, like the skull region, the vicinity of the ear canals or the orbitofrontal cortex. A cylindrical geometry was used as the basic design module to achieve the simplest ferro-shim geometries for minimal ferro-shim mass. The basic design module for the generation of shim fields by passive shimming used in [40] was a sphere. The transformation of the numerically optimized ratios for Z2 shimming (+Z2: 0.24, –Z2: 0.85) into angles yield values of  $76.7^\circ$  and  $49.6^\circ$  which nicely reproduced the analytical results of  $76.2^\circ$  and  $48.6^\circ$ , respectively. This cross-check of methods further validates the numerical analysis developed and the optimization procedure presented here. The advantage of the numerical method used here is that it allows the direct analysis of the quality of field distributions for particular, even complex, geometrical conditions. For the ZX / ZY shim terms two quarters of a loop were used to generate reasonable shim fields and 2 line elements or 4 blocks were applied for the X2–Y2 / XY shims. In ref. [40] at least 11 pieces were necessary for the generation of ZX / ZY shim terms and no less than 17 pieces for X2–Y2 / XY shimming. Elegant

and more general solutions for passive shimming with ferromagnetic material have been proposed which might additionally include higher order terms. The drawback of these techniques, however, is that they require many hundreds or even more than 1000 metal pieces [41, 82]. The modularity similar to active shimming techniques and the reduction to 2 pieces per shim term is an important simplification of passive shimming that makes the method applicable also for passive shimming within single sessions. The further decomposition of the generated shim fields into spherical harmonic functions enabled the generation and analysis of the block design for the strengthened X2–Y2 / XY shimming. Because it was started from the theory of dipoles and basic symmetry considerations with somewhat arbitrary default geometries, one cannot claim that the proposed design for passive shimming is the best solution possible for accuracy of shim fields and ease of experimental implementation. Due to symmetry considerations, however, it is unlikely that solutions with less than two pieces of ferro-shim for X2–Y2, XY, ZX, ZY and -Z2 can be found.

# Chapter 7

## Chemical Shift Imaging of the Visual Cortex

Limited sensitivity is a major problem for *in vivo* CSI of brain metabolites. Improvement of SNR is usually accomplished at the expense of reduced spatial resolution. Yet, most structures of interest in the primate brain, e.g. the regions of the cortical sheet, are in the range of a few cubic millimeters or below, while cubic centimeter voxels are commonly used in CSI studies of the human brain.

The dedicated setup for performing MR spectroscopy experiments in the anesthetized macaque, as well as the previously described physical and methodological improvements were used to push the resolution limit for CSI in the non-human primate model. The separation of gray and white matter structures from the visual cortex was achieved and the feasibility of CSI at *cortical* dimensions was proven.

### 7.1 High Resolution CSI of the Visual Cortex

For zoomed CSI, a STEAM localization scheme was used, which was extended by a conventional  $13 \times 13$  phase encoding scheme (FOV  $17 \times 2 \times 17$  mm<sup>3</sup>, TE 10 ms, TM 10 ms, TR 3 s, BW 5 kHz, NA 42). STEAM pulse lengths of 2 ms were sufficiently short to maximize the gradient amplitudes for slice selection, thereby minimizing the CSD for the CSI slice to  $1.1 \times 0.1 \times 1.1$  mm<sup>3</sup>/ppm. With an excitation frequency offset of  $-1.66$  ppm ( $-500$  Hz), the synthesizer frequency was set to 3 ppm for the <sup>1</sup>H metabolite excitation. Since relevant metabolite peaks are expected in the range of 2 to 4 ppm in <sup>1</sup>H MR spectroscopy of the brain, frequency deviations that gave rise to CSD were in the range of  $\pm 1$  ppm or below.

Thus, the effective CSD for the excitation of the measured metabolites was less than  $1.1 \times 0.1 \times 1.1 \text{ mm}^3$ . Signal loss due to T2 relaxation and signal dephasing by J-coupling were minimized using a short echo time. Given the technical constraints of the gradient system BGA38 used for this study (maximum strength 80 mT/m, rise time  $<200 \mu\text{s}$ ), the minimal echo time TE was predominantly determined by the length of the STEAM pulses. An echo time shorter than 5 ms was technically feasible with the MR system and sequence; the profile of the optimized RF pulses, however, required a tradeoff in the echo time and TE was chosen to 10 ms. Shimming was performed on a 20-mm cubic voxel for all first- and second-order shims with FASTMAP [99] using automated serial acquisition [157]. Shim requirements of the Z2 and X2-Y2 shims were close to the maximum available shim strength of the BGA38, but the field maps along the six diagonal projections were still flat after the shimming procedure. No third-order contribution was observed in the selected region of interest. A considerable improvement of the field homogeneity within the CSI slice ( $17 \times 2 \times 17 \text{ mm}^3$ ) was achieved by additional volume selective shimming of first-order terms running the MR sequence in pure spectroscopy mode without phase encoding (see section 5.5). A Gaussian filter (67% at the edges) was applied to the spatial  $13 \times 13$  CSI data matrix. Then the data were zero-filled to a  $27 \times 27$  matrix and Fourier transformed to the spatio-spectral domain. The nominal spatial resolution of  $1.3 \times 2 \times 1.3 \text{ mm}^3$  was decreased by this procedure to  $1.4 \times 2 \times 1.4 \text{ mm}^3$ , as determined from the width of the spatial response function (SRF) at 64% of its maximum value [63]. Metabolite quantification was achieved with LCModel by voxelwise peak deconvolution in the spectral domain from 1 k time domain data points (acquisition time 0.2 s). Absolute quantification was done assuming 8 mM total creatine (Cr + PCr) in gray matter tissue [72].

The CSI FOV was placed in coronal orientation to the visual cortex of the left hemisphere as shown in Fig. 7.1. The spatial excitation profile of the saddle coil was homogeneous in the region of interest, as determined from the CSI slice profile of water using a readout gradient. The orientation of the surface coil used for signal reception was parallel to the CSI FOV, which is least susceptible to sensitivity changes across the CSI volume. The line width of the water signal from the total localized CSI volume was 18.8 Hz. The duration of the total experiment was approximately 6 h using a  $13 \times 13$  matrix, TR 3 s, and 42 averages. The carefully supervised maintenance of the monkeys physiology and optimally controlled system performance guaranteed both the well-being of the subject and stable conditions for the entire MR acquisition period. Metabolite quantification was achieved by voxelwise fitting in the frequency domain, which worked well for all CSI voxels. The output from LCModel provided metabolite concentrations with error estimates (CRLB), as well as global line width (FWHM) and SNR estimates. The FWHM

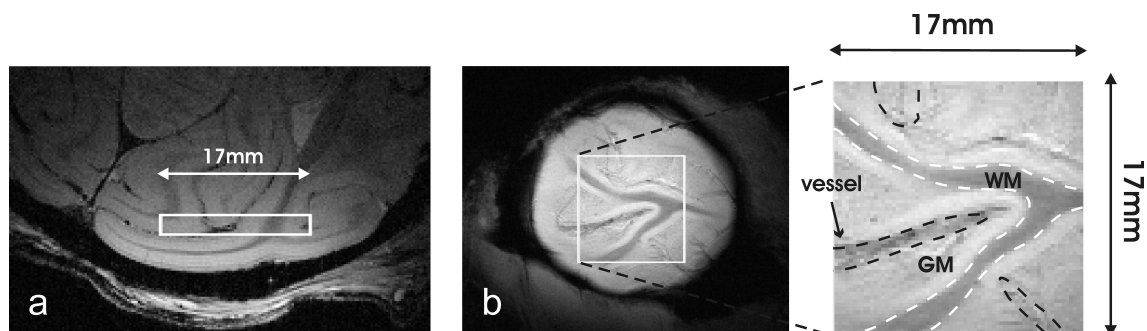


**Figure 7.1:** Anatomical scout images (FLASH) of the left hemisphere of the monkey brain after a 30 degrees leftward rotation. The CSI FOV ( $17 \times 2 \times 17 \text{ mm}^3$ ) is shown as a white box in the axial (a) and the pseudocoronal views (b), respectively. In (a) a single slice was selected; in (b) all slices that were covered by the CSI slice were summed together. From the zoomed CSI FOV, a white matter structure (white dashed contour) surrounded by gray matter can be identified, as well as additional anatomic features (black dashed contours), for instance, a vessel.

value is not a direct measure of the true full width at half maximum of a particular metabolite. Experimentally confirmed, however, it turned out to be a good estimate for the line width of the Cr + PCr singlet at 3.03 ppm [145]. The mean of the metabolite FWHM estimates of all CSI voxel spectra as determined by LCModel analysis was  $15.1 \pm 4.0 \text{ Hz}$  (mean  $\pm$  std).

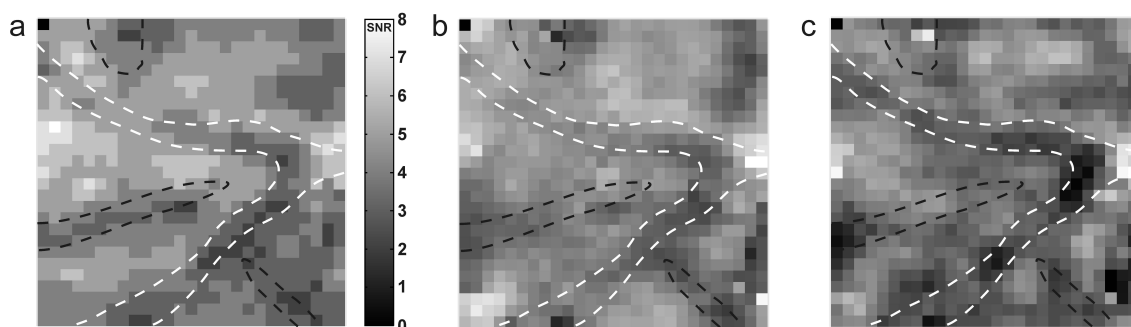


**Figure 7.2:** LCModel maps. Mapped quantitative results of the spectral analysis done voxelwise with LCModel. (a) Global metabolite SNR ( $4.2 \pm 1.1$ , mean  $\pm$  std). Compartments of gray and white matter tissue as well as additional anatomic features (e.g., a vessel) can be identified (compare to Fig. 7.1). (b) Map of NAA + NAAG concentrations. (c) Map of Glu + Gln concentrations.

Global metabolite SNR estimates were  $4.2 \pm 1.1$  (mean  $\pm$  std), shown in a SNR map in Fig. 7.2a. Anatomic structures are clearly distinguishable in the multislice FLASH images (Fig. 7.1b, matrix:  $256 \times 256 \times 41$ , FOV  $64 \times 64 \times 20.5 \text{ mm}^3$ ,

TE 15 ms, TR 1700 ms) like the white matter tissue compartment surrounded by gray matter or a blood vessel in the left central part of the FOV. Maps of metabolite concentrations of NAA + NAAG and Glu + Gln are shown in Fig. 7.2b and c, respectively. For increased grayscale contrast of the metabolite maps, 1 outlier (34 mM) of the 729 voxel concentration values was removed from the Glu + Gln map and 9 outliers (21-31 mM) were removed from the NAA + NAAG map (matrix  $27 \times 27$ ). All outliers were exclusively located in the FOV periphery and this procedure was not applied to any type of quantitative analysis. Cramér-Rao lower bounds over the entire CSI FOV were  $11.4 \pm 3.7\%$  for Cr + PCr,  $10.1 \pm 2.4\%$  for NAA + NAAG, and  $15.9 \pm 6.6\%$  for Glu + Gln. A total of 11/729 (1.5%) outliers for Cr + PCr, 10/729 (1.4%) for NAA + NAAG, and 9/729 (1.2%) for Glu + Gln were excluded from the quantitative analysis, for which the values were outside of  $\pm 3 \sigma$  of the initial distribution of the CRLB's. The metabolite ratios were 1.43:1 and 1.32:1 for NAA + NAAG versus Cr + PCr in gray matter (GM) and white matter (WM), according to the anatomy-based tissue segmentation (see Fig. 7.3a). Similarly, the metabolite ratios were 1.30:1 and 1.04:1 for Glu + Gln versus Cr + PCr in gray and white matter, respectively. These results are similar to the metabolite concentrations reported from healthy human brain [72,158,159]. Gray and white matter brain tissue was segmented based on anatomic images for a statistical analysis of the metabolite concentration as a function of tissue type (Fig. 7.3a). The spatial dependence in the excitation of protons with different chemical shift due to CSD was less than  $1.1 \times 0.1 \times 1.1 \text{ mm}^3$ , i.e., less than 2 voxels in the CSI matrix of  $27 \times 27$ . Inside the CSI FOV, where the STEAM excitation profile was homogeneous, the CSD had minimal effect. Voxels from the two outer lines were avoided for further analysis to account for the frequency-dependent signal weighting at the borders of the CSI FOV. Since a 2D phase encoding scheme was used for spatial encoding of the metabolite magnetization, no CSD artifact was expected from the image encoding. Under the assumption of 8 mM Cr + PCr concentration in gray matter brain tissue [72], quantitative scaling provided a white matter concentration of  $7.3 \pm 1.4 \text{ mM}$  for Cr + PCr (mean  $\pm$  std). Glu + Gln concentrations were  $10.5 \pm 2.6 \text{ mM}$  in GM and  $7.6 \pm 2.7 \text{ mM}$  in WM. NAA + NAAG concentrations were  $11.5 \pm 2.6 \text{ mM}$  in GM and  $9.6 \pm 2.0 \text{ mM}$  in WM. Histograms of all metabolite concentrations are shown in Fig. 7.3b.



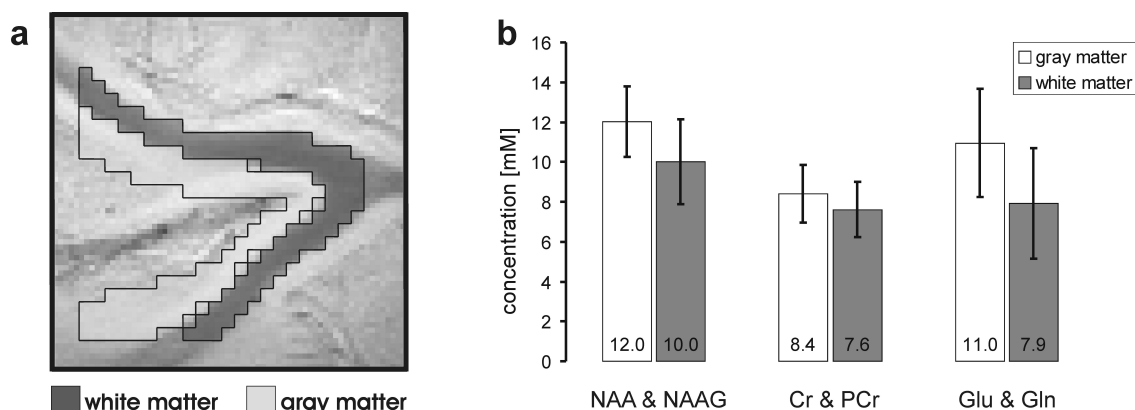


**Figure 7.3:** Statistical analysis of the CSI metabolite concentrations. (a) Selected brain tissue ROIs of gray (bright shading) and white (dark shading) matter in the CSI FOV from the visual cortex of a macaque monkey measured by  $^1\text{H}$  CSI at 7 T. (b) Statistical analysis of the brain metabolites NAA + NAAG, Cr + PCr, and Glu + Gln from cortex gray and white matter tissue. Absolute quantification was achieved under the assumption of 8 mM Cr + PCr concentration in gray matter tissue. Metabolite concentrations were significantly higher in gray matter for all three brain metabolites (Wilcoxon rank-sum test,  $P \leq 2 \cdot 10^{-5}$ ).

Shapiro testing revealed that group data were not Gaussian distributed for the particular metabolites in both tissues (Cr + PCr:  $P = 0.089$  (GM),  $P = 0.0034$  (WM); Glu + Gln:  $P = 0.61$  (GM),  $P = 0.009$  (WM); NAA + NAAG:  $P = 0.0001$  (GM),  $P = 0.089$  (WM)). Therefore, a Wilcoxon rank-sum test was used and the null hypothesis of higher mean concentrations in white matter tissue was tested for each metabolite (Cr + PCr:  $P = 2 \cdot 10^{-5}$ , Glu + Gln:  $P = 9 \cdot 10^{-12}$ , NAA + NAAG:  $P = 1 \cdot 10^{-9}$ ). Rejection of the null hypothesis led to the result that the mean values of the metabolite concentrations were significantly higher in gray matter than in white matter tissue for all three metabolites (Fig. 7.3b). The consistently lower metabolite content for NAA + NAAG, Cr + PCr, and Glu + Gln in white matter tissue fits well with some of the literature reports [72, 158]. For the values of NAA + NAAG in Ref. [159] it is reported that NAA concentrations were lower in GM than in WM (0.9:1).

## 7.2 Significance and Discussion

One advantage of CSI versus the serial acquisition of multiple single voxel MR spectra is its inherently consistent quantitative scaling. When inhomogeneities of the CSI sensitivity profile are small, spectra from different locations intrinsically have the same scaling. In contrast, when single voxel spectra from different locations are compared, consistent scaling must be provided by quantitative references, which may include additional error sources. CSI also overcomes the problem of accuracy in repositioning a single sensitive volume in repeated studies of the same subject. This issue is critical for metabolite measurements in an organ with sharp variations in metabolite concentration on a submillimeter scale. A source of potential error is the inhomogeneous receive characteristic of the surface coil, which might be specifically important for quantitative results. Here, the surface coil was positioned parallel to the CSI FOV (L-R), as this orientation is least susceptible to sensitivity changes across the CSI volume; e.g., a CSI slice perpendicular to the surface coil (A-P) would have maximum variation across the slice. The effective sensitivity profile of the CSI FOV depends on several parameters, such as the sensitivity profiles of the RF coils or the frequency profiles of the STEAM and the OVS modules. Two controls for the sensitivity profile of the CSI FOV were applied here: (1) a readout gradient along the x-, y- or z-direction, used to image the magnetization of water along projections, i.e., integrals of the magnetization along one particular direction; (2) integration of water peaks of a CSI water reference scan to get a direct 2D image of the effective sensitivity. The disadvantage of both methods is that the water content is known to be different in GM and WM tissue [65]. Therefore the measured *sensitivity map* does not reflect the effective sensitivity only, but the sensitivity map weighted by the visible water content. Both methods, however, refer to the final sensitivity profile that included all types of influences mentioned above. A possible extension could be to include an additional reference measurement with the homogeneous saddle coil in transceive mode to determine the contribution of the inhomogeneous profile of the surface coil. Additionally,  $B_1$  measurements could be performed. Notably, artifacts such as baseline distortions and fat signals were small and mostly localized when the CSI volume included parts of the cranial bone marrow. The local metabolite content was strongly reduced in these regions, but strong artificial signal spread over the entire CSI FOV, as reported in literature [160], was not apparent. There are mainly two sources of artificial signal spread over the entire FOV originating from signal either inside or outside the CSI FOV. A careful selection of appropriate RF pulse shapes was used to minimize errors in STEAM excitation/localization (sinusoidal filtered sinc-pulses with five side lobes) and to optimize the OVS module (hyperbolic secant pulses with a relatively sharp frequency profile). The minimal

spatial gap between the CSI FOV and the OVS module reduced the residual bone marrow magnetization.

To summarize, the feasibility of CSI with a spatial resolution in the millimeter range ( $1.4 \times 2 \times 1.4 \text{ mm}^3$ ,  $\sim 4 \mu\text{L}$ ) was demonstrated in the primate brain which corresponds roughly to a factor 80–500 smaller voxel volumes than what is commonly used in CSI of the human brain [161,162]. Based on different metabolite concentrations of NAA + NAAG, Glu + Gln, and Cr + PCr, a white matter compartment from the visual cortex with a width of 1-3 mm was separated from the surrounding gray matter tissue. Metabolite concentration ratios of white versus gray matter tissue as well as between metabolites of interest were in agreement with literature values. In conclusion, it was shown that  $^1\text{H}$  CSI of brain metabolite is feasible at *cortical* resolutions which is important for further detailed neuroscientific studies of monkey visual cortex.

# Chapter 8

## Acquisition Weighted Chemical Shift Imaging

Based on the proof of feasibility for high resolution CSI of the macaque cortex in chapter 7, the in-plane resolution limit that is achievable with the current setup was determined to be in the range of 1–2 mm. In these experiments, a conventional sampling scheme with a full k-space coverage was used. As an extension, k-space weighted CSI acquisition was evaluated and implemented to improve the spatial response function (SRF) and, thereby, the spatial specificity and the reliability of the data. To this end, the CSI FOV of  $17 \times 2 \times 17 \text{ mm}^3$  was kept with the aim to achieve the same in-plane resolution of 1.3 mm.

### 8.1 Theoretical Comparison of Weighting Schemes

To determine the most reasonable weighting scheme, a box car function of constant amplitude representing the conventional full k-space coverage was compared to the Hamming and Hanning filter functions (Table 8.1, [163]). The Hanning filter function has been shown to be a reasonable compromise between localization accuracy and sensitivity [164] and, therefore, is currently the most widely used weighting scheme [62, 63, 165]. The generation of 2D filters from the 1D Hanning and Hamming functions was achieved by rotation around the k-space center, i.e. the indexing was substituted by a distance parameter.

**Table 8.1:** One-dimensional spatial filter functions. For a box car filter covering the full  $k$ -space the amplitudes  $y$  are constant. In case of Hanning/Hamming weighting schemes, the filter value  $y$  is a function of filter position  $k$  and filter dimension  $n$ .

filter	function
box car	$y = 1$
Hanning	$y(k+1) = 0.50 - 0.50 \cos(2\pi \frac{k}{n-1})$ , $k = 0, \dots, n-1$
Hamming	$y(k+1) = 0.54 - 0.46 \cos(2\pi \frac{k}{n-1})$ , $k = 0, \dots, n-1$

Without spatial filtering the SRF shows strong sidebands (Fig. 8.1a,d) and each voxel receives signal contributions not only from the considered voxel volume, but from the biggest part of the FOV. The side bands of the SRF and the concomitant spatial contaminations can be minimized by applying spatial low pass filters (Fig. 8.1b,c). However, this is at the cost of a broadening of the central peak of the SRF and leads to a reduction of the attainable spatial resolution (Fig. 8.1e,f).

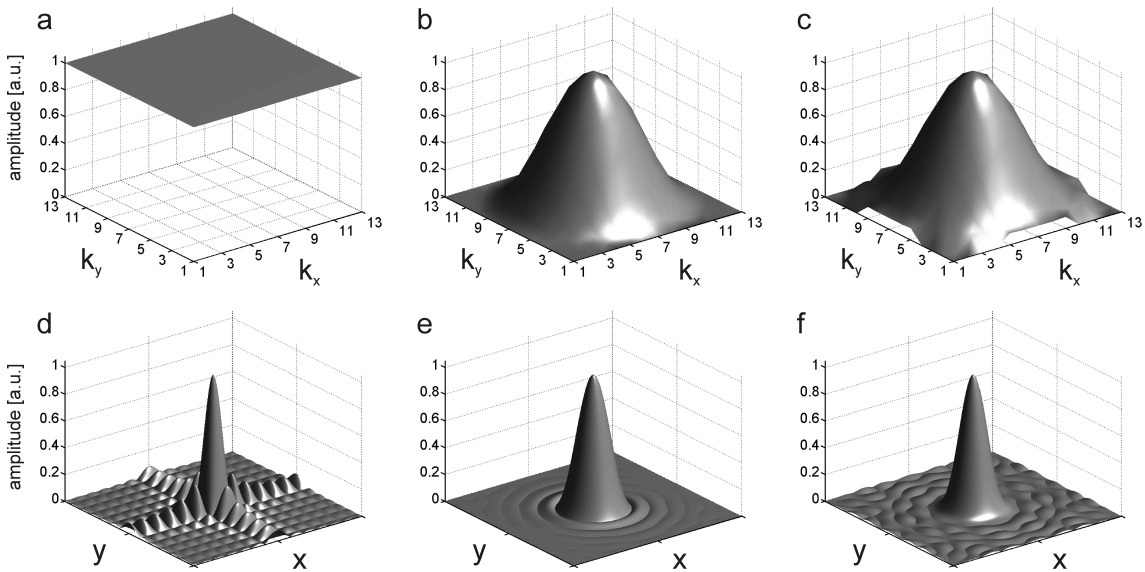


**Figure 8.1:** Analysis of the magnitude spatial response functions (SRF) for 3 spatial filter functions with a matrix size of  $13 \times 13$ . First row: Box car (a), Hanning (b) and Hamming (c) filter functions. Second row: The corresponding SRFs provide characteristics of spatial resolution and localization accuracy.

For conventional k-space coverage without spatial filtering the width of the central SRF peak at 64% of its maximum amplitude reproduces the nominal spatial resolution of equation (1.31) and corresponds to the maximum attainable spatial resolution of the imaging modality (Fig. 8.2a, [62]).

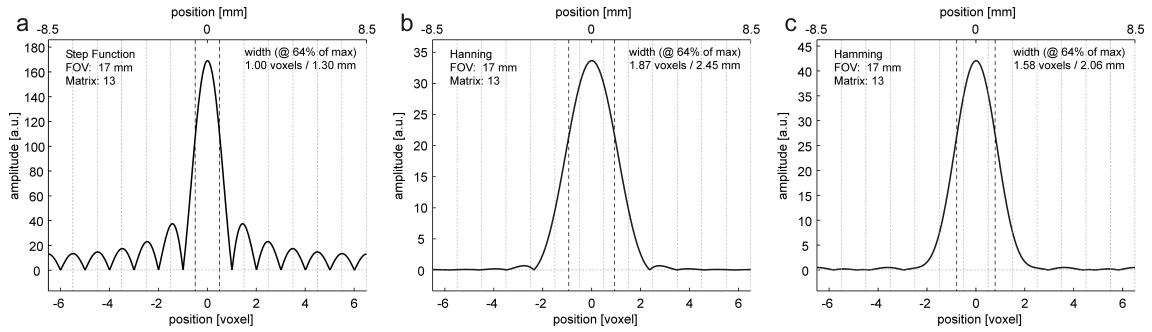


**Figure 8.2:** Analysis of the magnitude SRF for box car (a), Hanning (b) and Hamming (c) acquisition schemes. Hanning/Hamming filters suppress side lobes of the SRF at the cost of broadening the central peak, i.e. a loss in spatial resolution. The 64% level of the peak of the SRF defines the spatial resolution and is assigned by vertical dashed lines.

Without spatial filtering, the nominal in-plane resolution of a  $13 \times 13$  CSI phase encoding matrix applied to a  $17 \times 17$  mm<sup>2</sup> FOV is 1.3 mm (Fig. 8.2a). In comparison, the width of the SRF for the Hanning weighted acquisition scheme is increased by a factor of 1.87 and the spatial resolution is reduced from 1.3 mm to 2.45 mm (Fig. 8.2b). For the Hamming weighting the resolution is reduced from 1.3 mm to 2.06 mm equivalent to a broadening of the SRF by a factor of 1.58 (Fig. 8.2c). The SRF of the Hanning filter shows one dominant side lobe before it quickly decays to zero. The first side lobe of the Hamming SRF is less pronounced, but contributions from larger distances are slightly higher compared to those of the Hanning SRF.

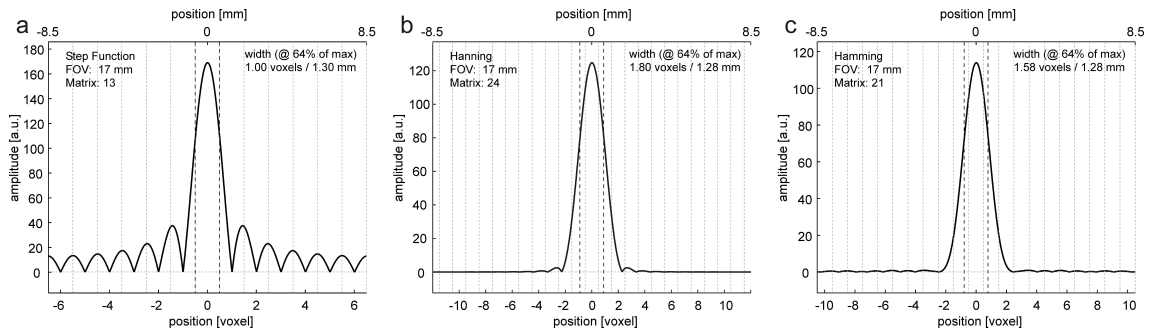


**Figure 8.3:** Adaptation of the size of the k-space sampling scheme to maintain the spatial resolution at  $\sim 1.3$  mm. Matrix sizes of 24 for the Hanning and 21 for the Hamming weighting scheme are required.

With the goal to maintain the same spatial resolution for acquisition weighted CSI, the size of the CSI matrix is to be increased to counterbalance the broadening effect of the SRF [63]. CSI matrix sizes of 24 for the Hanning and 21 for the Hamming weighting function are necessary to reduce the width of the SRF at the 64% level to 1.28 mm which is similar to the nominal resolution of 1.3 mm for the conventional  $13 \times 13$  CSI matrix (Fig. 8.3). When the sensitivity of the Hamming and the Hanning weighting are compared for equal example matrix sizes of  $13 \times 13$ ,  $21 \times 21$  or  $24 \times 24$  based on the maximum amplitude of the SRF or, equivalent, the integral of the central SRF peak with amplitudes  $>64\%$  of the maximum value, sensitivity ratios of 1.25, 1.22 and 1.21 are found. When these values are corrected for the increased number of acquisitions for the Hamming weighting, the sensitivity ratios reduce to 1.06, 1.05 and 1.02. However, the inherent sensitivity for typical CSI k-space dimensions remains higher for the Hamming scheme than for the Hanning weighting function in all cases. If differing matrix sizes of 21 for the Hamming and 24 for the Hanning weighting are used in order to achieve similar spatial resolution, the sensitivity ratio of Hamming versus Hanning is inverted to 0.91. The Hamming weighting function covers a fraction of 26% of the full acquisition space consisting of the two k-space dimensions and the number of averages along the third dimension compared to 23% for the Hanning window. For a nominal repetition number of 18, i.e. the amplitude of the k-space center, 2090 single runs of the Hamming weighted CSI sequence are necessary (see next section). Due to the increased k-space matrix size for the Hanning filter function, 18 repetitions require 2385 single runs<sup>1</sup>. If the sensitivity ratio of the Hamming versus Hanning is corrected by the ratio of the required runs similar to the comparison at equal matrix size, it becomes 1.04. Thus, the Hamming weighting function provides increased sensitivity not only for equal k-space matrix sizes, but also if the same spatial resolution is to be achieved.

Assuming that the signal and the noise amplitudes are the same for all repetitions and phase encoding steps, the SNR of the Hanning acquisition weighting has been shown to be the same as for conventional full k-space coverage [63]<sup>2</sup>. Thus, this must also be true for the Hamming filter function with an increased sensitivity compared to the Hanning acquisition scheme.

---

<sup>1</sup>The exact numbers depend on the details of the experimental realization of the filter functions and some variations are possible

<sup>2</sup>The Hanning filter function used there was not exactly the same, since it decayed to zero at the total edges of k-space. With the definition used here, zero values are achieved at the first and the last point of the k-space grid.

## 8.2 Implementation of Hamming Weighted CSI

For the experimental realization of the weighting schemes only integer repetition numbers are possible for each k-space position. The Hanning filter function decays to zero at the border of the k-space. Since these points are not measured, the sampling theorem is no longer completely fulfilled. But an up-scaling of zeros to the exact window function is not possible, therefore, a step is induced that leads to rippling in image space. The potential effects are expected to be small, however, they are negligible only if the signal amplitudes have decayed to the noise level for the outer k-space lines. The use of a Hamming sampling scheme avoids that problem, since data are acquired from all k-space lines. In addition, the results of the filter analysis correspond to the experimental realization, since the theoretically considered filter function is applied experimentally without further modifications. Here, the Hamming weighted acquisition scheme was implemented based on the above argumentation, the improved sensitivity and due to the smaller spatial contaminations from the direct vicinity of voxels, which was considered of major importance for the differentiation of neighboring brain structures.

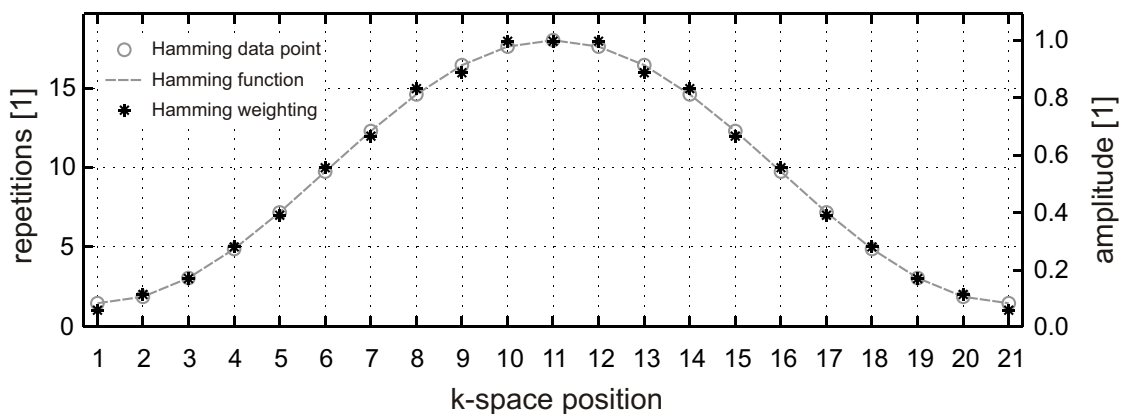


**Figure 8.4:** Section through the central k-space line of the experimental Hamming weighting scheme. A linear transformation of the Hamming filter function (gray data points, right y-coordinate) minimizes the rounding errors after discretization (black data points, left y-coordinate).

In general, arbitrary nominal average numbers, i.e. maximum amplitudes of the Hamming acquisition filter, can be used. The minimization of the deviations of the filter and the acquisition scheme, however, minimized the required post-processing correction of the discretization by up- and down-scalings of the k-space data and, therefore, the amplification of noise contributions or the waste of sensitivity. In order to minimize the related SNR loss [166] an optimized linear transformation, i.e.



a scaling and an offset, was determined to find the weighting scheme with minimal need for rounding.

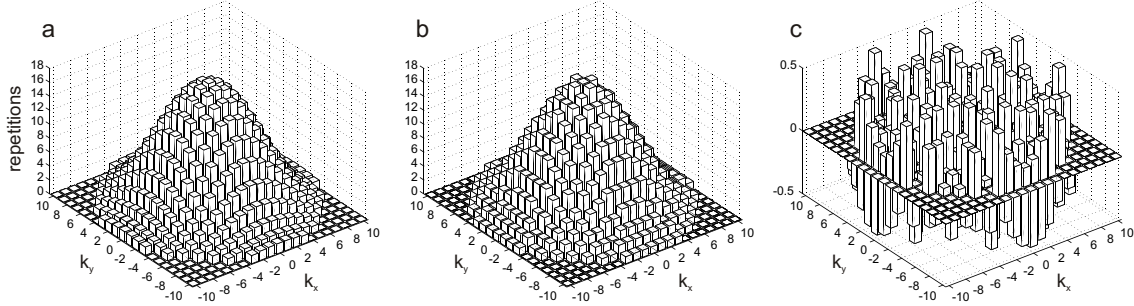


**Figure 8.5:** Optimization of the Hamming weighting scheme for experimental acquisition weighted CSI. The best linear transformation minimized rounding errors after the discretization of the filter function (a,b) and the deviations were small (c).

The radius of the Hamming filter function was chosen to exceed the actual maximum distance of the k-space positions by 5%, thereby, more than one k-space point from the outer k-space line was included. The optimized 2D filter function provided a nominal number of 18 averages and required 2090 acquisitions (Fig. 8.4/8.5). For a repetition time TR of 3 s a total acquisition time of 105 minutes was necessary for the experimental realization of the Hamming weighting scheme. Compared to conventional k-space sampling, no prolongation of the CSI experiment is required, but the SRF is considerably improved by Hamming acquisition weighting.

## 8.3 Experimental Validation

The theoretical considerations and the imaging properties of the Hamming weighted k-space acquisition scheme were experimentally validated in a water phantom. To this end, the SRF was measured for the conventional full  $13 \times 13$  k-space coverage and compared to the optimized  $21 \times 21$  Hamming weighting scheme. The water magnetization from a  $3 \times 3 \times 3 \text{ mm}^3$  voxel in the magnet's iso-center was excited with STEAM and mapped with a CSI FOV of  $60 \times 60 \times 2 \text{ mm}^3$ . The FOV dimensions far bigger than the STEAM voxel size guaranteed that the signal source could be considered point-like. The SRF of the conventional  $13 \times 13$  CSI scheme is shown in figure 8.6a and nicely matches the theoretical prediction (Fig. 8.1d). Experimentally, amplitude ratios of the side lobes were not always monotonically decaying with distance from the k-space center, however, deviations were small and the number of side lobes and their position exactly fit the theoretical expectations.

Hamming acquisition weighting completely suppressed the side lobes so that only the central peak of the SRF remained (Fig. 8.6b). The shapes of the central peaks of the SRF from conventional k-space encoding and after Hamming weighting were essentially identical with deviations e.g. of the width at 64% of the SRF maximum amplitude of less than 1%.

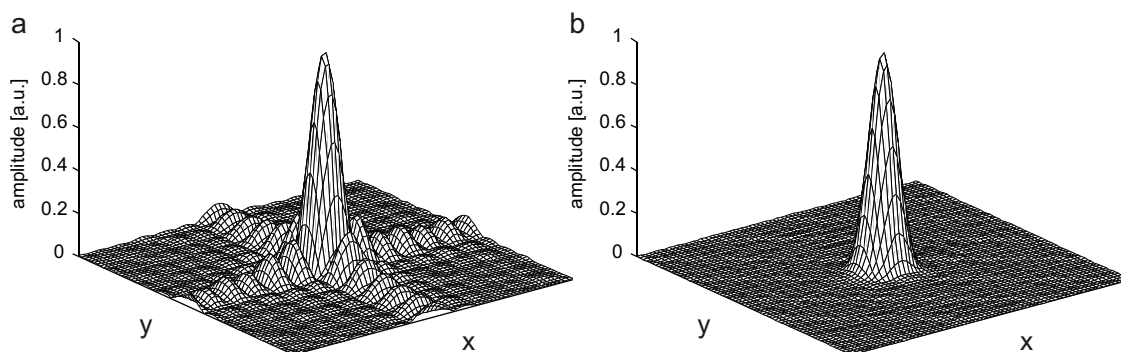


**Figure 8.6:** *Experimental validation of the improvement of the SRF. (a) The SRF for the full  $13 \times 13$  k-space coverage showed strong side bands. (b) For increased CSI matrix size of  $21 \times 21$  the central peak of the SRF after acquisition weighted Hamming filtering was essentially the same like for the conventional sampling, but the side lobes completely vanished.*

A large number of acquisitions is required for the experimental realization of acquisition weighted CSI and repetition times of the MR sequence of several seconds have to be applied based on the T1 times of the brain metabolites. Depending on the SNR to be achieved, the total experiment duration can get easily to the range of hours and the frequency drifts of the MR system of such long lasting experiments can not be neglected. The splitting of a total acquisition scheme into subunits and the interleaved application of the frequency lock algorithm can overcome the problem. Here, an alternative strategy for the removal of frequency drifts that appear during the acquisition period is possible. Since the data from the k-space center do not contain any gradient imposed phase, they can be considered single voxel MR spectroscopy signals originating from the entire CSI slice. Based on the regularly measured frequency information (Fig. 8.7), a postprocessing frequency correction by the fitted frequency development is then possible for all data.

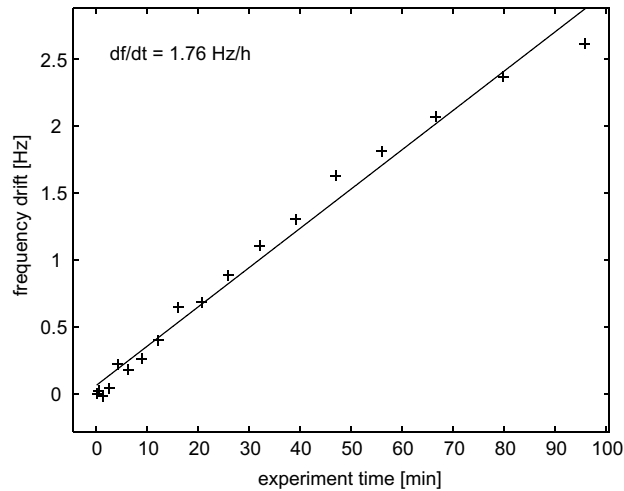


**Figure 8.7:** *If spectra from the central  $k$ -space position are selected from the full Hamming weighted acquisition scheme, tracking of the system frequency development during the acquisition period is possible. No additional experiments are required and a post-processing frequency correction can be performed. Here, the linear regression of the data points revealed a frequency drift of 1.76 Hz/h.*

## 8.4 Significance and Discussion

Acquisition weighting is a reasonable way to improve the spatial localization properties of phase encoded CSI without sensitivity loss. For CSI of brain metabolites within cortex structures this is a critical issue due to the low metabolite concentrations in brain tissue and because potential metabolite variations e.g. between brain structures or based on functional changes are expected to be small.

Hamming weighted acquisition for CSI was evaluated and compared to conventional and Hanning weighted acquisition schemes. The Hamming weighting scheme proved to be the preferable method for acquisition weighted CSI applications due to the increased sensitivity, less profound nearest neighbor contaminations and the possibility of a direct experimental realization of the theoretical filter function.

A method for Hamming acquisition weighted CSI was implemented and the improvement of the SRF was experimentally validated. Thus, Hamming acquisition weighted CSI is expected to further improve the data quality and the reliability of quantitative results from high resolution CSI of small brain structures such as the monkey visual cortex.

## Chapter 9

# MR Spectroscopy of the Primary Visual Cortex (V1)

### 9.1 In vivo MR Spectroscopy in V1

#### 9.1.1 In vivo MR Spectroscopy in Human V1

Common single voxel MR spectroscopy studies of the human visual cortex commonly use voxel volumes larger than  $10 \text{ cm}^3$  based on the limited sensitivity of MR [109–117]. The volumes include not only V1, but also white matter tissue, CSF and in some cases higher cortical areas. Furthermore, the reported results of functional MR spectroscopy studies during sensory stimulation were not always consistent. For lactate, for instance, time courses and quantitative ranges of the observed concentration changes differed considerably [109–116]. Potential explanations range from differences in experimental conditions or stimulation paradigms to varying compositions of gray matter, white matter and CSF within the MR spectroscopy volume. The later is critical because cells, synapses, astrocytes and other elements involved in the neuro-metabolic link are not uniformly distributed in the brain but the vast majority is known to be confined within the gray matter. In addition, the spatial stimulation profile, i.e. the retinotopic representation of the visual stimulus within the MR spectroscopy voxel, was poorly defined in all human studies. The functional specificity of MR spectroscopy can be improved if the spatial specificity is high enough to obtain samples exclusively confined within a special functional subunit of the brain, e.g. in the representation of a limited visual field area in V1. The required spatial selectivity, therefore, would be determined by the dimensions of the anatomical/functional brain structure to be investigated rather than by the

convenience of voxel placement. Most of the representation of the central visual field in the human brain is located inside the calcarine sulcus on the medial surface of the occipital part of the brain (Fig. 9.1a). Due to the curvature of inflated cortex and a cortical thickness in the human of 1.7–3.0 mm [167–169], minimal voxel sizes in MR spectroscopy studies were orders of magnitude bigger than what would be required by the anatomical constraints for an exclusive study of V1-regions. For the reasons briefly mentioned above no MR spectroscopy study to date was sufficiently spatially selective to provide information on the metabolism of striate cortex only.

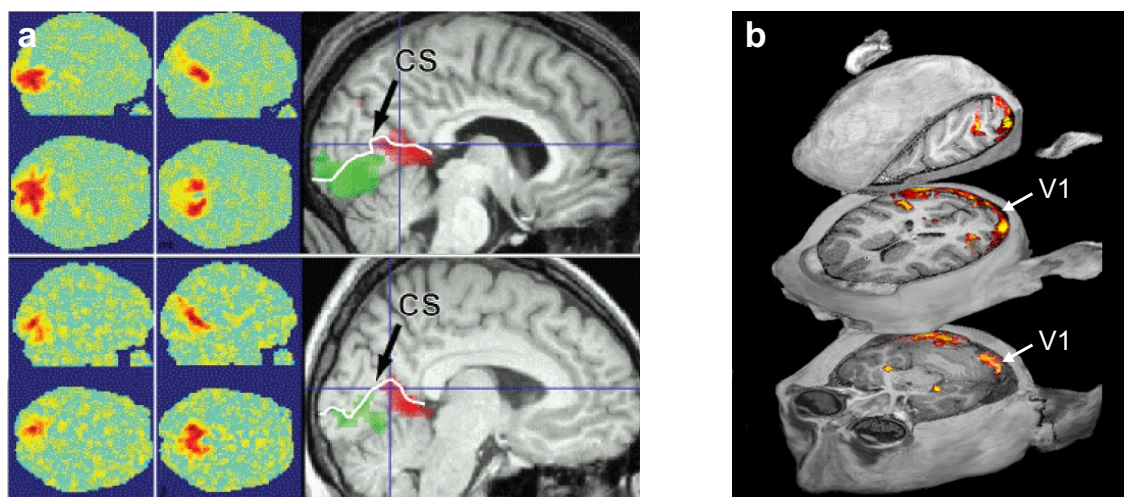


**Figure 9.1:** *V1 anatomy in human versus macaque. (a) Human V1 is located along the calcarine sulcus (CS) in the central posterior part of the brain. Functional activation along the posterior (left column, right column: green) and the anterior (center column, right column: red) central sulcus (CS) indicates the position of V1 in the human (Courtesy Dr.A.Bartels, for details see [170]). (b) V1 of the macaque is placed at the posterior surface of the brain in the direct vicinity to the skull bone (Courtesy Prof.N.K.Logothetis, for details see [171]).*

### 9.1.2 In vivo MR Spectroscopy in Monkey V1

In contrast to human neuroanatomy, the representation of the central visual field in striate cortex is located on the operculum in monkeys, namely on the posterior-lateral surface of the occipital lobe rather than within the banks of the calcarine sulcus (Fig. 9.1b). In addition, the location of the vertical meridian which commonly runs parallel to the lunate and inferioroccipital sulcus is well defined, and can be used as a landmark for the mapping of the visual field on the cortical surface. With a thickness of 1.7–2.0 mm [168] macaque V1 is only slightly thinner than

the human striate cortex. On the other hand, the monkey V1 follows the curvature of the adjacent cranial bone and is void of sulci, i.e. it is largely flat. Furthermore, the small distance to the skull surface enables the use of RF surface coils for increased sensitivity of MR investigations. In other words, the topology and position of the macaque striate cortex permits a good positioning of an MR spectroscopy voxel, albeit the volume of the latter (in the range of 30–70  $\mu\text{L}$ ) remains a challenging problem given the inherently low sensitivity of MR.

Cortex regions directly attached to the skull bone are normally avoided in human and animal MR spectroscopy experiments of the brain. Besides limited spatial selection profiles of the spectroscopy voxel and the concomitant lipid contaminations of the spectra, impaired shimming is the main problem. Strong field distortions have been reported not only from tissue and bone versus the surrounding air, but also from tissue to bone [172–174]. In contrast, in studies from inner parts of the brain the localization errors are not necessarily visible in the spectra and shimming is less problematic due to more homogeneous susceptibility conditions.

The goal here was to overcome the localization and the shimming problem in order to enable MR spectroscopy in the primary visual cortex (V1) of the macaque.

## 9.2 Shimming at the Brain Surface

### 9.2.1 Strategy for the Efficient Field Homogenization in V1

Before a strategy for the removal of the field distortions at the cortex surface could be found, typical field distributions and artifacts had to be acquired and the relevant characteristics had to be understood. To this end, magnetic field distributions from the visual cortex and particularly from MR spectroscopy voxels in V1 (see Fig. 9.2) were measured and decomposed into spherical harmonic functions. Depending on the head anatomy and rotation, and the positioning of the monkey, the second order field distortions ranged up to 75  $\text{Hz}/\text{cm}^2$  (for the Z2 shim term) in the monkey visual cortex at 7 T [175]. The third and fourth order terms were dominated by the tesseral shim terms Z3 and Z4 with values below  $\pm 20 \text{ Hz}/\text{cm}^3$  and  $\pm 10 \text{ Hz}/\text{cm}^4$  for a  $15 \times 15 \times 15 \text{ mm}^3$  cube volume, respectively. In general, the smaller the voxel examined, the less relevant were the higher order effects with respect to the frequency spread and minimal line width. For the selected small voxel size of 40  $\mu\text{L}$ , first and second order terms were considered sufficient to describe the magnetic field distribution in V1. For maximum efficiency of the mapping and decomposition of

magnetic fields in regular MR spectroscopy experiments, the FASTMAP [99] sparse sampling algorithm was used. Direct full 3D field mapping of the spectroscopy voxel, decomposition of the field distribution into spherical harmonics and subsequent adjustment of the corresponding shim currents was also possible. For a reliable field decomposition of such a small volume, however, high resolution anatomical images would have been required which was considered too time consuming for regular experiments. SNR practically limited the minimal voxel size of FASTMAP to about  $10 \times 10 \times 10 \text{ mm}^3$ ; so shimming of volumes as small as the spectroscopy voxel was not feasible. When the position of the FASTMAP voxel was adjusted to be centered in V1, the posterior parts of the projections also acquired signals, including the cranial bone, muscles and air. This led to the failure of the algorithm. A shift of the shim voxel inside the brain did not overcome this problem, because at least part of the MR spectroscopy volume remained outside the shim volume due to the curvature of the cortex. The analysis of typical field distortions in the visual cortex and in V1 enabled an alternative strategy. The behavior of the second order distortions on a larger scale was used to estimate the second terms in the vicinity of the spectroscopy volume-of-interest.

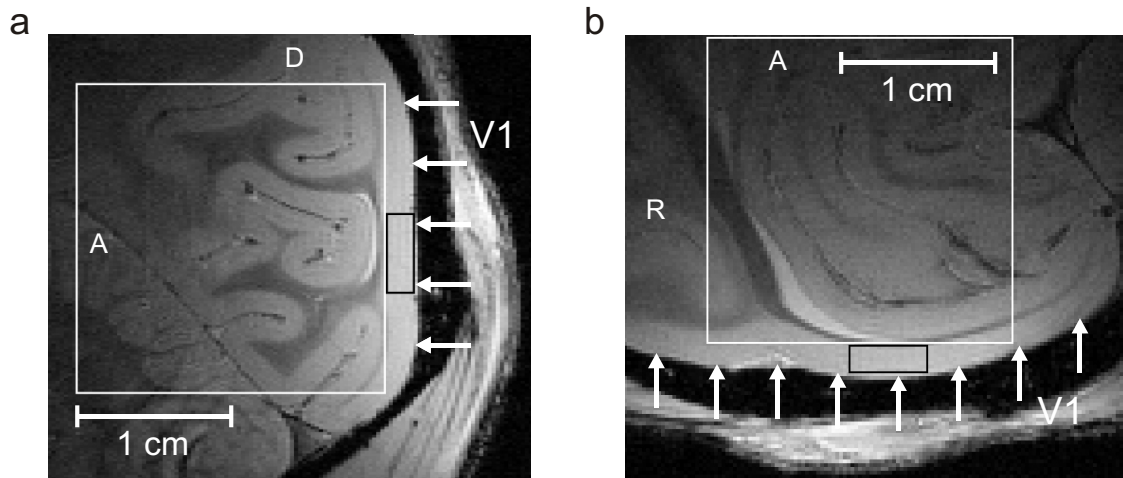


**Figure 9.2:** *FLASH* scout images from the monkey head with sagittal (a) and axial (b) slice orientation. The monkey head was rotated 45 degrees to the right to align the primary visual cortex (V1, white arrows) and the  $x$ - $z$ -plane of the laboratory coordinate system. Large scale first and second order shimming was done on a  $20 \times 20 \times 20 \text{ mm}^3$  cube voxel (white box) before a localized linear shim algorithm was applied on the  $5 \times 1.6 \times 5 \text{ mm}^3$  MR spectroscopy voxel (black box). Only areas within the voxels belong to the assigned geometries; the boxes themselves do not.

Hereby, first and second order shimming of  $10 \times 10 \times 10 \text{ mm}^3$  to  $20 \times 20 \times 20 \text{ mm}^3$  voxels from the visual cortex, i.e. the vicinity of the MR spectroscopy voxel in V1,

removed the second order terms in that VOI sufficiently (Fig. 9.2, white/black box). The detailed analysis of the frequency distribution of the MR spectroscopy voxel after large scale first and second order shimming is shown in figure 9.3 for a representative study. Linear terms remained in the voxel in V1 (Fig. 9.3a,b) and the FWHM of the fitted frequency distribution was determined to 19.4 Hz (Fig. 9.3c, N 980). The effect of further volume selective first order shimming of the voxel volume was simulated by linear detrending of the 3D field distribution. A considerable narrowing of the frequency distribution by the hypothetical removal of the linear gradients was in agreement with the observation that the remaining distortions were mainly of the first order (Fig. 9.3d,e,f, FWHM 8.0 Hz). For the actual experimental accomplishment of the localized first order shimming, the iterative algorithm from section 5.5 was used that minimized the decay of the water signal under identical experimental conditions for volume selection, timing, RF power and OVS. In practice, the theoretically predicted narrowing of the frequency distribution was not fully achieved, but the FWHM of the magnetic field distribution was improved by a factor of 2 thereby decreasing the FWHM from 19.4 Hz to 9.9 Hz (Fig. 9.3g,h,i).



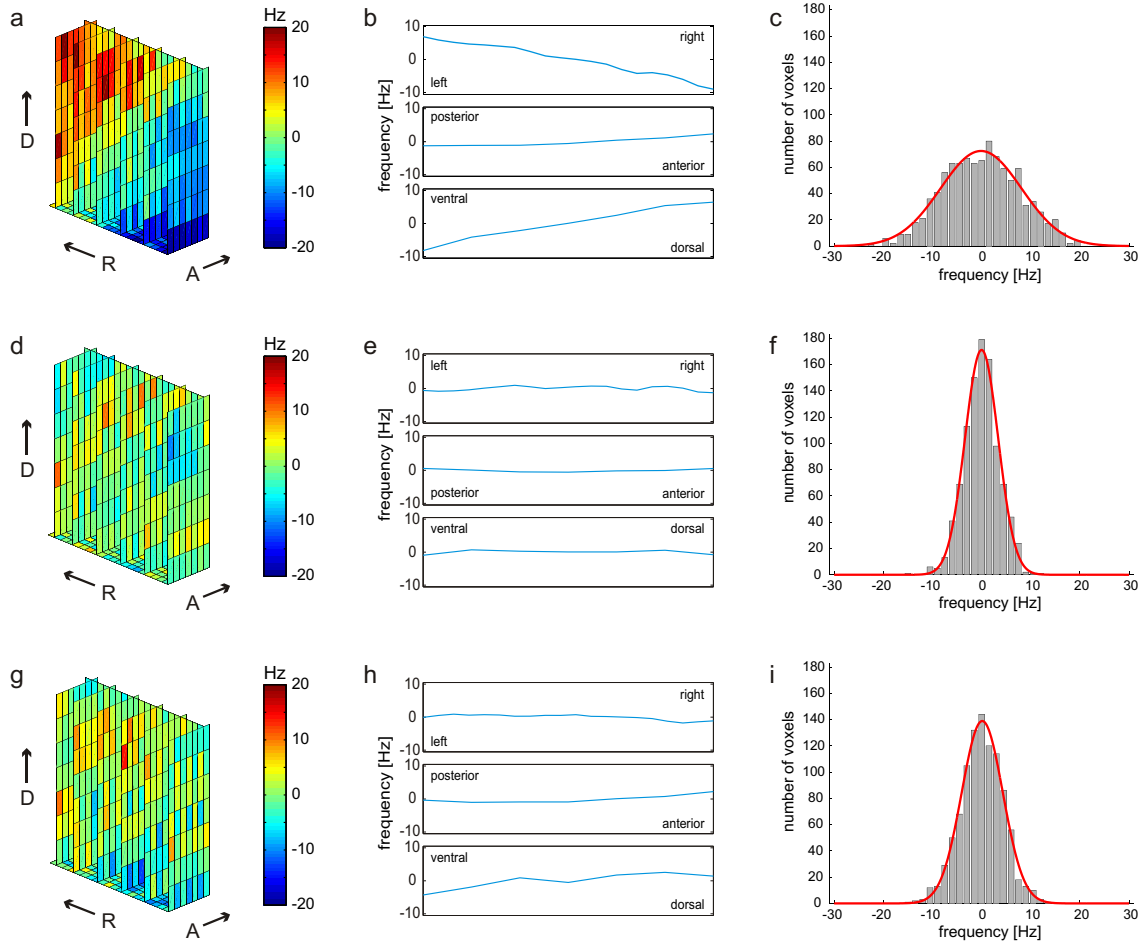


**Figure 9.3:** 3D field map analysis of a V1 voxel in the direct vicinity of the cranial bone (MR spectroscopy: FOV  $5 \times 1.6 \times 5 \text{ mm}^3$ , field mapping: FLASH, TE 10/15 ms, TR 2 s, BW 50 kHz, FOV  $64 \times 64 \times 20 \text{ mm}^3$ , matrix  $256 \times 256 \times 25$ ). After large scale first and second order shimming of a  $20 \times 20 \times 20 \text{ mm}^3$  voxel in the vicinity of the small MR spectroscopy voxel the second order field distortions were gone and mainly first order terms remained ((a) 3D field map, (b) orthogonal projections, (c) frequency histogram). A theoretical linear detrending of the frequency distribution removed the first order terms and considerably narrowed the frequency distribution (d,e,f). The experimental accomplishment of the first order shimming was achieved by iterative optimization of the FID length (g,h). The FWHM of the Gaussian fit of the 3D frequency distribution was improved by a factor of 2 ((i) FWHM 9.9 Hz, N 980) compared to the large scale shimming only ((c) FWHM 19.4 Hz), and was close to the theoretical prediction ((f) FWHM 8.0 Hz).

### 9.2.2 Field Distortions Due to the Vicinity of Blood Vessels

The pia matter and subpial space surrounding the cortical surface contain a complex system of arterial and venous blood vessels of differing orientations and diameters which range from several millimeters for the biggest arteries and veins down to a few  $\mu\text{m}$  for the smallest capillaries. Many of the small and medium size vessels are localized at the brain surface between the cranial bone and cortex in pial and subpial regions; larger vessels often follow the fundus of sulci. Blood vessels can pose two kinds of problems for localized MR spectroscopy in the cortex: partial volume effects and magnetic field distortions. If the space requirement of the vessel is achieved by cortex deformation, the vessel itself may become part of the MR spectroscopy voxel and influence quantitative results. Smaller capillaries are not critical with respect to such partial volume effects when they are found in pial regions and/or if the MR spectroscopy voxel diameter is still smaller than the cortical thickness. However, if the vessel contains venous blood, the paramagnetic property of deoxygenated hemoglobin influences not only the magnetic field inside the vessel but also its surroundings. Fig. 9.4a shows a coronal slice section through the monkey head at the surface level of the visual cortex (red dashed line in the axial view of Fig. 9.4b). Several blood vessels can be seen on the cortex surface one of which is located in the direct vicinity of an adjacent MR spectroscopy voxel (yellow box). Because arteries, brain tissue and cranial bone are diamagnetic, the field distribution neighboring a venous blood vessel becomes inhomogeneous [34–36] and an increased frequency spread was observed within the voxel in the vicinity of that vessel (Fig. 9.4c, histogram: FWHM 24.5 Hz, N 2430). The induced field distortions were complex and appeared not to be purely linear within the MR spectroscopy voxel. Localized first order shimming alone was not capable of removing them and a considerable frequency spread remained (Fig. 9.4d, histogram: FWHM 17.8).

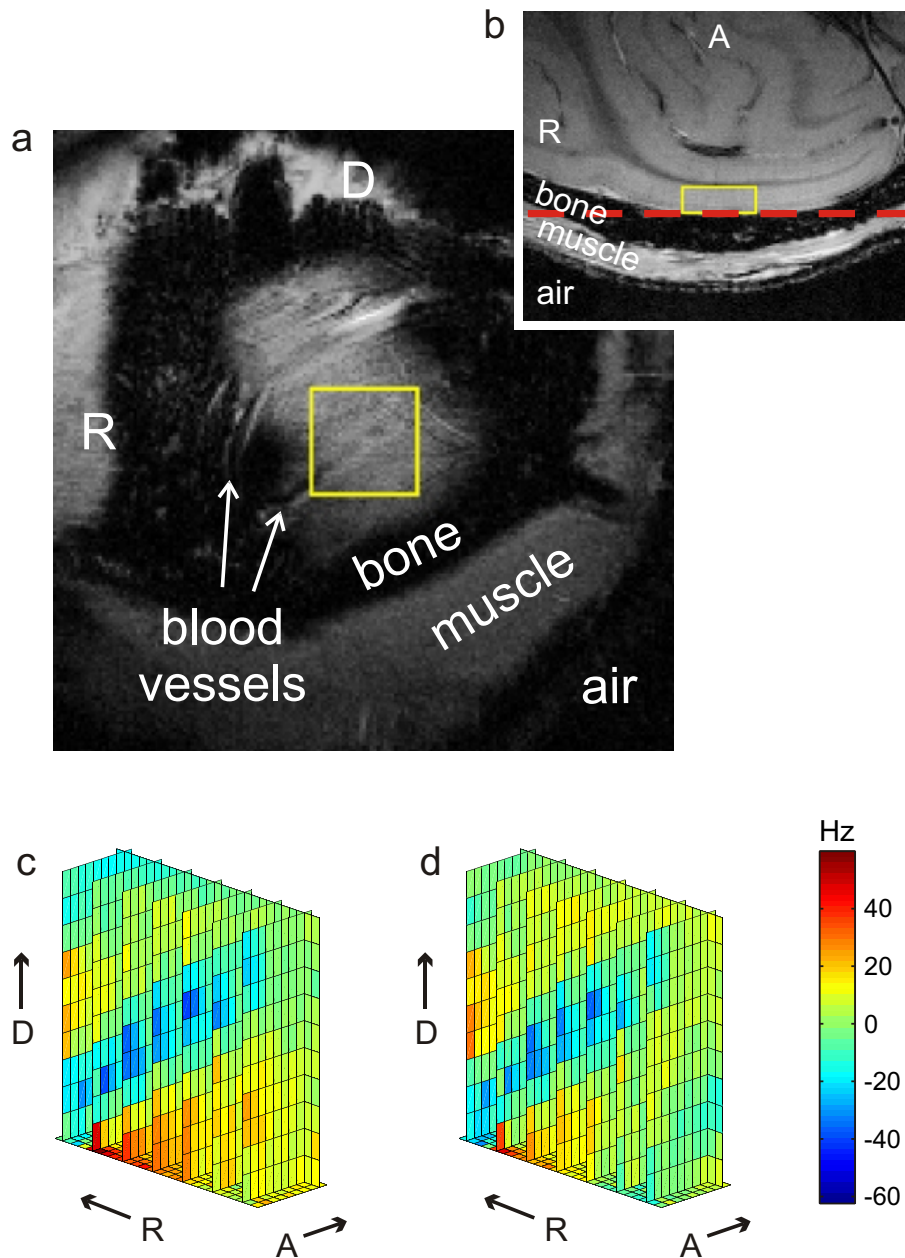


**Figure 9.4:** (a) Coronal slice section through the monkey head at the surface level of the visual cortex (red dashed line in axial view (b)). Arterial and venous blood vessels of different sizes and orientations are found between the cortex surface and the cranial bone (FLASH, coronal, FOV  $44.8 \times 44.8 \times 10.5 \text{ mm}^3$ , matrix  $256 \times 256 \times 21$ , TE 10 ms, TR 900 ms). (c) Localized field distortions are induced in the MR spectroscopy voxel in V1 (yellow box) if placed in the direct vicinity of a venous vessel (histogram FWHM 24.5 Hz, N 2430). (d) Because the distortions are not of the first order only, they cannot be fully removed by the localized linear shim algorithm (histogram FWHM 17.8 Hz).

### 9.3 Localized $^1\text{H}$ MR Spectroscopy in Macaque V1

Following the methodological improvements described above, localized  $^1\text{H}$  MR spectroscopy could be performed for the first time from macaque V1 tissue only.

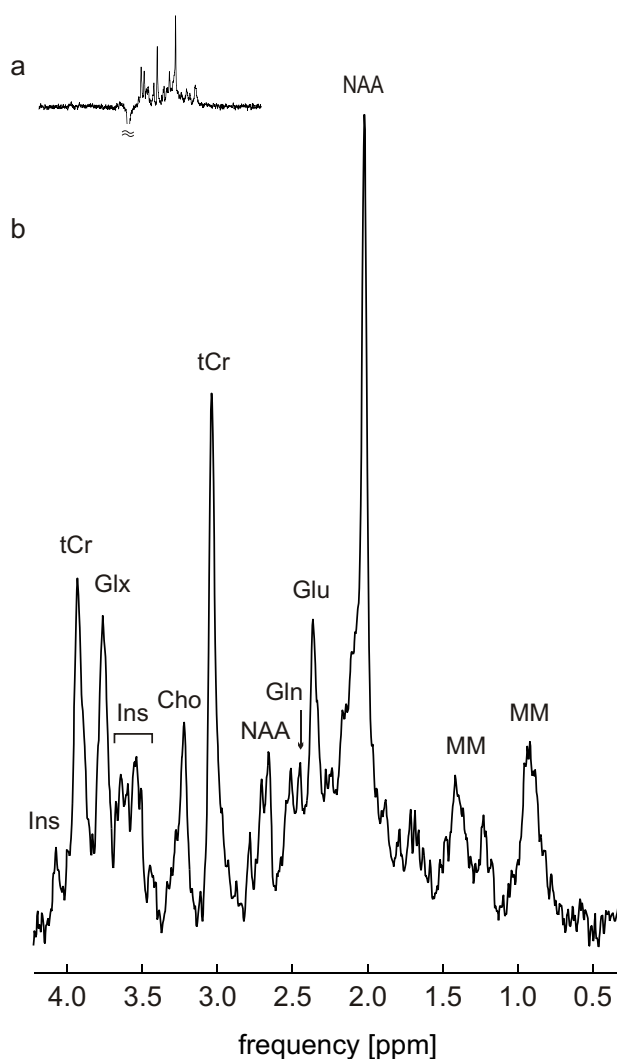


**Figure 9.5:** Localized  $^1\text{H}$  MR spectrum from pure primary visual cortex (V1) of a macaque monkey at 7 Tesla (STEAM, TE 11 ms, TM 10 ms, TR 3 s,  $5 \times 1.6 \times 5 \text{ mm}^3$ , NA 1280, LB 2 Hz). Data were eddy current corrected and zero-order phased. No baseline correction nor first order phasing was required. The SNR of 15 (LCModel 28.8), the metabolite line width of 11 Hz (FWHM, Cr + PCr at 3.03 ppm) and the overall spectral quality enabled the independent quantification of 10 metabolites at  $\text{CRLB} < 20\%$ , including GABA, Glu, Gln, Cr and PCr. The corresponding quantification is reported in table 9.1.

**Table 9.1:**  $^1\text{H}$  MR spectroscopy results from pure primary visual cortex (V1) at 7 Tesla (FOV  $5 \times 1.6 \times 5 \text{ mm}^3$ ) corresponding to figure 9.5. Spectral peak deconvolution and quantification was done with LCMoel based on the assumption of 8 mM Cr + PCr. 10 metabolites were quantified with CRLB < 20% (in parenthesis).

	Conc./mM	(CRLB)
GPC	0.6	(17)
GSH	2.1	(12)
GABA	2.6	(14)
Gln	2.9	(18)
PCr	3.9	(16)
Cr	4.1	(15)
Asp	4.7	(13)
Ins	5.3	(7)
NAA	9.4	(5)
Glu	10.5	(5)
Cr+PCr	8.0	(4)
NAA+NAAG	10.6	(3)
Glu+Gln	13.4	(5)

A selected  $^1\text{H}$  brain metabolite spectrum acquired exclusively from V1 gray matter (Fig. 9.2/black box,  $5 \times 1.6 \times 5 \text{ mm}^3$ ) is shown in figure 9.5. No first order phasing was necessary and the spectral baseline was flat in frequency regions where no metabolite or water signals were expected (Fig. 9.5a). The lack of baseline fluctuations or strong lipid and fat contamination from the neighboring cranial bone marrow proved the highly selective localization of the STEAM excitation and the additional outer volume suppression (OVS). A SNR of 15 (LCMoel: 28.8) and a spectral line width of 11 Hz for the Cr + PCr singlet at 3.03 ppm was achieved, which enabled not only the spectral separation of glutamate from glutamine, but also the deconvolution of creatine and phosphocreatine and the quantification of GABA with Cramér-Rao lower bounds < 20% (Fig. 9.5, Table 9.1).

**Table 9.2:**  $^1\text{H}$  MR spectroscopy results from pure primary visual cortex (V1) at 7 Tesla. Summary of 9 studies from different monkeys, hemispheres and head rotations. Spectral peak deconvolution and quantification was done with LCModel based on the assumption of 8 mM total creatine (Cr + PCr). Reported values are means from all studies and their standard deviations.

	Conc./mM	std.dev./mM
GPC	0.9	0.2
GABA	2.5	0.4
GSH	2.8	0.5
Gln	3.0	1.3
PCr	3.2	0.7
Asp	4.4	2.1
Cr	4.8	0.7
Ins	6.0	1.2
NAA	9.9	1.2
Glu	11.0	2.3
Cr+PCr	8.0	0.0
NAA+NAAG	10.7	1.0
Glu+Gln	14.0	3.5

A total of 9 MR spectroscopy studies was done in different monkeys, hemispheres and portions of V1. Line widths of  $(13.5 \pm 1.9)$  Hz for water and  $(13.0 \pm 1.3)$  Hz for the 3.03 ppm methylene singlet of creatine + phosphocreatine (Cr + PCr) were achieved (FWHM: mean  $\pm$  std.). The mean quantification results and the corresponding standard deviations are summarized in table 9.2 and the results were within the physiological range of gray matter values reported in the human [72, 135, 158].

## 9.4 Significance and Discussion

The first spatially localized V1-specific spectra from the primate brain were presented. A number of methodological advances was necessary to obtain the spectra-quality displayed in figure 9.5.

Firstly, imperfections of the RF pulse profile lead to signal contributions that originate from erroneous locations. For MR spectroscopy voxels inside the brain such artifacts could go unnoticed. In this study, however, the direct vicinity of the VOI to the cranial bone marrow required a high accuracy of the voxel positioning and a high quality spatial profile. Successful application of the frequency lock, and the combination of STEAM localization and OVS, proved sufficient to avoid signal contamination from the cranial bone that could lead to artificial fat signals, line broadening or baseline fluctuations. Because an ambiguous spectral baseline introduces a major uncertainty for the quantification of MR spectra, a reliable baseline definition was an important step to improve the accuracy of quantitative spectral results.

Good field homogeneity is essential for high quality spectra. A dedicated shim strategy consisting of combined large scale and localized shimming was thus developed for a fast and reliable removal of field gradients within the primary visual cortex. Field inhomogeneities within V1 voxels could be considered as first and second order in areas devoid of blood vessels. Because the second order fields are slowly varying in space, estimates of the second order terms inside the MR spectroscopy voxels in V1 were achieved by measuring the required shim fields in neighboring areas. Strong susceptibility induced field distortions were reported from other groups not only at transitions from brain tissue to air but also from brain tissue to the cranial bone [172–174]. The similar magnetic susceptibilities of tissue and bone [34–36], however, confound later observation. Based on the field distortions alone it was difficult to distinguish the effect of tissue and bone from the effect of tissue/bone and air. In addition, the geometrical conditions with respect to the scanner field play an important role. Venous blood vessels and the ear canals of the animals had considerable effects on the magnetic field distribution in the visual cortex. Strong additional variation of the magnetic field distribution at the brain surface was not observed. In fact, the proposed vicinity shimming of second order terms would not be successful if the magnetic field distribution close to the brain surface was not be smooth. Notably, all shim values determined once per session were stable over several hours and there was no need for repeating the shimming procedure or parts of it in any of the experiments.

The characteristic line of the Gennari [171] that gives a striated appearance to the primate cortex, and consists of myelinated horizontal fibers, could, in principle, have mild contamination-effects like those anticipated from partial inclusion of white matter. However, given the size of the fibres of Stellate-Cells forming the Gennari line, such a contribution is expected to be insignificant.

A period of one hour for an experiment can be considered short if long-term metabolic changes that take place during at least days or weeks are to be monitored. The observation of potential functional changes of brain metabolites as induced by sensory stimulation, however, requires a temporal resolution which is capable of accounting for appropriate physiological time scales. Using an error threshold for which metabolite quantification is considered reliable (such as a 20% CRLB limit), the achievable temporal resolution of the setup presented here cannot be assigned in general terms, but must be considered metabolite-specific.

To obtain the V1 spectra reported here, MR spectroscopy voxels as small as 40  $\mu\text{L}$  ( $5 \times 1.6 \times 5 \text{ mm}^3$ ) were used, which is roughly 2–3 orders of magnitude smaller than those commonly reported in human spectroscopy studies. The high quality of the spectra was, among other things, due to the advantages of the high field. To properly exploit the field advantages, the utilized pulse sequence was optimized with respect to the selected target region. The MR system performance was carefully monitored and evaluated in order to guarantee sufficiently high SNR for an acquisition time of 1 hour. The detailed control of the subjects positioning, as well as the maintenance of its physiology within the normal range during anesthesia was also critical for obtaining quality spectra. Pushing the lower volume limit of  $^1\text{H}$  MR spectroscopy in primates permitted the selective retrieval of neurochemical information from a particular anatomical and functional cortex structure. The  $^1\text{H}$  MR spectroscopy signal strength attained by the 7 T setup and the excellent spectral quality enabled the independent quantification of GABA, Glu, Gln, Cr and PCr in small and highly localized voxels of the macaque V1 without partial volume contamination from other anatomical or functional areas. The methodological basis was provided to address neuroscientific questions related to sensory stimulation, reorganization and plasticity in specific and well-localized anatomical or functional parts of the visual cortex.



# Chapter 10

## Summary

The goal of the thesis was to achieve maximum quality spectra from localized portions of visual cortex from the non-human primate. To this end, an appropriate setup for performing MR experiments in the anesthetized monkey was established and methods for single voxel MR spectroscopy and for conventional and acquisition weighted spectroscopic imaging were coded, implemented and optimized. The sensitivity was maximized by the strong 7 T magnetic field of the MR scanner and a combination of RF coils. The detailed characterization of the system properties and the performance by fast and easily applicable quality measures was used to optimize the setup, thereby, for instance leading to the use of an additional preamplifier in the receive chain. In addition, the measures guaranteed the functionality of the setup before and during prolonged experiments.

Different types of frequency fluctuations during *in vitro* and *in vivo* experiments were analyzed and an experimental correction algorithm was implemented to overcome the most prominent and critical long term drifts. The frequency spread due to the breathing of the anesthetized monkey was considered of minor impact on the spectral line width, however, a frequency tracking algorithm was applied during the experiment to control for exceptional strong frequency variations.

A focus of the work was the analysis and subsequent removal of magnetic field distortions that are apparent in the *in vivo* brain. To this end, magnetic fields were measured and decomposed by means of spherical harmonic functions, since the exact knowledge is the basic requirement in order to compensate for them. To meet the shim requirements in the visual cortex of the macaque, which were an order of magnitude larger than the active shim capacity of the 7 T MR system, a new combined passive and active shim approach was developed. Simple geometries of

ferromagnetic shim-elements were derived and numerically optimized to generate a complete set of modular second order spherical harmonic shim functions. The major goals of the shim design were maximization of shim field accuracy and ease of practical implementation. The theoretically optimized ferro-shim geometries were mounted on a cylindrical surface and placed inside the magnet bore, surrounding the subject's head and the RF coils. Passive shimming generated very strong shim fields and eliminated the worst of the field distortions, after which the field was further optimized by flexible and highly accurate active shimming. Here, the passive shimming procedure was first evaluated theoretically, then applied in phantom studies and subsequently validated for *in vivo*  $^1\text{H}$  MR spectroscopy in the macaque visual cortex. No artifacts due to the passive shim setup were observed and adjustments were reproducible between sessions. The modularity and the reduction to 2 pieces per shim term is an important simplification that makes the method applicable also for passive shimming within single sessions. The feasibility of very strong, flexible and high quality shimming via a combined approach of passive and active shimming is of great practical relevance for MR imaging and spectroscopy at high field strengths where shim-power is limited or where shimming of specific anatomical regions inherently requires strong shim fields.

Shimming the primary visual cortex (V1) of the macaque is particularly challenging, since it is a thin structure with a thickness of only 1.7–2.0 mm in the macaque and because it is directly attached to the cranial bone, i.e. it is a brain region prone for susceptibility induced field distortions. Typically, cortex regions in direct vicinity to the cranial bone are avoided for MR spectroscopy examinations due to these difficulties. The neuroscientific motivation of performing MR spectroscopy in V1, however, required a solution of the shimming problem. To achieve an optimal and efficient field homogenization in V1 of the macaque monkey, a serial shim strategy was developed. The second order terms were removed from a bigger voxel in the vicinity of the region-of-interest, before first order shimming was applied to the V1 MR spectroscopy voxel. With the established MR spectroscopy methods for anesthetized monkeys, and based on the methodological developments and corrections, the successful sampling from  $5 \times 1.6 \times 5 \text{ mm}^3$  (40  $\mu\text{L}$ ) volumes entirely confined within gray matter of the primary visual cortex is now possible.

The spatial resolution of  $^1\text{H}$  MR spectroscopic imaging in humans is typically in the range of centimeters. To push the spatial resolution limit in primates to a range that is capable to account for anatomical/functional dimensions, a  $^1\text{H}$  CSI method was established and optimized for the anesthetized monkey setup and the feasibility

of metabolic mapping along planar slices through the brain with a spatial resolution of 1–2 mm was demonstrated. The obtained spatial resolution permitted the segregation of gray and white matter in the visual cortex based on the concentrations of different metabolites and neurotransmitters like N-acetylaspartate, glutamate, and creatine. Concentration ratios of white matter versus gray matter tissue as well as between metabolites matched those reported in the literature from healthy human brain, demonstrating the consistency and reliability of the procedure.

Filter functions for CSI were analyzed and compared and the Hamming weighting scheme was selected based on its imaging and sensitivity characteristics. The implementation of Hamming weighted k-space sampling proved to minimize localization artifacts without loss of sensitivity. Thus, a further improvement of the attained CSI data quality and reliability of quantitative results is to be expected.

With this thesis the resolution limits for  $^1\text{H}$  MR spectroscopy and spectroscopic imaging are pushed ahead 2–3 orders of magnitude compared to previous studies in the human. The spatial specificity now reaches the level of *cortical* dimensions which is the basis for localized research e.g. on function or plasticity of the primate visual system.

# Appendix A

The chemical structures of the 20 most prominent brain metabolites are presented based on literature values [21] and reported concentrations from the healthy human or rodent brain are summarized. The relevant chemical *groups* of the biochemical *compounds* are characterized by their chemical shift  $\delta$  [ppm], the *multiplicity* (s: singlet, d: doublet, dd: doublet of doublets, t: triplet, m: multiplet) and the observed J-values [Hz]. For metabolites that consist of different moieties, the moieties are given separately as labeled in parenthesis. Reported metabolite concentrations are followed by the corresponding literature citations. Potential gray and white matter differences are not considered.

Compound	Group	$\delta$	Multipl.	J	Conc.	
Ala	$^2CH$	3.77	q	7.23	0.5–0.6	[7, 21]
	$^3CH_3$	1.47	d	-14.37		
Asp	$^2CH$	3.89	dd	3.65	0.9–2.0	[7, 21]
	$^3CH_2$	2.80	dd	9.11		
		2.65	dd	-17.43		
Cho	$N(CH_3)_3$	3.19	s	–	<0.1	[21, 44]
	$^1CH_2$	4.05	m	3.14		
	$^2CH_2$	3.50	m	0.57 - 6.98		
Cr	$N(CH_3)$	3.03	s	–	4.7–5.6	[21]
	$^2CH_2$	3.91	s	–		
	$NH$	6.65	s	–		
GABA	$^2CH_2$	3.01	m	5.37 - 7.13	0.8–1.0	[7, 21]
	$^3CH_2$	1.89	qu	6.98 - 10.58		
	$^4CH_2$	2.28	t	6.17 - 7.93		

Compound	Group	$\delta$	Multipl.	J	Conc.	
Glc ( $\alpha$ -anomer)	$^1CH$	5.22	d	3.8	1.0–2.7 [7, 21, 44]	
	$^2CH$	3.52	dd	9.6		
	$^3CH$	3.70	t	9.4		
	$^4CH$	3.40	t	9.9		
	$^5CH$	3.82	m	1.5		
	$^6CH$	3.83	dd	6.0		
	$^{6'}CH$	3.75	dd	-12.1		
	( $\beta$ -anomer)	$^1CH$	4.63	d		8.0
		$^2CH$	3.23	dd		9.1
		$^3CH$	3.47	t		9.4
		$^4CH$	3.39	t		8.9
		$^5CH$	3.45	m		1.6
		$^6CH$	3.88	dd		5.4
		$^{6'}CH$	3.71	dd		-12.3
Gln	$^2CH$	3.75	t	5.85	2.0–4.0 [7, 21, 44, 100]	
	$^3CH_2$	2.13	m	6.50		
		2.11	m	-14.50		
	$^4CH_2$	2.43	m	9.17		
		2.45	m	-15.37 - 9.21		
	$NH_2$	6.82	s	–		
	7.53	s	–			
Glu	$^2CH$	3.74	dd	7.33	8.0–12.0 [7, 21, 44, 100]	
	$^3CH_2$	2.04	m	4.65		
		2.12	m	-14.85		
	$^4CH_2$	2.34	m	8.41		
		2.35	m	-15.92 - 8.48		
Gly	$^2CH_2$	3.55	s	–	1.0 [21]	

Compound	Group	$\delta$	Multipl.	J	Conc.	
GPC (Gly)	$^1CH_2$	3.61	dd	5.77	0.15 [7]	
		3.67	dd	4.53		
	$^2CH$	3.90	m	—		
	$^3CH_2$	3.87	m	—		
		3.95	m	—		
	(Cho)	$^7CH_2$	4.31	m		3.10
						2.67
	$^8CH_2$	3.66	m	5.90		
	$N(CH_3)_3$	3.21	s	6.03		
GSH (Gly) (Cysteine)	$^{10}CH_2$	3.77	s	—	0.8–3.0 [7,21]	
		$^9NH$	7.15	t		—
	(Cysteine)	$^7CH_2$	4.56	dd		7.09
			$^{7'}CH_2$	2.93		dd
			2.97	dd		-14.06
	(Glu)	$^6NH$	8.18	d		—
			$^2CH$	3.77		t
		$^3CH_2$	2.16	m		6.36
			2.15	m		-15.48
		$^4CH_2$	2.51	m		6.7
	2.56	m	-15.92 - 7.6			
Ins	$^1CH$	3.52	dd	2.89	4.0–8.0 [7,21,100]	
	$^2CH$	4.05	t	10.00		
	$^3CH$	3.52	dd	3.01		
	$^4CH$	3.61	t	10.00		
	$^5CH$	3.27	t	9.49		
	$^6CH$	3.61	t	9.48		
Lac	$^2CH$	4.09	q	6.93	1.0–2.8 [7,44]	
	$^3CH_3$	1.31	d			

Compound	Group	$\delta$	Multipl.	J	Conc.	
NAA					6–11	[44, 72]
(Acetyl)	$^2CH_3$	2.01	s	–		
(Asp)	$^2CH$	4.38	dd	3.86		
	$^3CH_2$	2.67	dd	9.82		
		2.49	dd	-15.59		
	NH	7.82	d	6.40		
NAAG					0.5	[7]
(Acetyl)	$^2CH_3$	2.04	s	–		
(Aspartyl)	$^2CH$	4.61	dd	4.41		
	$^3CH_2$	2.72	dd	9.52		
		2.52	dd	-15.59		
(Glu)	$^2CH$	4.13	dd	–		
	$^3CH_2$	1.88	m	–		
		2.05	m	–		
	$^4CH_2$	2.19	m	–		
		2.18		–		
PCho	$^1CH_2$	4.28	m	2.23 - 7.33	0.6	[21]
	$^2CH_2$	3.64	m	2.68 - 6.30		
	N(CH <sub>3</sub> )	3.21	s	6.25		
PCr	N(CH <sub>3</sub> )	3.03	s	–	3.9–5.5	[7, 21]
	$^2CH_2$	3.93	s	–		
	NH	6.58	s	–		
	NH	7.30	s	–		
PE	$^1CH_2$	3.98	m	2.98 - 7.20	1.4–1.7	[7, 21]
	$^2CH_2$	3.22	s	0.46 - 7.29		
Scyllo	$^{1-6}CH$	3.33	s	–	0.2–0.7	[7, 21]
Tau	$^1CH_2$	3.42	t	6.40 - 6.74	1.5–6.0	[7, 21, 44]
	$^2CH_2$	3.25	t	6.46 - 6.79		

# Bibliography

- [1] Rabi I, Millman S, Kusch P, Zacharias J. The Molecular Beam Resonance Method for Measuring Nuclear Magnetic Moments. The Magnetic Moments fo  $^3\text{Li}6$ ,  $^3\text{Li}7$  and  $^9\text{F}19$ . *Phys Rev* 1939;55:526–35.
- [2] Purcell EM, Torrey HC, Pound RV. Resonance Absorption by Nuclear Magnetic Moments in a Solid. *Phys Rev* 1946;69:37–38.
- [3] Bloch F, Hansen WW, Packard M. Nuclear Induction. *Phys Rev* 1946;69:127.
- [4] Procter WG, Yu FC. The Dependence of a Nuclear Magnetic Resonance Frequency upon Chemical Compound. *Phys Rev* 1950;77:717.
- [5] Dickinson WC. Dependence of the  $^1\text{F}19$  Nuclear Resonance Position on Chemical Compound. *Phys Rev* 1950;77:736–737.
- [6] Lauterbur PC. Image Formation by Induced Local Interactions: Examples Employing Nuclear Magnetic Resonance. *Nature* 1973;242:190–191.
- [7] Pfeuffer J, Tkac I, Provencher SW, Gruetter R. Toward an in vivo neurochemical profile: quantification of 18 metabolites in short-echo-time ( $^1\text{H}$ ) NMR spectra of the rat brain. *J Magn Reson* 1999;141(1):104–20.
- [8] Tkac I, Starcuk Z, Choi IY, Gruetter R. In vivo  $^1\text{H}$  NMR spectroscopy of rat brain at 1 ms echo time. *Magn Reson Med* 1999;41(4):649–56.
- [9] Magistretti PJ, Pellerin L. Cellular mechanisms of brain energy metabolism and their relevance to functional brain imaging. *Philos Trans R Soc Lond B Biol Sci* 1999;354(1387):1155–63.
- [10] Rothman DL.  $^1\text{H}$  NMR Studies of Human Brain Metabolism and Physiology. *NMR in Physiology and Biomedicine*. San Diego: Elsevier Science and Technology Books, 1994.
- [11] Günther H. *NMR-Spektroskopie*. Stuttgart: Georg Thieme Verlag, 2nd edition, 1983.



- [12] Ernst RR, Bodenhausen G, Wokaun A. Principles of Nuclear Magnetic Resonance in One and Two Dimensions. International Series of Monographs on Chemistry 14. Oxford: Clarendon Press, 1987.
- [13] Canet D. NMR - Konzepte und Methoden. Berlin: Springer Verlag, 1991.
- [14] Slichter C. Principles of Magnetic Resonance. Berlin: Springer Verlag, 1996.
- [15] Haake EM, Brown RW, Thompson MR, Venkatesan R. Magnetic Resonance Imaging - Physical Principles and Sequence Design. New York: John Wiley and Sons, 1999.
- [16] Behar KL, Ogino T. Characterization of macromolecule resonances in the  $^1\text{H}$  NMR spectrum of rat brain. *Magn Reson Med* 1993;30(1):38–44.
- [17] Behar KL, Rothman DL, Spencer DD, Petroff OA. Analysis of macromolecule resonances in  $^1\text{H}$  NMR spectra of human brain. *Magn Reson Med* 1994;32(3):294–302.
- [18] Seeger U, Klose U, Lutz O, Grodd W. Elimination of residual lipid contamination in single volume proton MR spectra of human brain. *Magn Reson Imaging* 1999; 17(8):1219–26.
- [19] Seeger U, Klose U, Mader I, Grodd W, Nagele T. Parameterized evaluation of macromolecules and lipids in proton MR spectroscopy of brain diseases. *Magn Reson Med* 2003;49(1):19–28.
- [20] Seeger U. Kontaminationen in der volumenselektiven  $^1\text{H}$ -Kernspinresonanz-Spektroskopie mit STEAM am Beispiel des menschlichen Gehirns in vivo. Ph.D. thesis, University of Tübingen, 2004.
- [21] Govindaraju V, Young K, Maudsley AA. Proton NMR chemical shifts and coupling constants for brain metabolites. *NMR Biomed* 2000;13(3):129–53.
- [22] Sorensen OW, Eich GW, Levitt ML, Bodenhausen G, Ernst RR. Product operator formalism for the description of NMR pulse experiments. *Proc NMR Spectrosc* 1983;16:163.
- [23] Angelidis PA. Spectrum estimation and the Fourier transform in imaging and spectroscopy. *Concepts in Magnetic Resonance* 1996;8(5):339–381.
- [24] Ljunggren S. A Simple Graphical Representation of Fourier-Based Imaging Methods. *J Magn Reson* 1983;54:338–43.
- [25] Twieg DB. The k-space trajectory formulation of the NMR imaging process with applications in the analysis and synthesis of imaging methods. *Med Phys* 1985; 10:610.
- [26] Hennig J. K-space sampling strategies. *Eur Radiol* 1999;9(6):1020–31.

- [27] Vanhamme L, Sundin T, Hecke PV, Huffel SV. MR spectroscopy quantitation: a review of time-domain methods. *NMR Biomed* 2001;14(4):233–46.
- [28] Mierisova S, Ala-Korpela M. MR spectroscopy quantitation: a review of frequency domain methods. *NMR Biomed* 2001;14(4):247–59.
- [29] Stoyanova R, Brown TR. NMR spectral quantitation by principal component analysis. *NMR Biomed* 2001;14(4):271–7.
- [30] Bergmann L, Schäfer C. *Lehrbuch der Experimentalphysik, Festkörper*, volume 5. Berlin: de Gruyter Verlag, 2005.
- [31] McGinley JVM, Srivastava VC, DeMeester GD. Passive Shimming Technique for MRI Magnets, US patent 5,532,597, 1996.
- [32] Dorri B. Method for Passively Shimming a Magnet, US patent 5,677,854, 1997.
- [33] Neuberth G. Integral Passive Shim System for a Magnetic Resonance Apparatus, US patent 6,897,750 B2, 2005.
- [34] Sumanaweera TS, Glover GH, Adler JR. Method and apparatus for correcting spatial distortion in magnetic resonance images due to magnetic field inhomogeneity including inhomogeneity due to susceptibility variations, US patent 5,351,006, 1994.
- [35] Hopkins JA, Wehrli FW. Magnetic susceptibility measurement of insoluble solids by NMR: magnetic susceptibility of bone. *Magn Reson Med* 1997;37(4):494–500.
- [36] Bhagwandien R, Moerland MA, Bakker CJ, Beersma R, Lagendijk JJ. Numerical analysis of the magnetic field for arbitrary magnetic susceptibility distributions in 3D. *Magn Reson Imaging* 1994;12(1):101–7.
- [37] Li S, Dardzinski BJ, Collins CM, Yang QX, Smith MB. Three-dimensional mapping of the static magnetic field inside the human head. *Magn Reson Med* 1996;36(5):705–14.
- [38] Wilson JL, Jenkinson M, Jezzard P. Optimization of static field homogeneity in human brain using diamagnetic passive shims. *Magn Reson Med* 2002;48(5):906–14.
- [39] Jenkinson M, Wilson JL, Jezzard P. Perturbation method for magnetic field calculations of nonconductive objects. *Magn Reson Med* 2004;52(3):471–7.
- [40] Romeo F, Hoult DI. Magnet field profiling: analysis and correcting coil design. *Magn Reson Med* 1984;1(1):44–65.
- [41] Hillenbrand DF, Lo KM, Punchard WFB, Reese TG, Starewicz PM. High-Order MR Shimming: a Simulation Study of the Effectiveness of Competing Methods, Using an Established Susceptibility Model of the Human Head. *Appl Magn Reson* 2005;29:39–64.

- [42] Smythe WR. *Static and Dynamic Electricity*. New York: McGraw-Hill, 1968. Chapter 5.
- [43] Abramowitz M, Stegun I. *Handbook of Mathematical Functions*. New York: Dover Publications, 1965.
- [44] De Graaf RA. *In vivo NMR spectroscopy*. London: John Wiley and Sons, 1998.
- [45] Bottomley PA. Selective volume method for performing localized NMR spectroscopy, US patent 4,480,228, 1984.
- [46] Frahm J, Merboldt KD, Hanicke W. Localized Proton Spectroscopy Using Stimulated Echos. *J Magn Reson* 1987;72:502–508.
- [47] Hahn EL. Spin echoes. *Phys Rev* 1950;80:580–594.
- [48] Moonen CT, von Kienlin M, van Zijl PC, Cohen J, Gillen J, Daly P, Wolf G. Comparison of single-shot localization methods (STEAM and PRESS) for in vivo proton NMR spectroscopy. *NMR Biomed* 1989;2(5-6):201–8.
- [49] Ernst T, Hennig J. Coupling effects in volume selective  $^1\text{H}$  spectroscopy of major brain metabolites. *Magn Reson Med* 1991;21(1):82–96.
- [50] Zhong K, Ernst T. Localized in vivo human  $^1\text{H}$  MRS at very short echo times. *Magn Reson Med* 2004;52(4):898–901.
- [51] Brown TR, Kincaid BM, Ugurbil K. NMR chemical shift imaging in three dimensions. *Proc Natl Acad Sci U S A* 1982;79(11):3523–6.
- [52] Maudsley AA, Hilal SK, Perman WH, Simon HE. Spatially Resolved High Resolution Spectroscopy by "Four-Dimensional" NMR. *J Magn Reson* 1983;51:147–152.
- [53] Macovski A. Noise in MRI. *Magn Reson Med* 1996;36(3):494–7.
- [54] Mansfield P. Spatial mapping of the chemical shift in NMR. *Magn Reson Med* 1984; 1(3):370–86.
- [55] Macovski A. Volumetric NMR imaging with time-varying gradients. *Magn Reson Med* 1985;2(1):29–40.
- [56] Adalsteinsson E, Irarrazabal P, Spielman DM, Macovski A. Three-dimensional spectroscopic imaging with time-varying gradients. *Magn Reson Med* 1995;33(4):461–6.
- [57] Posse S, Tedeschi G, Risinger R, Ogg R, Le Bihan D. High speed  $^1\text{H}$  spectroscopic imaging in human brain by echo planar spatial-spectral encoding. *Magn Reson Med* 1995;33(1):34–40.

- [58] Adalsteinsson E, Irarrazabal P, Topp S, Meyer C, Macovski A, Spielman DM. Volumetric spectroscopic imaging with spiral-based k-space trajectories. *Magn Reson Med* 1998;39(6):889–98.
- [59] Matsui S, Sekihara K, Kohno H. High-Speed Spatially Resolved NMR Spectroscopy Using Phase-Modulated Spin-Echo Trains. Expansion of the Spectral Bandwidth by Combined Use of Delayed Spin-Echo Trains. *J Magn Reson* 1985;64:167–71.
- [60] Mareci TH, Brooker HR. High-Resolution Magnetic Resonance Spectra from a Sensitive Region Defined with Pulsed Field Gradients. *J Magn Reson* 1984;57:157–163.
- [61] Pohmann R. Methoden der orts aufgelösten NMR-Spektroskopie. Ph.D. thesis, University of Würzburg, 1999.
- [62] von Kienlin M, Pohmann R. Spatial Resolution in Spectroscopic Imaging. Spatially Resolved Magnetic Resonance. Weinheim: Wiley-VCH, 1998.
- [63] Pohmann R, von Kienlin M. Accurate phosphorus metabolite images of the human heart by 3D acquisition-weighted CSI. *Magn Reson Med* 2001;45(5):817–26.
- [64] Rayleigh L. Investigations in Optics, with Special Reference to the Spectroscope. *Philos Mag* 1879;8:261–274.
- [65] McIlwain H. Biochemistry and the Central Nervous System. Edinburgh: Churchill Livingstone, 5th edition, 1985.
- [66] Serrai H, Clayton DB, Senhadji L, Zuo C, Lenkinski RE. Localized proton spectroscopy without water suppression: removal of gradient induced frequency modulations by modulus signal selection. *J Magn Reson* 2002;154(1):53–9.
- [67] Dreher W, Leibfritz D. New method for the simultaneous detection of metabolites and water in localized in vivo <sup>1</sup>H nuclear magnetic resonance spectroscopy. *Magn Reson Med* 2005;54(1):190–5.
- [68] De Graaf RA, Sacolick LI, Rothman DL. Water and Metabolite-Modulated MR Spectroscopy and Spectroscopic Imaging. In ISMRM, annual meeting. Seattle/USA, 2006; 3063.
- [69] Haase A. Localization of unaffected spins in NMR imaging and spectroscopy (LOCUS spectroscopy). *Magn Reson Med* 1986;3(6):963–9.
- [70] Moonen CT, Van Zijl PC. Highly Effective Water Suppression for in Vivo Proton NMR Spectroscopy (DRYSTEAM). *J Magn Reson* 1990;88:28–41.
- [71] Frahm J, Bruhn H, Gyngell ML, Merboldt KD, Hanicke W, Sauter R. Localized proton NMR spectroscopy in different regions of the human brain in vivo. Relaxation

- times and concentrations of cerebral metabolites. *Magn Reson Med* 1989;11(1):47–63.
- [72] Kreis R, Ernst T, Ross BD. Absolute Quantitation of Water and Metabolites in the Human Brain. II. Metabolite Concentrations. *J Magn Reson B* 1993;102:9–19.
- [73] Deese AJ, Dratz EA, Hymel L, Fleischer S. Proton NMR T<sub>1</sub>, T<sub>2</sub>, and T<sub>1</sub> rho relaxation studies of native and reconstituted sarcoplasmic reticulum and phospholipid vesicles. *Biophys J* 1982;37(1):207–16.
- [74] Luo Y, de Graaf RA, DelaBarre L, Tannus A, Garwood M. BISTRO: an outer-volume suppression method that tolerates RF field inhomogeneity. *Magn Reson Med* 2001;45(6):1095–102.
- [75] Provencher SW. Estimation of metabolite concentrations from localized in vivo proton NMR spectra. *Magn Reson Med* 1993;30(6):672–9.
- [76] Provencher SW. Automatic quantitation of localized in vivo <sup>1</sup>H spectra with LCModel. *NMR Biomed* 2001;14(4):260–4.
- [77] Cavassila S, Deval S, Huegen C, van Ormondt D, Graveron-Demilly D. Cramer-Rao bounds: an evaluation tool for quantitation. *NMR Biomed* 2001;14(4):278–83.
- [78] Alger JR, Symko SC, Bizzi A, Posse S, DesPres DJ, Armstrong MR. Absolute quantitation of short TE brain <sup>1</sup>H-MR spectra and spectroscopic imaging data. *J Comput Assist Tomogr* 1993;17(2):191–9.
- [79] Danielsen ER, Henriksen O. Absolute quantitative proton NMR spectroscopy based on the amplitude of the local water suppression pulse. Quantification of brain water and metabolites. *NMR Biomed* 1994;7(7):311–8.
- [80] Hoult DI. "Shimming" on Spatially Localized Signals. *J Magn Reson* 1987;73:174.
- [81] Jesmanowicz A, Roopchansingh V, Cox RW, Starewicz P, PUNCHARD WFB, Hyde JS. Local Ferroschims Using Office Copier Toner. In ISMRM, annual meeting. Glasgow/Scotland, 2001; 617.
- [82] Jesmanowicz A, Hyde JS, PUNCHARD WFB, Starewicz PM. Method for Shimming a Static Magnetic Field in a Local MRI Coil, US patent 6,294,972 B1, 2001.
- [83] Wilson JL, Jezzard P. Utilization of an intra-oral diamagnetic passive shim in functional MRI of the inferior frontal cortex. *Magn Reson Med* 2003;50(5):1089–94.
- [84] Cusack R, Russell B, Cox SM, De Panfilis C, Schwarzbauer C, Ansorge R. An evaluation of the use of passive shimming to improve frontal sensitivity in fMRI. *Neuroimage* 2005;24(1):82–91.

- [85] Koch KM, Brown PM, Rothman DL, De Graaf RA. Adjustable Subject-Specific Passive Shims using Optimized Distributions of Bismuth and Zirconium. In ISMRM, annual meeting. Seattle/USA, 2006; 519.
- [86] Konzbul P, Sveda K. Shim coils for NMR and MRI solenoid magnets. *Meas Sci Technol* 1995;6:1116–1123.
- [87] Brideson MA, Forbes LK, Crozier S. Determining Complicated Winding Patterns for Shim Coils Using Stream Functions and the Target-Field Method. *Concepts in Magnetic Resonance* 2001;14:9–18.
- [88] Forbes LK, Crozier S. A novel target-field method for finite-length magnetic resonance shim coils: II. Tesseral shims. *Journal of Physics D: Applied Physics* 2002; 35(9):839–849.
- [89] Brideson MA, Forbes LK, Crozier S. Winding patterns for actively shielded shim coils with asymmetric target-fields. *Meas Sci Technol* 2003;14:484–493.
- [90] Webb P, Spielman D, Macovski A. Inhomogeneity correction for in vivo spectroscopy by high-resolution water referencing. *Magn Reson Med* 1992;23(1):1–11.
- [91] Gruetter R, Boesch C. Fast, Noniterative Shimming of Spatially Localized Signals. In Vivo Analysis of the Magnetic Field along Axes. *J Magn Reson* 1992;96:323–334.
- [92] Miyasaka N, Takahashi K, Hetherington HP. Fully automated shim mapping method for spectroscopic imaging of the mouse brain at 9.4 T. *Magn Reson Med* 2006; 55(1):198–202.
- [93] Spielman DM, Adalsteinsson E, Lim KO. Quantitative assessment of improved homogeneity using higher-order shims for spectroscopic imaging of the brain. *Magn Reson Med* 1998;40(3):376–82.
- [94] Chen Z, Li SS, Yang J, Letizia D, Shen J. Measurement and automatic correction of high-order B<sub>0</sub> inhomogeneity in the rat brain at 11.7 Tesla. *Magn Reson Imaging* 2004;22(6):835–42.
- [95] Tropp J, Derby KA, Hawrysko C, Sugiura S, Yamagata H. Automated Shimming of B<sub>0</sub> for Spectroscopic Imaging. *J Magn Reson* 1989;85:244.
- [96] Vlaardingerboek MT, Den Boer JA. *Magnetic Resonance Imaging*. Berlin: Springer Verlag, 1999.
- [97] Cusack R, Papadakis N. New robust 3-D phase unwrapping algorithms: application to magnetic field mapping and undistorting echoplanar images. *Neuroimage* 2002; 16(3 Pt 1):754–64.
- [98] Wen H, Jaffer FA. An in vivo automated shimming method taking into account shim current constraints. *Magn Reson Med* 1995;34(6):898–904.

- [99] Gruetter R. Automatic, localized in vivo adjustment of all first- and second-order shim coils. *Magn Reson Med* 1993;29(6):804–11.
- [100] Ross BD. Biochemical considerations in 1H spectroscopy. Glutamate and glutamine; myo-inositol and related metabolites. *NMR Biomed* 1991;4(2):59–63.
- [101] Ross BD, Bluml S. New aspects of brain physiology. *NMR Biomed* 1996;9(7):279–96.
- [102] Chalupa LM, Werner JS. *The Visual Neurosciences*, volume 1. Cambridge: the MIT press, 2004.
- [103] Van Essen DC. Visual areas of the mammalian cerebral cortex. *Annu Rev Neurosci* 1979;2:227–63.
- [104] Poggio GE. Central neural mechanisms in vision. In VB Mountcastle, CV Mosby, eds., *Medical Physiology*, volume 1. St. Louis: C. V. Mosby Company, 14th edition, 1980; 544–585.
- [105] Felleman DJ, Van Essen DC. Distributed hierarchical processing in the primate cerebral cortex. *Cereb Cortex* 1991;1(1):1–47.
- [106] McCormick DA, Shu Y, Hasenstaub A. Balanced recurrent excitation and inhibition in local cortical networks. In TK Hensch, M Fagiolini, eds., *Excitatory-inhibitory balance: synapses, circuits, and systems plasticity*. New York: Kluwer Academic Publishers, 1st edition, 2003; .
- [107] Douglas RJ, Koch C, Mahowald M, Martin KA, Suarez HH. Recurrent excitation in neocortical circuits. *Science* 1995;269(5226):981–5.
- [108] Haider B, Duque A, Hasenstaub AR, McCormick DA. Neocortical network activity in vivo is generated through a dynamic balance of excitation and inhibition. *J Neurosci* 2006;26(17):4535–45.
- [109] Sappey-Marinier D, Calabrese G, Fein G, Hugg JW, Biggins C, Weiner MW. Effect of photic stimulation on human visual cortex lactate and phosphates using 1H and 31P magnetic resonance spectroscopy. *J Cereb Blood Flow Metab* 1992;12(4):584–92.
- [110] Merboldt KD, Bruhn H, Hanicke W, Michaelis T, Frahm J. Decrease of glucose in the human visual cortex during photic stimulation. *Magn Reson Med* 1992;25(1):187–94.
- [111] Frahm J, Kruger G, Merboldt KD, Kleinschmidt A. Dynamic uncoupling and recoupling of perfusion and oxidative metabolism during focal brain activation in man. *Magn Reson Med* 1996;35(2):143–8.
- [112] Mangia S, Garreffa G, Bianciardi M, Giove F, Di Salle F, Maraviglia B. The aerobic brain: lactate decrease at the onset of neural activity. *Neuroscience* 2003;118(1):7–10.

- [113] Prichard J, Rothman D, Novotny E, Petroff O, Kuwabara T, Avison M, Howseman A, Hanstock C, Shulman R. Lactate rise detected by  $^1\text{H}$  NMR in human visual cortex during physiologic stimulation. *Proc Natl Acad Sci U S A* 1991;88(13):5829–31.
- [114] Chen W, Novotny EJ, Zhu XH, Rothman DL, Shulman RG. Localized  $^1\text{H}$  NMR measurement of glucose consumption in the human brain during visual stimulation. *Proc Natl Acad Sci U S A* 1993;90(21):9896–900.
- [115] Mangia S, Tkac I, Gruetter R, Van de Moortele PF, Maraviglia B, Ugurbil K. Dynamics of human brain metabolites during prolonged visual stimulation as revealed by  $^1\text{H}$ -MRS at 7 T. In ISMRM, annual meeting. Seattle/USA, 2006; 151.
- [116] Tkac I, Ugurbil K, Harel N. Functional  $^1\text{H}$  NMR spectroscopy in cat visual cortex. In ISMRM, annual meeting. Seattle/USA, 2006; 150.
- [117] Mullins PG, Rowland LM, Jung RE, Sibbitt J W L. A novel technique to study the brain's response to pain: proton magnetic resonance spectroscopy. *Neuroimage* 2005;26(2):642–6.
- [118] Xu S, Yang J, Li CQ, Zhu W, Shen J. Metabolic alterations in rat somatosensory cortex during forepaw stimulation measured by  $^1\text{H}$ -MR spectroscopy at 11.7 T. In ISMRM, annual meeting. Miami Beach/USA, 2005; 548.
- [119] Douglas RJ, Martin KA. Neuronal circuits of the neocortex. *Annu Rev Neurosci* 2004;27:419–51.
- [120] Miller BL. A review of chemical issues in  $^1\text{H}$  NMR spectroscopy: N-acetyl-L-aspartate, creatine and choline. *NMR Biomed* 1991;4(2):47–52.
- [121] Kandel ER, Schwartz JH, Jessel TM. *Principles of Neuronal Science*. New York: McGraw-Hill, 1991.
- [122] Siesjo BK. *Brain Energy Metabolism*. New York: Wiley, 1978.
- [123] Buxton RB. *Introduction to Functional Magnetic Resonance Imaging Principles and Techniques*. Cambridge: Cambridge University Press, 2002.
- [124] Rothman DL, Sibson NR, Hyder F, Shen J, Behar KL, Shulman RG. In vivo nuclear magnetic resonance spectroscopy studies of the relationship between the glutamate-glutamine neurotransmitter cycle and functional neuroenergetics. *Philos Trans R Soc Lond B Biol Sci* 1999;354(1387):1165–77.
- [125] Ames r A. CNS energy metabolism as related to function. *Brain Res Brain Res Rev* 2000;34(1-2):42–68.
- [126] Chih CP, Lipton P, Roberts J E L. Do active cerebral neurons really use lactate rather than glucose? *Trends Neurosci* 2001;24(10):573–8.



- [127] Gjedde A, Marrett S, Vafaee M. Oxidative and nonoxidative metabolism of excited neurons and astrocytes. *J Cereb Blood Flow Metab* 2002;22(1):1–14.
- [128] Rothstein JD, Martin L, Levey AI, Dykes-Hoberg M, Jin L, Wu D, Nash N, Kuncel RW. Localization of neuronal and glial glutamate transporters. *Neuron* 1994; 13(3):713–25.
- [129] Rothman DL, Hanstock CC, Petroff OA, Novotny EJ, Prichard JW, Shulman RG. Localized <sup>1</sup>H NMR spectra of glutamate in the human brain. *Magn Reson Med* 1992;25(1):94–106.
- [130] Lee HK, Yaman A, Nalcioglu O. Homonuclear J-refocused spectral editing technique for quantification of glutamine and glutamate by <sup>1</sup>H NMR spectroscopy. *Magn Reson Med* 1995;34(2):253–9.
- [131] Govindaraju V, Basus VJ, Matson GB, Maudsley AA. Measurement of chemical shifts and coupling constants for glutamate and glutamine. *Magn Reson Med* 1998; 39(6):1011–3.
- [132] Pouwels PJ, Frahm J. Regional metabolite concentrations in human brain as determined by quantitative localized proton MRS. *Magn Reson Med* 1998;39(1):53–60.
- [133] Birken DL, Oldendorf WH. N-acetyl-L-aspartic acid: a literature review of a compound prominent in <sup>1</sup>H-NMR spectroscopic studies of brain. *Neurosci Biobehav Rev* 1989;13(1):23–31.
- [134] Simmons ML, Frondoza CG, Coyle JT. Immunocytochemical localization of N-acetyl-aspartate with monoclonal antibodies. *Neuroscience* 1991;45(1):37–45.
- [135] Wang Y, Li SJ. Differentiation of metabolic concentrations between gray matter and white matter of human brain by in vivo <sup>1</sup>H magnetic resonance spectroscopy. *Magn Reson Med* 1998;39(1):28–33.
- [136] Bruhn H, Frahm J, Gyngell ML, Merboldt KD, Hanicke W, Sauter R. Cerebral metabolism in man after acute stroke: new observations using localized proton NMR spectroscopy. *Magn Reson Med* 1989;9(1):126–31.
- [137] Arnold DL, Matthews PM, Francis G, Antel J. Proton magnetic resonance spectroscopy of human brain in vivo in the evaluation of multiple sclerosis: assessment of the load of disease. *Magn Reson Med* 1990;14(1):154–9.
- [138] Brand A, Leibfritz D, Hamprecht B, Dringen R. Metabolism of Cysteine in Astroglial Cells: Synthesis of Hypotaurine and Taurine. *J Neurochem* 1998;71:827–832.
- [139] Ugurbil K, Adriany G, Andersen P, Chen W, Garwood M, Gruetter R, Henry PG, Kim SG, Lieu H, Tkac I, Vaughan T, Van De Moortele PF, Yacoub E, Zhu XH. Ultrahigh field magnetic resonance imaging and spectroscopy. *Magn Reson Imaging* 2003;21(10):1263–81.

- [140] Novotny J E J, Fulbright RK, Pearl PL, Gibson KM, Rothman DL. Magnetic resonance spectroscopy of neurotransmitters in human brain. *Ann Neurol* 2003;54 Suppl 6:S25–31.
- [141] Tkac I, Andersen P, Adriany G, Merkle H, Ugurbil K, Gruetter R. In vivo  $^1\text{H}$  NMR spectroscopy of the human brain at 7 T. *Magn Reson Med* 2001;46(3):451–6.
- [142] Gruetter R, Weisdorf SA, Rajanayagan V, Terpstra M, Merkle H, Truwit CL, Garwood M, Nyberg SL, Ugurbil K. Resolution improvements in in vivo  $^1\text{H}$  NMR spectra with increased magnetic field strength. *J Magn Reson* 1998;135(1):260–4.
- [143] Bluml S, Seymour KJ, Ross BD. Developmental changes in choline- and ethanolamine-containing compounds measured with proton-decoupled  $(^{31}\text{P})$  MRS in in vivo human brain. *Magn Reson Med* 1999;42(4):643–54.
- [144] Pfeuffer J, Tkac I, Ugurbil K, Garwood M, Gruetter R. Detection and Assignment of Phosphocreatine Signal in vivo in  $^1\text{H}$  NMR Spectra at 9.4 Tesla. In ISMRM, annual meeting. Philadelphia/USA, 1999; 1363.
- [145] Juchem C, Merkle H, Schick F, Logothetis NK, Pfeuffer J. Region and volume dependencies in spectral line width assessed by  $(^1\text{H})$  2D MR chemical shift imaging in the monkey brain at 7 T. *Magn Reson Imaging* 2004;22(10):1373–83.
- [146] Pfeuffer J, Merkle H, Beyerlein M, Steudel T, Logothetis NK. Anatomical and functional MR imaging in the macaque monkey using a vertical large-bore 7 Tesla setup. *Magn Reson Imaging* 2004;22(10):1343–59.
- [147] Logothetis NK, Guggenberger H, Peled S, Pauls J. Functional imaging of the monkey brain. *Nat Neurosci* 1999;2(6):555–62.
- [148] Sijbers J, Scheunders P, Bonnet N, Van Dyck D, Raman E. Quantification and improvement of the signal-to-noise ratio in a magnetic resonance image acquisition procedure. *Magn Reson Imaging* 1996;14(10):1157–63.
- [149] Ebel A, Maudsley AA. Detection and correction of frequency instabilities for volumetric  $^1\text{H}$  echo-planar spectroscopic imaging. *Magn Reson Med* 2005;53(2):465–9.
- [150] Kastrup A, Kruger G, Neumann-Haefelin T, Moseley ME. Assessment of cerebrovascular reactivity with functional magnetic resonance imaging: comparison of  $\text{CO}_2$  and breath holding. *Magn Reson Imaging* 2001;19(1):13–20.
- [151] Thompson RB, Allen PS. Response of metabolites with coupled spins to the STEAM sequence. *Magn Reson Med* 2001;45(6):955–65.
- [152] Ter Haar D. Theory and Applications of the Density Matrix. *Rep Prog Phys* 1961; 24:304–62.

- [153] Mulkern R, Bowers J. Density Matrix Calculations of AB Spectra from Multipulse Sequences: Quantum Mechanics Meets In Vivo Spectroscopy. *Concepts in Magnetic Resonance* 1994;6:1–23.
- [154] Muller-Bierl B, Graf H, Lauer U, Steidle G, Schick F. Numerical modeling of needle tip artifacts in MR gradient echo imaging. *Med Phys* 2004;31(3):579–87.
- [155] Muller-Bierl B, Graf H, Steidle G, Schick F. Compensation of magnetic field distortions from paramagnetic instruments by added diamagnetic material: measurements and numerical simulations. *Med Phys* 2005;32(1):76–84.
- [156] Clare S, Evans J, Jezzard P. Requirements for room temperature shimming of the human brain. *Magn Reson Med* 2005;55(1):210–214.
- [157] Pfeuffer J, Juchem C, Merkle H, Nauerth A, Logothetis NK. High-field localized (1)H NMR spectroscopy in the anesthetized and in the awake monkey. *Magn Reson Imaging* 2004;22(10):1361–72.
- [158] Michaelis T, Merboldt KD, Bruhn H, Hanicke W, Frahm J. Absolute concentrations of metabolites in the adult human brain in vivo: quantification of localized proton MR spectra. *Radiology* 1993;187(1):219–27.
- [159] Hetherington HP, Mason GF, Pan JW, Ponder SL, Vaughan JT, Twieg DB, Pohost GM. Evaluation of cerebral gray and white matter metabolite differences by spectroscopic imaging at 4.1T. *Magn Reson Med* 1994;32(5):565–71.
- [160] Tran TK, Vigneron DB, Sailasuta N, Tropp J, Le Roux P, Kurhanewicz J, Nelson S, Hurd R. Very selective suppression pulses for clinical MRSI studies of brain and prostate cancer. *Magn Reson Med* 2000;43(1):23–33.
- [161] Ebel A, Maudsley AA. Improved spectral quality for 3D MR spectroscopic imaging using a high spatial resolution acquisition strategy. *Magn Reson Imaging* 2003; 21(2):113–20.
- [162] Hetherington HP, Pan JW, Chu WJ, Mason GF, Newcomer BR. Biological and clinical MRS at ultra-high field. *NMR Biomed* 1997;10(8):360–71.
- [163] Harris FJ. On the use of windows for harmonic analysis with the discrete Fourier transform. *Proceedings of the IEEE* 1978;66(1):5183.
- [164] Mareci TH, Brooker HR. Essential considerations for spectral localization using indirect gradient encoding of spatial information. *J Magn Reson* 1991;92:229–246.
- [165] Scheenen TW, Klomp DW, Roll SA, Futterer JJ, Barentsz JO, Heerschap A. Fast acquisition-weighted three-dimensional proton MR spectroscopic imaging of the human prostate. *Magn Reson Med* 2004;52(1):80–8.

- [166] Hugg JW, Maudsley AA, Weiner MW, Matson GB. Comparison of k-space sampling schemes for multidimensional MR spectroscopic imaging. *Magn Reson Med* 1996; 36(3):469–73.
- [167] Duvernoy HM. *The Human Brain. Surface, Blood Supply, and Three-Dimensional Sectional Anatomy*. Wien: Springer Verlag, 2nd edition, 1999.
- [168] Rockel AJ, Hiorns RW, Powell TP. The basic uniformity in structure of the neocortex. *Brain* 1980;103(2):221–44.
- [169] Creutzfeld OD. *Cortex Cerebri. Leistung, strukturelle und funktionelle Organisation der Hirnrinde*. Berlin: Springer Verlag, 1983.
- [170] Frackowiak SJ, Friston KJ, Frith CD, Dolan RJ, Price CJ, Zeki S, Ashburner J, Penny W. *Human Brain Function*. San Diego: Elsevier Academic Press, 2nd edition, 2004.
- [171] Logothetis NK. The neural basis of the blood-oxygen-level-dependent functional magnetic resonance imaging signal. *Philos Trans R Soc Lond B Biol Sci* 2002; 357(1424):1003–37.
- [172] Zeng H, Constable RT. Image distortion correction in EPI: comparison of field mapping with point spread function mapping. *Magn Reson Med* 2002;48(1):137–46.
- [173] Jezzard P, Clare S. Sources of distortion in functional MRI data. *Hum Brain Mapp* 1999;8(2-3):80–5.
- [174] Windischberger C, Robinson S, Rauscher A, Barth M, Moser E. Robust field map generation using a triple-echo acquisition. *J Magn Reson Imaging* 2004;20(4):730–4.
- [175] Juchem C, Merkle H, Logothetis NK, Pfeuffer J. Localized <sup>1</sup>H spectroscopy in the primary visual cortex V1. In *ISMRM, annual meeting*. Kyoto/Japan, 2004; 2040.

# Acknowledgments

First of all, I would like to thank my supervisors Prof. Nikos K. Logothetis and Dr. Josef Pfeuffer from the Max-Planck-Institut für Biologische Kybernetik and Prof. Fritz Schick from the Eberhard-Karls-Universität Tübingen for their support throughout the whole work. Without their advice and help, the thesis would not have been possible. Prof. Logothetis who has generated an extraordinary research environment at the MPI für Biologische Kybernetik fully supported me scientifically and personally, whenever it was required. Dr. Pfeuffer introduced me to the field of MR spectroscopy and provided me a critical view on its potentials and limitations. I would like to thank Prof. Schick for officially supervising my PhD and for giving me the opportunity to join the seminars of his MR group at the university hospital Tübingen. The stimulating discussions with him and his group significantly broadened my knowledge and interests in MR and linked them to clinical problems.

I am also indebted to a series of people who collaborated with me or helped me with their thorough advices: Dr. Bernd Müller-Bierl (Eberhard-Karls-Universität Tübingen), Dr. Hellmut Merkle (National Institute of Health (NIH), Bethesda/USA), Dr. Eric Beutner (Rheinisch Westfälische Technische Hochschule (RWTH) Aachen), Dr. Anil K. Mishra (Institute for Nuclear Medicine and Allied Sciences (INMAS), Delhi/India), Dr. Mihaela Daub and Dr. Kornelius Nielsch (MPI für Mikrostrukturphysik, Halle a.d.Saale), Prof. Karl Maier (Rheinische Friedrich-Wilhelms-Universität Bonn) and last but not least my brother Dr. Sascha Juchem.

I would like to thank Michael Schmid and Han Lee for many interesting discussions, their patience in answering me the infinite number of a physicist's questions about neuroscience, and for sharing with me the same passion for *le bistro X*.

My closest friends in Tübingen Tabea Schindler, Jochen Futter and Michael Schmid I would like to thank for the time we spent together and for living with me the private as well as the professional up's and down's during the last years.

Finally, I owe the biggest thank to my beloved parents, Margit and Hans-Peter Juchem, for their infinite personal and practical support throughout the years and for being there whenever I needed them.

# Curriculum Vitae

## PERSONAL DETAILS

Name	Christoph Juchem
Date of Birth	26 June 1975
Nationality	German

## EDUCATION

2002-2006	PhD at the Max-Planck-Institute for Biological Cybernetics
2001	University of Bonn: degree in physics
1998-2001	University of Bonn
1997-1998	Universidad Autónoma de Madrid (University of Madrid/Spain)
1995-1997	University of Bonn
1994-1995	Zivildienst (community service)
1985-1994	Görres-Gymnasium (secondary school), Koblenz Abitur (school-leaving diploma)

## PRACTICAL EXPERIENCE AND INTERNSHIPS

2002-2006	supervision of internships for physics students at the University Hospital Tübingen
Aug.2000-Aug.2001	night operator at the particle accelerator of the University of Bonn (Bonner Isochron-Zyklotron)
Feb.2000-Apr.2000	internship at the University Hospital Mainz, Research Group MR-Physics
July 1998	internship at HT Plásticos (Alcalá de Henares/Spain), Dept. of Quality Control

## CONFERENCE PAPERS

Juchem C, Logothetis NK, Pfeuffer J. A Simple Approach of Combined Passive and Active Shimming for In Vivo MR Spectroscopy at High Magnetic Field. Proc. ISMRM, 1394 (2006).

Juchem C, Logothetis NK, Pfeuffer J. Localized 1H MR Spectroscopy in the Primary Visual Cortex (V1) of the Macaque Monkey. Proc. ISMRM, 152 (2006).

Juchem C, Schick F, Logothetis NK, Pfeuffer J. Region and volume dependencies in spectral linewidth assessed by 1H 2D chemical shift imaging in the monkey brain at 7T. Proc. ISMRM, 2526 (2005).

Pfeuffer J, Juchem C, Merkle H, Logothetis NK. Localized 1H MR spectroscopy in the alert monkey at 7 Tesla. Proc. ISMRM, 547 (2005).

Juchem C, Logothetis NK, Pfeuffer J. In vivo 1H MR spectroscopy at 7T in the primary visual cortex of the macaque monkey. In SfN, annual meeting 2005. Proc. SfN, 921–2 (2005).

Juchem C, Logothetis NK, Pfeuffer J. Simple approach of combined passive and active shimming for high field MR spectroscopy. Proc. ESMRMB, 225 (2005).

Juchem C, Merkle H, Logothetis NK, Pfeuffer J. In vivo CSI of glutamate in the monkey brain. In ISMRM, annual meeting. Proc. ISMRM, 32 (2004).

Juchem C, Merkle H, Logothetis NK, Pfeuffer J. Localized 1H spectroscopy in the primary visual cortex V1. Proc. ISMRM, 2040 (2004).

Juchem C, Merkle H, Logothetis NK, Pfeuffer J. In vivo spectroscopic imaging of glutamate. Proc. SfN, 154–4 (2003).

Juchem C, Merkle H, Logothetis NK, Pfeuffer J. In vivo CSI of glutamate in Macaca mulatta brain. Proc. ESMRMB, MAGMA (Supplement) 145–146 (2003).

Pfeuffer J, Juchem C, Merkle H, Logothetis NK. Proton MR Spectroscopy at 7 Tesla in the Macaque monkey. Proc. ISMRM, 1971 (2003).

Juchem C, Augath MA, Merkle H, Logothetis NK, Pfeuffer J. In vivo 1H Spectroscopy of the Caudate Nucleus in Macaca mulatta brain. Proc. ESMRMB, MAGMA 15, 377 (2002).

## PUBLICATIONS

Juchem C, Muller-Bierl B, Schick F, Logothetis NK, Pfeuffer J. Combined Passive and Active Shimming for In Vivo MR Spectroscopy at High Magnetic Fields. *J Magn Reson*, 183, 278–289(2006).

Juchem C, Logothetis NK, Pfeuffer J.  $^1\text{H}$  MR Spectroscopy of the Macaque Primary Visual Cortex at 7 Tesla: Strategies and Pitfalls of Shimming at the Brain Surface. submitted (2006).

Schmid MC, Oeltermann A, Juchem C, Smirnakis SM, Logothetis NK. Simultaneous EEG and fMRI in the macaque monkey at 4.7 T, *Magn Reson Imaging* 24(4), 335–342 (2006).

Juchem C, Logothetis NK, Pfeuffer J. High-resolution  $(^1\text{H})$  chemical shift imaging in the monkey visual cortex. *Magn Reson Med* 54(6), 1541–6 (2005).

Juchem C, Merkle H, Schick F, Logothetis NK, Pfeuffer J. Region and volume dependencies in spectral line width assessed by  $(^1\text{H})$  2D MR chemical shift imaging in the monkey brain at 7 T. *Magn Reson Imaging* 22(10), 1373–83 (2004).

Pfeuffer J, Juchem C, Merkle H, Nauerth A, Logothetis NK. High-field localized  $^1\text{H}$  NMR spectroscopy in the anaesthetized and in the awake monkey. *Magn Reson Imaging* 22(10), 1361–1372 (2004).